6-4-2012

Characterization of Martian Surfaces using Mechanical and Spectrophotometric Models

Amy Shaw
Washington University in St. Louis

WASHINGTON UNIVERSITY IN ST. LOUIS

Department of Earth and Planetary Sciences

Dissertation Examination Committee:
Raymond Arvidson, Chair
Ramanath Cowsik
Martin Israel
Bradley Jolliff
William McKinnon
Viatcheslav Solomatov

Characterization of Martian Surfaces using Mechanical and Spectrophotometric Models

by

Amy Sheriar Shaw

A dissertation presented to the
Graduate School of Arts and Sciences
of Washington University in
partial fulfillment of the
requirements for the degree
of Doctor of Philosophy

August 2012

Saint Louis, Missouri

ABSTRACT OF THE DISSERTATION

Characterization of Martian Surfaces using

Mechanical and Spectrophotometric Models

by

Amy Sheriar Shaw

Doctor of Philosophy in Earth and Planetary Sciences

Washington University in St. Louis, 2012

Professor Raymond Arvidson, Chairperson

Two recent *in situ* Mars missions, the Phoenix Mars Lander and the Mars Exploration Rover Opportunity, have explored two quite different locations on the surface of Mars. The Phoenix lander investigated the polygonal terrain and associated soil and icy soil deposits of a high northern latitude site (68.22° N, 234.25° E). The Opportunity rover, the only currently operational spacecraft on the surface of Mars, is located much closer to the equator (1.95 °S, 354.47 °E), and has been exploring the plains and sedimentary rocks in Meridiani Planum. Concurrent with *in situ* Opportunity and Phoenix observations, the Compact Reconnaissance Imaging Spectrometer for Mars (CRISM) was in orbit around Mars collecting hyperspectral data. In this dissertation, surface and orbital data are used to explore and characterize surface material properties at the Phoenix and Opportunity sites.

The Phoenix soil physical properties experiments involved the analysis of forces determined from motor currents from the Robotic Arm (RA)'s trenching activities. Using this information and images of the landing site, soil cohesion and angle of internal friction were determined. Soil dump pile slopes were used to determine the angle of internal friction of loose soil: $38^{\circ} \pm 5^{\circ}$. Additionally, an excavation model that treated walls and edges of the RA's scoop as retaining walls was used to calculate mean *in situ* soil cohesion values for several trenches in the Phoenix landing site workspace. These cohesions were found to be consistent with the stability of steep trench slopes. Cohesions varied from $0.2^{+0.4}_{-0.2}$ kPa to $1.2^{+1.8}_{-1.2}$ kPa, with the exception of a subsurface platy horizon unique to a shallow trough for which cohesion will have to be determined using other methods. Soil on a nearby polygon mound had the greatest cohesion ($1.2^{+1.8}_{-1.2}$ kPa). This high cohesion value was most likely due to the presence of adsorbed water or pore ice above the shallow icy soil surface. Further evidence for enhanced soil cohesion above the ice table includes lateral increase in excavation force, by over 30 N, as the RA approached ice. The behavior of soil near the ice table interface is of particular interest considering that many of the high-latitude and mid-latitude regions of Mars are underlain by ice.

For the region traversed by Opportunity in the vicinity of Victoria crater, normalized spectral radiances from the Compact Reconnaissance Imaging Spectrometer for Mars (CRISM) were used to retrieve surface scattering properties. Estimates agree with those retrieved in previous photometric studies which used Opportunity's Panoramic Camera (Pancam) data, and I was able to extend estimates of the Hapke single particle

scattering albedo and asymmetry parameter (from the one-term Henyey Greenstein single particle phase function) to a greater spatial and spectral range. Results are useful for determining the boundaries between surface units that otherwise look relatively uniform spectrally. This work also provides photometric functions essential for converting spectra to a single viewing geometry which will yield more accurate spectral comparisons. Results were obtained through simultaneous modeling of surface and atmospheric contributions, iterating through surface scattering parameters until a Levenberg-Marquardt least squares best fit was achieved. Retrieved single scattering albedos range from 0.42 to 0.57 (0.5663 - 2.2715 micrometers), and retrieved asymmetry parameters range from -0.27 to -0.17 (moderately backscattering). All surfaces become more backscattering with increasing wavelength. The majority of Victoria crater's ejecta apron is more backscattering than surrounding regions, indicating a change in physical properties. Images taken when the rover traversed this unit show a cover of basaltic soil with superposed millimeter-scale hematitic spherules, providing agreement with previous analyses of lab experiments showing increased backscattering with the addition of hematitic spherules. Dark wind streaks on the apron appear smooth (low backscatter) because basaltic sands have partly buried spherules, lessening millimeter-scale roughness (in agreement with previous near-surface wind streak analyses). The CRISM-derived scattering parameters also show that bedrock-dominated surfaces are less backscattering than soil-covered surfaces, largely due to lower areal abundance of spherules. The ability to analyze surface unit spherule cover is important because it relates to a wetter period during which spherules formed in Meridiani.

ACKNOWLEDGEMENTS

I thank my advisor, R. E. Arvidson, for his guidance over the past five years, and his positive influence on my research and writing style. I also thank my co-authors who have collaborated with me on the projects that contribute to this dissertation. I thank my committee members, R. Cowsik, M. H. Israel, B. Jolliff, W. B. McKinnon, and V. S. Solomatov. I also thank the mission teams that I collaborated with and that acquired the data analyzed in this dissertation, particularly the Phoenix, MER, and CRISM teams. I thank the graduate and undergraduate students, past and present, in my research group, especially: G. Coutrot, S. Cull, A. Fraeman, R. Greenberger, T. Heet, C. Kreisch, K. Lichtenberg, K. Siebach, C. Simurda, N. Stein, S. Wiseman, and L. Yang. I also thank the staff at the Remote Sensing Laboratory: L. Arvidson, K. Bennett, E. Guinness, M. Mueller, D. Scholes, S. Slavney, T. Stein, J. Wang, and F. Zhou for their general support and for sharing their software and database expertise. Special thanks to S. Murchie, F. P. Seelos, and M. J. Wolff for their collaboration and helpful insights. I also thank Paolo Bellutta for contributing the maps of ripple width, and Michael T. Mellon for providing the thermal inertia data.

Parts of this work were funded by the McDonnell Center for Space Sciences at Washington University in Saint Louis and by NASA through the MER, Phoenix, and CRISM projects.

TABLE OF CONTENTS

LIST OF FIGURES

LIST OF TABLES

Chapter 1 : Introduction

1.1 Overview

In this dissertation, the material properties of the martian surface are inferred using data from the Phoenix Mars Lander, the Opportunity Mars Exploration Rover, the Mars Reconnaissance Orbiter (MRO), the Mars Global Surveyor (MGS), and the Mars Odyssey (ODY) orbiter. Combining near-surface and orbital data allows generation of a self-consistent model of surface properties. At the Phoenix landing site, average angle of soil internal friction and soil cohesion are retrieved as a function of depth and location relative to polygonal landforms. At the Opportunity rover traverse area, combined modeling of the surface and atmosphere is applied to data from the Compact Reconnaissance Imaging Spectrometer for Mars (CRISM) aboard MRO in order to derive maps of surface single scattering albedo as well as the angular distribution of scattered light. These parameters are then compared to surface textures and materials, based on observations from Opportunity.

1.2 *In situ* Soil Properties Investigation

In Chapter 2 of this dissertation, *in situ* soil properties are presented based on analysis of Phoenix data. The Phoenix lander's high northern latitude landing site is dominated by thermal contraction polygonal landforms [*Smith et al.*, 2009]. The polygonal terrain consists of relatively loose soil of varying depth over ice-cemented soil. Phoenix measured ice table depths of ~5 cm on average, confirming pre-landing estimates (2-6 cm [*Mellon et al.*, 2008; *Arvidson et al*., 2008]). Forces derived from Phoenix Robotic Arm (RA) motor currents, along with *Balovnev*'s [1983] model of the

mechanics of soil excavation, are used to calculate mean cohesions for several trenches dug in the loose soil layer in the work area of the RA. Trench locations sample polygon sides and troughs as well as a polygon mound. Resulting Mohr-Coulomb cohesion values are consistent with and responsible for the stability of steep trench slopes. Cohesions of soils in the work area varied from $0.2^{+0.4}_{-0.2}$ kPa to $1.2^{+1.8}_{-1.2}$ kPa, with the highest soil cohesion corresponding to the center of a polygon mound. Taking into account the largest error estimate, the highest possible cohesion for the locations measured is 3 kPa. It is worth noting that there exists a subsurface platy horizon consisting of highly cohesive plates for which cohesion will have to be determined using other methods (due to low interplate cohesion affecting excavation). Cohesion over the majority of locations measured is likely due to the presence of adsorbed water and/or pore ice above the shallow icy soil surface. Enhanced cohesion near the ice table caused lateral increase in excavation force, by over 30 N, where excavations approached the ice table. Cohesion also increases with proximity to relatively pure, penetrable ice. The second Mohr-Coulomb parameter, the angle of internal friction, was estimated using soil dump site morphology; an average value of $38^{\circ} \pm 5^{\circ}$ was obtained for the RA work area. Of the previously measured *in situ* martian soils, the crusty to cloddy soil at the Viking Lander 2 site [*Moore and Jakosky*, 1989] provides the best match to the Mohr-Coulomb parameters at the Phoenix landing site. The Viking Lander 2 site is also closest and most geologically similar to the Phoenix landing site.

The analysis of the Phoenix landing site soil physical properties presented in this dissertation provides information on the fundamental mechanical properties of the soil,

including depth profiles and the relation of these properties to the presence of icy soil. The results presented here will need to be taken into account in any model of Phoenix soil, and will provide constraints for laboratory experiments on analog soils.

The determination and interpretation of the Phoenix soil properties presented in this dissertation have been published in the *Journal of Geophysical Research* [*Shaw et al.,* 2009]. I led the analyses, with contributions from my coauthors. We were all heavily involved in mission operations, and my coauthors were also involved in mission preparation. They provided data, including force values, and significant data processing as well as invaluable information on modes and procedures of instrument operation and how these affected the data. Many useful discussions with coauthors contributed to the final manuscript.

1.3 Self-Consistent Model for Surface Texture from Rover-based and Orbital Data

In Chapters 3 and 4 of this dissertation, a self-consistent model of the materials within the section of the Opportunity rover's traverse region around Victoria crater, based on a combination of orbital and near-surface results, is presented. Scattering properties of the surface are retrieved using a simplified version of *Hapke*'s [1993] model in order to map single scattering albedo and the angular asymmetry of scattered light (which is strongly affected by surface roughness). There is a positive correlation between single scattering albedo and apparent surface roughness for variations in the spectral domain (i.e. variations in scattering properties from one wavelength to another). There is a negative correlation between single scattering albedo and apparent surface roughness for

variations in the spatial domain (i.e. variations in scattering properties from one region to another); this finding is in agreement with the independently obtained near-surface results of *Johnson et al*. [2006]. This latter correlation appears to be a mixing line between bedrock-rich region and soil-rich region end-members.

Previous workers [*Shepard and Helfenstein*, 2007] infer that roughness affecting photometric results is in the size range of millimeters down to the particle size. They hypothesize that this scale represents the smallest size scale for which shadows are not strongly affected by multiple scattering. From combining orbital and near-surface results, it is apparent that roughness at the scale of ~3-5 millimeters (i.e. roughness due to hematitic spherules along Opportunity's traverse) has a significant effect on how the surface in Opportunity's traverse region scatters light, and that the relative roughness at this size scale can be determined from orbit. It is interesting to note that the presence of large ripples does not have a strong correlation with observed backscatter.

The work conducted for this dissertation shows that the entire study area (centered on Victoria crater) is backscattering at all wavelengths studied, with backscatter increasing with wavelength. Regions of Victoria's ejecta apron that are not associated with wind streaks are consistently more backscattering than the surrounding terrain due to the presence of larger hematite-rich spherules. Wind streaks are less backscattering than the rest of the ejecta apron due to aeolian deposits partly burying spherules (i.e. smoothing out millimeter-scale roughness). These results, as well as single-scattering albedo spectra and asymmetry parameter (asymmetry of angular scatter) spectra are in agreement with those from near-surface work [*Geissler et al*., 2008; *Johnson et al*., 2006]

for wavelengths (0.432-1.009 μm) for which there exist near-surface results. The interpretation that backscatter seen from orbit is heavily affected by spherules is also in agreement with lab experiments [*Johnson et al*., 2007].

The analysis of surface properties at the Opportunity traverse region presented in this dissertation has identified a main factor, hematitic spherules, that is contributing to the photometric signal in the area around Victoria crater. This yields information about the current surface and how it affects observations made from orbit and from near-surface instrumentation.

I conducted the determination and interpretation of surface properties at the Opportunity traverse area presented in this dissertation with the guidance of my faculty advisor, Raymond Arvidson, and this work is currently in preparation for publication in the *Journal of Geophysical Research*.

References

Arvidson, R. E., D. Adams, G. Bonfiglio, P. Christensen, S. Cull, M. Golombek, J. Guinn, E. Guinness, T. Heet, R. Kirk, A. Knudson, M. Malin, A. McEwen, A. Mushkin, T. Parker, F. Seelos IV, K. Seelos, P. Smith, D. Spencer, T. Stein, L. Tamppari, (2008), Mars Exploration Program 2007 Phoenix landing site selection and characteristics, *J. Geophys. Res*., *113*, E00A03.

Arvidson, R. E., J. F. Bell III, P. Bellutta, N. A. Cabrol, J. G. Catalano, J. Cohen, L. S. Crumpler, D. J. Des Marais, T. A. Estlin, W. H. Farrand, R. Gellert, J. A. Grant, R. N. Greenberger, E. A. Guinness, K. E. Herkenhoff, J. A. Herman, K. D. Iagnemma, J. R. Johnson, G. Klingelhofer, R. Li, K. A. Lichtenberg, S. A. Maxwell, D. W. Ming, R. V. Morris, M. S. Rice, S. W. Ruff, A. Shaw, K. L. Siebach, P. A. de Souza, A. W. Stroupe, S. W. Squyres, R. J. Sullivan, K. P. Talley, J. A. Townsend, A. Wang, J. R. Wright, A. S. Yen (2010), Spirit Mars Rover Mission: Overview and selected results from the northern Home Plate Winter Haven to the side of Scamander crater, *J. Geophys. Res*., *115*, E00F03.

Balovnev, V. I. (1983), *New methods for calculating resistance to cutting of soil*, Amerind Publishing (Translation), P. Datta translator and Rosvuzizdat, New Delhi, Available from National Technical Information Service, Springfield, VA 22161.

Geissler, P. E., J. R. Johnson, R. Sullivan, K. Herkenhoff, D. Mittlefehldt, R. Fergason, D. Ming, R. Morris, S. Squyres, L. Soderblom, M. Golombek (2008), First in situ

investigation of a dark wind streak on Mars, *J. Geophys. Res.*, *113*, E12S31, doi:10.1029/2008JE003102.

Hapke, B. (1993), *Theory of Reflectance and Emittance Spectroscopy*, Cambridge Univ. Press, New York.

Shepard, M. and P. Helfenstein (2007), A test of the Hapke Photometric model, *J. Geophys. Res.*, *112*, E03001.

Johnson, J. R., W. M. Grundy, M. T. Lemmon, J. F. Bell III, M. J. Johnson, R. Deen, R. E. Arvidson, W. H. Farrand, E. Guinness, A. G. Hayes, K. E. Herkenhoff, F. Seelos IV, J. Soderblom, S. Squyres (2006), Spectrophotometric properties of materials observed by Pancam on the Mars Exploration Rovers: 2. Opportunity, *J. Geophys. Res.*, *111*, E12S16.

Johnson, J. R. et al. (2007) Spectrogoniometric measurements and models of Mars analog soils. *LPS XXXVIII*, Abstract #1288.

Mellon, M. T., W. V. Boynton, W. C. Feldman, R. E. Arvidson, T. N. Titus, J. L. Bandfield, N. E. Putzig, H. G. Sizemore (2008), A prelanding assessment of the ice table depth and ground ice characteristics in Martian permafrost at the Phoenix landing site, *J. Geophys. Res.*,*113*, E00A25, doi:10.1029/2007JE003067.

Moore, H. J., and B. M. Jakosky (1989), Viking Landing Sites, Remote-Sensing Observations, and Physical Properties of Martian Surface Materials, *Icarus, 81*, 164-184.

Murchie, S., R. Arvidson, P. Bedini, K. Beisser, J.-P. Bibring, J. Bishop, J. Boldt, P. Cavender, T. Choo, R. T. Clancy, E. H. Darlington, D. Des Marais, R. Espiritu, D.

Fort, R. Green, E. Guinness, J. Hayes, C. Hash, K. Heffernan, J. Hemmler, G. Heyler, D. Humm, J. Hutcheson, N. Izenberg, R. Lee, J. Lees, D. Lohr, E. Malaret, T. Martin, J. A. McGovern, P. McGuire, R. Morris, J. Mustard, S. Pelkey, E. Rhodes, M. Robinson, T. Roush, E. Schaefer, G. Seagrave, F. Seelos, P. Silverglate, S. Slavney, M. Smith, W.-J. Shyong, K. Strohbehn, H. Taylor, P. Thompson, B. Tossman, M. Wirzburger, M. Woff (2007), Compact Reconnaissance Imaging Spectrometer for Mars (CRISM) on Mars Reconnaissance Orbiter (MRO), *J. Geophys. Res*., *112*, E05S03.

Shaw, A., R. E. Arvidson, R. Bonitz, J. Carsten, H. Uwe Keller, M. T. Lemmon, M. T. Mellon, M. Robinson, and A. Trebi-Ollennu (2009), Phoenix Soil Physical Properties Investigation, *J. Geophys. Res., 114*, E00E05, doi:10.1029/2009JE003455.

Smith, P. H., L. Tamppari, R. E. Arvidson, D. Bass, D. Blaney, W. Boynton, A. Carswell, D. Catling, B. C. Clark, T. Duck, E. DeJong, D. Fisher, W. Goetz, P. Gunnlaugsson, M. Hecht, V. Hipkin, J, Hoffman, S. F**.** Hviid, H. U**.** Keller, S. Kounaves, C. Lange, M. Lemmon, M. B**.** Madsen, W. Markiewicz, J. Marshall, C. McKay, M. Mellon, D. Ming, R. V. Morris, W. T. Pike, N. Renno, U. Staufer, C. Stoker, P. Taylor, J. Whiteway, A. Zent (2009), H2O at the Phoenix Landing Site, *Science*, *325*, 58, doi: 10.1126/science.1172339.

Chapter 2 : Phoenix Soil Physical Properties Investigation

Journal of Geophysical Research, 114, E00E05, doi:10.1029/2009JE003455

2.1 Introduction

The Phoenix Lander investigated the polygonal terrain and associated soil and icy soil deposits of a high northern latitude site on Mars. The soil physical properties component involved the analysis of force data determined from motor currents from the Robotic Arm (RA)'s trenching activity. Using this information and images of the landing site, soil cohesion and angle of internal friction were determined. Dump pile slopes were used to determine the angle of internal friction of the soil: 38°±5°. Additionally, an excavation model that treated walls and edges of the scoop as retaining walls was used to calculate mean soil cohesions for several trenches in the Phoenix landing site workspace. These cohesions were found to be consistent with the stability of steep trench slopes. Cohesions varied from $0.2^{+0.4}_{-0.2}$ kPa to $1.2^{+1.8}_{-1.2}$ kPa, with the exception of a subsurface platy horizon unique to a shallow trough for which cohesion will have to be determined using other methods. Soil on polygon mounds had the greatest cohesion ($1.2^{+1.8}_{-1.2}$ kPa). This was most likely due to the presence of adsorbed water or pore ice above the shallow icy soil surface. Further evidence for enhanced cohesion above the ice table includes lateral increase in excavation force, by over 30 N, as the RA approached ice.

The Phoenix Mars Lander (Scout Mission) landed at 68.22° N, 234.25° E (Areocentric) on May 25th 2008 and operated until Nov. 2nd, 2008 [*Smith et al.*, 2008]. Phoenix was equipped with a 2.4 m Robotic Arm (RA) that was designed to excavate down to a buried ice table and to acquire and deliver samples of martian soil to deck-mounted instruments [*Arvidson et al.*, 2009]. There are three main types of materials at the site: 1) soil, 2) relatively pure ice, and 3) icy soil. For the first type of material, the term "soil" is used to describe unconsolidated surface material that has undergone various soil formation processes, such as cryoturbation (this practice follows nomenclature developed by *Moore et al.* [1987]). During the mission, most of the excavation was conducted in this type of material. See Figure 2.1 for a workspace digital elevation map which includes the trenches and dump piles resulting from RA activity. *Bonitz et al.* [2008] gives a review of the RA design and operation. In our paper we use RA trajectory information, retrieval of forces from RA excavations, and images from spacecraft cameras to investigate the physical properties of the soil at the Phoenix landing site.

First, background is provided for the landing site, the data sets used, and RA operations. Then we discuss the determination of the first of two Mohr-Coulomb parameters, the angle of internal friction and how it relates to trench slopes. We next review the method of determining the second Mohr-Coulomb parameter: cohesion. This is followed by a description of an example excavation from a laboratory test in a known material, for which the method of *Balovnev* [1983] yields a reasonable cohesion. We then analyze forces associated with RA excavations in the polygonal landforms at the Phoenix site and retrieve values for soil cohesion. Slope stability calculations are used to

demonstrate that retrieved cohesions and angles of internal friction are consistent with trench wall slopes and the absence of wall failures. We then end with a discussion of platy soil that forms a morphologically unique texture relative to the other soil exposures at the landing site.

2.2 Background

The Phoenix lander operated from approximately L_s 77° to 151°. It is the northernmost landed Mars mission to date. The northern plains landing site was chosen because of the prediction of buried water ice based on hydrogen detected in neutron data from the Gamma Ray Spectrometer (GRS) Suite on the Mars Odyssey spacecraft [*Boynton et al.*, 2002] and based on thermal inertia data [*Mellon et al.*, 2008]. Ice table depth (~5 cm) observations measured during the Phoenix mission are consistent with current diffusive equilibrium with atmospheric water vapor [*Sizemore et al.*, 2010; *Mellon et al*., 2008]. Orbital observations also indicate the presence of adsorbed water on surface soil grains [*Poulet et al.*, 2009].

Thermal cracking of the buried icy soil is thought to have led to the formation of meter-scale polygonal trough networks in the overlying soil [*Mellon et al.*, 2009], whose properties are examined in this paper. Throughout this paper, the term "icy soil" is used to indicate the impenetrable (for the scoop blade) ice-cemented soil located underneath a cover of penetrable soil (although, as addressed later, there may be limited pore ice or adsorbed water in this layer as well). Figure 2.2 shows the RA workspace with approximate polygon outlines drawn in. The RA had access to a shallow polygon trough,

a deep trough, the sides of two polygons, and one polygon center, as delineated in *Arvidson et al.* [2009]. Arrows in Figure 2.2 indicate where, in relation to these features, ice or icy soil was uncovered.

The parent material of the soil was ejecta from Heimdal crater (which is ~11.5 km in diameter and located ~20 km to the east of the landing site) mixed in with aeolian material [*Heet et al.*, 2009]. The site is in a valley underlain by the Scandia region unit (see *Tanaka et al.* [2008] for possible formation mechanisms), near the northern boundary of the Alba Patera unit [*Heet et al.*, 2009]. Of the sites visited by landed missions, the Viking Lander 2 site (at ~48° N latitude) is most geologically similar to the Phoenix site, as it is also in the northern lowlands, has a polygonal network, is quite flat [*Mutch et al.*, 1977], and is presumed to have underlying ice. Compared to the other landing sites, the Phoenix site has the lowest rock abundances and least evidence of aeolian processes.

Wet chemistry and Thermal and Evolved Gas Analyzer (TEGA) results indicate the Phoenix soil includes carbonate and perchlorate salts and is somewhat alkaline in pH [*Smith et al.*, 2009; *Boynton et al.*, 2009; *Hecht et al.*, 2009; *Kounaves et al.*, 2010]. The soil exhibits the particle size distribution of loamy sand (Thomas Pike, personal communication). Particle size distribution can affect apparent cohesion, but the effect is minimal compared to that of inter-particle cohesion (loamy sands do not have high apparent cohesion because there is a minimal clay-size fraction). Tests where soil clods that were sprinkled onto instrument covers broke apart on contact show that the soil is

weakly cohesive, and so there must be an additional contributing factor to cohesion beyond that from particle size [*Arvidson et al.*, 2009].

In this paper, we give numerical estimates of the cohesion and angle of internal friction of the soil. Thus it is useful to look at the magnitude of these parameters at other locations on Mars. The Viking landers encountered soil that was classified into three types: drift, blocky, and crusty to cloddy [*Moore and Jakosky*, 1989]. Values for cohesion and angle of internal friction for these soil types as well as soils encountered by the Pathfinder and MER rovers are given in Table 2.1. Phoenix soils appear similar to crusty to cloddy soils from the Viking Lander 2 site, as explained in detail in *Arvidson et al.* [2009].

2.3 Primary Data Sets

There are two primary data sets on which much of the analysis in this paper is based: 1) images of the trenches by cameras onboard the Phoenix spacecraft [*Lemmon et al.*, 2008; *Keller et al.*, 2008] and 2) data acquired by the RA while trenching. The RA is a four-degree-of-freedom arm. The degrees of freedom correspond to the four joints, two of which are located in the shoulder and provide motion in azimuth and elevation, and the other two provide motion in elevation for the elbow and wrist. Only the three joints providing motion in elevation were in operation during excavation. Excavation was conducted in a backhoe-style, scooping material towards the lander and lifting it up to be transported to the appropriate dump location. Data from the RA include force values experienced by the RA, time at which those forces were experienced, Cartesian position

values for where the RA was located at any point in time, and scoop blade angle values. See Figure 2.3 for an image of the scoop. Coordinates are in Payload Frame [*Zamani et al.*, 2008] and refer to the position of the scoop tip. The Payload Frame has its origin at the RA shoulder (which is at deck level), the x-axis points north, the y-axis points east, and the z-axis points downward (the lander touched down with an orientation such that the side with the RA faced north; this kept icy soil in shadows once exposed). Scoop position was computed based on reported joint angles and the lengths of segments of the arm. The force data were calculated from motor currents, which were measured frequently throughout arm operation. Motor currents were converted to torques via a relation determined by testing and curve-fitting. The torque values were then converted to force values via the manipulator Jacobian (the manipulator Jacobian is a matrix obtained by taking the Jacobian of the forward kinematic equations. See *Spong and Vidyasagar* [1989] for information on derivation and use). A temperature correction was also applied using a relation based on testing and curve-fitting. Resulting force values were broken up into components, of which radial force (Fr) and vertical force (Fz) are used in this paper. Radial force is the lateral force in the direction of excavation. Many of the force values given in this paper are resultant forces ($F = \mathrm{sqrt}(Fr^2 + Fz^2)$) in the plane that contains the vertical vector as well as the vector pointing in the direction of excavation (Figure 2.4). Usable force values are sparser than the trajectory values.

The data are affected by two sources of oscillation that are systematic effects independent of any soil property. Oscillations in the trajectory data were caused by the algorithm used to determine the intermediate trajectory points in between commanded

trajectory points. Oscillations can also appear in the force data; these were caused by the accommodation algorithm. Accommodation occurred when the RA experienced a high level of force; it retreated backward from the ground until the force returned to a value that was considered safe for operation. This accommodation sometimes caused RA trajectory to follow the topography of the interface between the soil and the underlying icy soil instead of following commanded trajectory.

When the RA was in contact with the soil, positions returned in the data were less exact than for moves in free air. When the arm was loaded against the surface, it flexed, resulting in errors in the calculated position. In extreme cases, the error was 2-4 cm at the end of the 2.4 m-long arm. Relative positioning was generally more accurate than absolute positioning, and positions were repeatable to within 2 mm.

Each time a trenching operation was scheduled during the mission, the following parameters were commanded: starting position, trench depth, trench length, trench width, and trench slope, as well as several other parameters. In this paper, each traverse across the bottom of a trench is called a pass. Each trenching command generally resulted in a number of passes (anywhere from one to greater than thirty passes depending on trenching objectives), and each pass attempted to proceed deeper than the previous pass until the commanded depth was achieved. The depth interval between passes was commanded to be different for different trenches. This was done because the trenches are of various lengths and the intent was to ensure that the scoop did not fill before it reached the end of the trench. Depth intervals between passes ranged from about a third of a centimeter (as was the case for Snow White Trench – most features at the landing site

were named after fairy-tale characters) up to one centimeter (DodoGoldilocks Trench). In this paper, each section of a trench that is one scoop width across is called a swath. Many trenches were excavated using multiple trenching commands, and each of these commands often resulted in the creation of multiple swaths (to accomplish this, the RA scoop would generally pass over one swath, then over the next, and then alternate between the two until the trench was complete). This allowed better viewing of a greater expanse of the trench floor.

Another important item to note is that, in general, the angle at which the scoop blade was inclined with respect to the horizontal varied as the RA scoop traveled across the bottom of the trench. For example, sol 76 trenching in Stone Soup had a minimum angle of 116.3°, a maximum of 162.7°, and a mean of 146.1°. Figure 2.5 illustrates the range of blade angle values. Although the scoop blade angle varied along each pass (becoming shallower as the pass progressed), in general it did not change from pass to pass.

2.4 Dump Pile and Trench Wall Slopes and Angle of Internal Friction

Table 2.2 gives slope measurements for various dump piles in the workspace. Figures 2.6 and 2.7 show transects and profiles corresponding to each of these slopes. Dump piles have an average slope of 38°±5° (same mean is obtained whether or not a von Mises distribution [*Jones*, 2006] is assumed). The 95% confidence interval assuming a von Mises distribution is used for the estimate of error. The mean dump pile slope is taken to represent the angle of internal friction of the soil because cohesive bonds were

broken during the dumping action (clods broke up during sprinkle tests [*Arvidson et al.*, 2009]), however we do not believe that particle shapes were changed. In addition to dump pile slopes, we measured trench wall slopes. Well-lit trench slopes are used to determine an average trench slope value of 71°±10° (the 95% confidence interval assuming a von Mises distribution is again used for the error estimate). Furthermore, only side walls are used because they were the least affected by compression from the scoop since these walls were parallel to the direction of scoop motion. Table 2.3 gives slope measurements for various trench walls in the work space, and Figure 2.8 shows transects and profiles for the walls. Trench wall slopes are much larger than the angle of internal friction, and slope failure was not observed on these walls. This result indicates the presence of cohesive forces in undisturbed soils.

2.5 Method for Calculating Cohesion

In addition to the internal friction, cohesion affects the soil's resistance to excavation. The analysis in this section follows the methods of *Balovnev* [1983] to estimate soil cohesion, or shear strength. This technique has been investigated by workers concerned with lunar soils [*Wilkinson and deGennaro*, 2007]. Balovnev applied the theory of retaining walls to the walls of a scoop [*Balovnev*, 1983; *Blouin et al.*, 2001]. He considered draft, or horizontal force, to be made up of four parts: 1) resistance (to cutting) experienced by the blade, 2) additional resistance due to a beveled edge on the blade, 3) resistance (to cutting) experienced by the sides of the scoop, and 4) resistance (from friction) experienced by scoop sides. We neglect part three because scoop passes

were not deep enough for this to be a factor. The equations for the remaining parts of the horizontal force are as follows:

$$\mathbf{F1} = wz(1+\tan\delta\cot\beta)A_1\left(\frac{zg\rho}{2}+c\cot\phi\right)\hat{r} \tag{2.1}$$

$$\mathbf{F2} = we_b(1+\tan\delta\cot\alpha_b)A_2\left[\frac{e_b g\rho}{2}+c\cot\phi+zg\rho\left(\frac{1-\sin\phi}{1+\sin\phi}\right)\right]\hat{r} \tag{2.2}$$

$$\mathbf{F4} = 4\tan\delta A_4 l_s z\left(\frac{zg\rho}{2}+c\cot\phi\right)\hat{r} \tag{2.3}$$

where A_1=A(β), A_2=A(α_b), and A_4=A(π/2).

$$A(\beta) = \frac{\cos\delta\left(\cos\delta+\sqrt{\sin^2\phi-\sin^2\delta}\right)}{1-\sin\phi}\exp\left\{\left[2\beta-\pi+\delta+\sin^{-1}\left(\frac{\sin\delta}{\sin\phi}\right)\right]\tan\phi\right\} \tag{2.4}$$

where w is blade width, z is depth between passes (i.e. excavation depth), δ is the soil-scoop friction angle, β is the rake angle, φ is the soil friction angle, g is Mars gravity, ρ is bulk density, c is cohesion, e_b is the height of the blunt (beveled) edge, α_b is the angle of the blunt edge, l_s is the length of a scoop side, and $\hat{r}$ indicates that the listed contributions to the force are all in the horizontal, radial direction.

Here we compare horizontal force values resulting from the above equations to the horizontal force returned in the RA telemetry in order to obtain soil cohesion values.

The first excavation in Snow White is used to illustrate the procedure for determining cohesion.

Some assumptions are made in order to attain cohesion values. 1) The scoop blade angle varied along the length of each trench as it was being excavated. For example, for the first excavation into Snow White, the angle varied from 123.2° to 169°, with an average of 147.3° (to obtain rake angle, this value as well as values given for other trenches must be subtracted from 180°). This average value is used in calculations, and the angle of the beveled end of the scoop blade is also taken into account (see Figure 2.5). The scoop blade is at an angle relative to the rest of the scoop, but its angle is used in calculations of cohesion because the thickness of each tract of soil being excavated in a single pass is generally less than the scoop blade length (some sample acquires are exceptions). 2) The angle of external friction (soil-scoop friction) is assumed to equal the angle of internal friction as it is assumed that after the first excavation the scoop was no longer clean. 3) Density is assumed to be 1.235 g/cc from Thermal and Electrical Conductivity Probe observations [*Zent et al.*, 2010] (uncertainty in this value is due to instrument error as well as to the following assumptions: basaltic mineralogy, no soil disturbance from needle placement). This density value is consistent with the density *Moore and Jakosky* [1989] found for similar crusty to cloddy soil at the Viking landing sites [*Arvidson et al.*, 2009]. Deviations from this value are taken into account in the calculation of the uncertainties. 4) The depth between passes is taken from the parameter set used in commanding the RA. Other values used include: gravity (3.76 m/s^2), blade width (8.6 cm), beveled edge thickness (0.093 cm for a horizontal blade), beveled edge

angle to rest of blade (34.8°), and side length (11.4 cm). *Balovnev* [1983]'s equations give horizontal force required to excavate through soil of a given cohesion. We solve his equations for cohesion so that we can work backward and use the horizontal force values (Fr – force in the direction of excavation) returned by the RA to obtain the soil cohesion. Only negative forces are used in the Fr distributions because the negative direction in the RA coordinate system is towards the RA shoulder (i.e. towards the lander) and the backhoe motion of the RA is towards the lander as well. Positive values are most likely rebound values due to the fact that the RA is a mechanical system; so positive values are ignored since they do not reflect soil properties. If excavation activity involved significant accommodation, data points from the section of the trench where this happened are removed before horizontal force is averaged. Table 2.4 gives cohesions for various trenches in the workspace, uncertainties in cohesion, values of the various contributions to force described earlier, and values of certain other parameters used to calculate cohesion. Uncertainty in horizontal force, density, rake angle, angle of internal friction, depth between passes, and gravity estimate are taken into account in the error propagation calculations. The uncertainty in horizontal force results in the largest contribution to the uncertainty in cohesion; uncertainty in angle of internal friction gives the second largest contribution. Note that the uncertainties in cohesion are larger than the calculated values. While this means that there is no reliable lower bound (other than 0 kPa) for those values, it still gives the most likely value as well as an upper bound. Furthermore, the relative error in cohesion values is less than the absolute error given here. In general, higher uncertainty values are obtained when using excavation models to

determine cohesion, as opposed to using a direct shear test, which is relatively impractical for a planetary mission; for an example of uncertainties resulting from modeling a similar process, see *Moore and Jakosky* [1989].

2.6 Analysis of Payload Interoperability Testbed (PIT) Experiments

Before discussing the cohesion of the landing site soil, we present results from laboratory testing in a loose soil over a hard icy soil simulant. Figure 2.9 shows the RA trajectory for the first excavation in the University of Arizona Payload Interoperability Testbed (PIT) icy soil simulant trenching test conducted with an engineering model of the spacecraft. During each pass of the trenching activity, the scoop moved from the far edge of the trench towards the depth-axis or z-axis (which intersects with the RA shoulder at depth= 0 m). This means that, in Figure 2.9, as well as in all of the trajectories that will be shown in this paper, the RA scoop comes down on the right side of the figure, travels through the soil, and then turns upward and is elevated out of the trench when it gets to the left side of the figure. Most of this first excavation was through the soil simulant used to cover the hard icy soil simulant. The Mars soil simulant used was poorly sorted basaltic soil (silt-sized up to 150 micrometer diameter particles with sand being the predominant fraction) that retained its shape after compression; this was due to the fine grain fraction which fills in the pore space giving the soil an apparent cohesion. The method of Balovnev yields a cohesion of $0.4^{+0.7}_{-0.4}$ kPa (Table 2.4) for this soil. This soil is shown in Figure 2.10 as the darker soil in the upper layer, above the lighter-toned material representing the hard icy soil simulant. The lineations, or chatter marks, in the

figure are due to interaction of the soil with the RA during excavation. Note that lineations such as this have also been seen on the floors of trenches at the landing site [*Arvidson et al.*, 2009]. When the RA reached the lighter-toned icy soil simulant, it could not penetrate into the simulant with the scoop blade and instead underwent stick-slip motion where it skittered across the surface. Figure 2.10 shows that higher forces resulted when this happens. This same stick-slip motion occurred when the RA scoop blade passed over the surface of icy soil at the landing site, so an icy soil rasp was used to penetrate and acquire icy soil [*Arvidson et al.*, 2009].

2.7 Analysis of Excavations

2.7.1 Excavation at the Side of a Polygon

Both the first touch, which consisted of pressing the bottom of the RA scoop into the soil, and the first excavation into the soil at the landing site were conducted on the side of a polygon at the site of what is now a trench named DodoGoldilocks (Figures 2.1-2.2). For analysis of soil on the side of a polygon, we used a trench named Upper Cupboard (which was excavated immediately to the east of the DodoGoldilocks trench) because its excavation was conducted at more frequent depth intervals and more data points were obtained than for DodoGoldilocks; therefore, it gives a better indication as to the strength of the soil. Figure 2.11 shows the trajectory with force values for the first excavation of Upper Cupboard trench, conducted on sol 67. Forces grade from high to low as the location of the scoop progresses away from the deeper section of the far end of the trench. The RA went into safe mode in that area of the trench, and was covering most

of the exposed ice when the trench was imaged. However, in an image from a later sol, the location of the ice was found to correspond to the location of many of the highest force values (Figure 2.12). Therefore, the relatively pure ice found in Upper Cupboard (and in DodoGoldilocks) has a significant effect on the strength of the soil located in the same section of the trench. This soil has a cohesion of $0.6^{+1.2}_{-0.6}$ kPa (Table 2.4). Any chunks of ice that may have been excavated would have affected this value. Soil on the opposite side of the trench has a cohesion of $0.2^{+0.4}_{-0.2}$ kPa. See Table 2.4 for parameters used in the calculation. For rough comparison, loose, granular material has a similar cohesion to the values listed in Table 2.4 [*Scholtes et al.*, 2009].

2.7.2 Excavation at the Center of a Polygon

On the first sol that we trenched in the center of a polygon (Wonderland polygon mound), icy soil was revealed and verified spectroscopically [*Blaney et al.*, 2009]. The icy soil (seen in Snow White trench, Figure 2.13) is believed to correlate with accommodation seen in the RA trajectory, and this is used to differentiate between icy and relatively non-icy soils in the RA force data. Two excavations were conducted in Snow White on Sol 22 (the first sol of RA activity in this region). For the cohesion calculations, force values taken from the first excavation (maximum depth below surface: 3 cm) are used to represent shallow soil; calculations using these values result in a cohesion of $0.6^{+0.8}_{-0.6}$ kPa. The deep soil force data are taken from the second excavation (3-5 cm depth below surface) and result in a cohesion of $1.2^{+1.8}_{-1.2}$ kPa. However, even before the RA began its second excavation, there was a change in soil cohesion; this can

be seen through a decrease in scoop velocity as the excavation progressed (See Table 2.5). Velocity is calculated from position and time data returned by the RA. Of the net 2 cm/s velocity decrease over the ten passes analyzed, 1.7 cm/s velocity change occurred over the course of only three passes (passes 5-7). This corresponds to the depth at which we start seeing higher forces [*Arvidson et al.*, 2009, Figure 2.19] that are not associated with accommodation. This change is abrupt and velocity does not change appreciably from pass to pass in the second excavation into Snow White (on the same sol). The previous example of Upper Cupboard trench indicates that we would expect a more gradual gradient if this were due to proximity to the ice table. As will be discussed in a subsequent section of this paper, we do also see a gradual gradient that appears to be related to proximity to ice at Snow White; this change appears in the form of an angled gradient in force.

Both the first and second trenching activities conducted on Sol 22 in Snow White exhibit accommodation and therefore both encountered icy soil corresponding to the ice table. We can see this from the higher forces experienced by the RA in an area towards the foot of the trench where the trajectory measurements also show the arm moving higher in elevation, i.e. experiencing accommodation (Figure 2.14). Force values show that the ice table is uneven, despite trenching on relatively flat land at the top of a polygon. The post-trenching image also shows this pattern (Figure 2.13). For regions where the RA encountered icy soil that it cannot penetrate, spectra indicate 30% ice and 70% soil [*Cull et al.*, 2008]. We do not present cohesion values for this icy soil (beneath the ice table) because the RA was not able to excavate into that material with the scoop

blade. If data points for which the arm accommodated to this icy soil are excluded, we can still see that the overlying soil at Snow White has relatively high cohesion, i.e. the material in Snow White is generally more difficult to trench than material at the sides (Upper Cupboard trench) and troughs (Stone Soup & La Mancha trenches) of polygons. This may be partially due to a higher level of soil processing on polygon mounds, but appears to be closely related to the proximity of the ice table. This effect can be seen in Figure 2.14, where there are higher forces in the foot of the trench (the area where the icy soil causes arm accommodation at the floor). These forces are evident right up to the surface in this section of the trench. This effect may be due to the RA encountering more pore ice or more adsorbed water as it progresses closer to the impenetrable icy soil.

2.7.3 Excavation in a Deep Trough

On the opposite side of the terrain elevation spectrum from Snow White trench, the Stone Soup trench is located in a polygon trough. During the first four sols of trenching activity in Stone Soup, the RA scoop alternated, first trenching along the right, then trenching along the left of the trench. Each sol's activity consisted of ~12 passes along each side of the bottom of the trench. In order of depth below the surface (also sol order), calculated cohesions for Stone Soup are: $0.3^{+0.5}_{-0.3}$ kPa, $0.2^{+0.5}_{-0.2}$ kPa, $0.3^{+0.5}_{-0.3}$ kPa, $0.3^{+0.7}_{-0.3}$ kPa (Table 2.4). Taken together, the cohesions, and especially the force distributions (Figure 2.15), from the latter two sols show that force increased with depth. However, there is no spectral confirmation that the scoop ever reached the ice table since the floor of the trench was in shadow (also note that the RA did not experience

accommodation). Figure 2.15 shows the variations in the force profile of the trench (from first four sols of excavation). The scoop may have hit part of the ice table or a hard soil clod at the bottom of the trench's head wall, where the figure shows exceptionally high forces, exceeding 100 N.

2.8 Slope Stability Analysis

A slope stability experiment was conducted near Stone Soup, at the southern portion of the western wall of DodoGoldilocks. This was the only location where a wall was stressed with the intent to initiate slope failure (Figure 2.16). Despite the application of ~75 N vertical force with the bottom of the RA scoop, slope failure was not observed on the wall. We can therefore use this experiment to estimate the minimum amount of cohesion the soil must have in order to withstand the applied stress. This is the cohesion at which the stressed wall would have a Factor of Safety (FoS) of unity. GALENA [*Clover Technology*, 2006] slope stability modeling software was used to model stresses and slope failures using limit equilibrium analysis on a 2D slope with a Mohr-Coulomb soil description. Properties and bounds defined in the model include: cohesion (varied), angle of internal friction (38°), unit weight (1235 kg/m^3 * 3.76 m/s^2 = 5.264 kN/m^3), slope failure type (circular or non-circular), failure surface bounds and radius, stress value, extent of stressed area, and analysis type (Spencer or Bishop analysis [*Spencer*, 1968; *Bishop*, 1955]). Varying analysis type did not change the results significantly. Neither did taking into account the presence of a harder subsurface layer. Multiple forward analyses were conducted on the model until the surface with a FoS just above 1

(the critical failure surface) was found, however this surface is a trivial case (Figure 2.17, bottom); if failure occurred at this surface, it would not be identifiable in digital elevation map data. A spectrum of failure surfaces from one that would not be noticed to one that involves the whole area of material under the scoop were investigated (Figure 2.17) and yield a range for minimum cohesion from <0.01 kPa to ~1.9 kPa. This indicates that uncertainty in the failure surface provides the largest source of uncertainty in the minimum bound for cohesion.

Figure 2.18 shows an intermediate case that gives a minimum cohesion estimate of ~0.9 kPa. For context, Figure 2.19 gives two profiles of the wall slope, one slightly to the north of the other. Both profiles yield similar results. The profiles of the resulting imprint of the scoop are also included in the figure and show the change in topography resulting from pressing the scoop on the wall. Because of this change in topography, it might be possible for a failure to have gone unrecognized: for example, if the soil slid only a small distance along the failure surface and then the scoop continued to compress the soil. However, there is no evidence for this sequence of events. From the image data, it appears that the scoop flattened the wall, causing it to compress and crumble, but not causing any large-scale movement of a coherent mass. After uncertainty in failure surface, the next two largest quantifiable sources of uncertainty in cohesion are the uncertainties in angle of internal friction and measured stress values; together they give an uncertainty in cohesion of about ~0.7 kPa. Unquantified sources of error in this slope stability method include the fact that this method does not take into account inhomogeneities present in the soil, it is not time-dependent (i.e. does not account for the

scoop pressing on higher-elevation soil before lower-elevation soil), does not account for the presence of the southern trench wall (i.e. limitations of 2D model), and ignores the effect from the scraper blade on the bottom of the scoop (the scraper blade caused some additional disturbance of the soil). The resulting range in cohesion from quantifiable uncertainties overlaps with that for surface soil at Stone Soup ($0.3^{+0.5}_{-0.3}$ kPa) obtained through Balovnev's method of analyzing excavation.

2.9 Excavation in a Shallow Trough

The RA was also able to excavate a trench (La Mancha) in a unique location: a low-elevation area in between two polygons forming a shallow polygon trough. Four sols involved excavation activity in La Mancha: sols 127, 132, 134, and 148. Sol 148 resembled a scrape, rather than an excavation, even though the scoop blade was used instead of the scraper blade. The scrape was commanded because it was expected that the RA was close to encountering the ice layer after sol 134's activity. Figure 2.20 shows the force distribution for the eastern swaths from both sols 132 and 134. Although the soil at La Mancha has structure, Balovnev's method can only give an "effective" or "bulk" cohesion. This "apparent" cohesion was calculated for soil located 0-6.5 cm below the surface at La Mancha trench: $0.2^{+0.5}_{-0.2}$ kPa (Table 2.4). La Mancha's value of cohesion is similar to the cohesion values of soil at Upper Cupboard and Stone Soup trenches. This result is surprising because images show that La Mancha is the only trench from which the RA excavated large platy slabs of soil (see Figures 2.21 and 2.22), although some clods were excavated from other trenches. These plates have been

identified as spectrally similar to nearby surface soil exposures [*Blaney et al.*, 2009]. A likely explanation for why the RA forces are lower than expected in this region comes from the layered, platy structure of the soil. In between the layers there are planes of weakness along which the material cracked when the RA conducted its excavation. The planes of weakness appear to be parallel to both the direction of excavation and the original surface of the ground. The plates themselves appear hard, as can be seen in Figure 2.21, where chatter marks are evident on a separated slab. Chatter marks were not seen on weakly cohesive, but morphologically similar slabs observed during laboratory testing [*Arvidson et al.*, 2009].

It is important to consider all possibilities for the origin of these platy slabs: 1) an isolated hard pan layer that could be cemented by carbonates or silica, 2) layer similar to the platy-textured soil found on Earth and considered to be a typical cryogenic feature [*Van Vliet-Lanoe et al.*, 1984]; these textures are formed by freeze-thaw above an ice lens or ice vein and are relatively permanent as far as soils are concerned; formation is aided by desiccation as cryosuction moves water slowly towards the underlying ice, 3) structures formed by vertical compression due to ice lens formation, and 4) layer formed when ice in troughs lasts long enough into spring for thin films of water to form; the area later dries leaving behind a cemented pan. It is not possible to choose among these varying hypotheses based solely on morphological evidence. The fact that the material just below where we observe the platy textures at the Phoenix site has been spectrally identified as icy soil [*Diana Blaney*, personal communication] lends support to hypothesis 2. A significant constraint on the formation mechanism is the location of the

platy soil in one of two troughs at the landing site. At the other trough, Stone Soup, we did not achieve the depth of the icy soil interface, so we do not know if there was platy soil above that interface. The necessity for the formation mechanism for the platy material to be able to explain its occurrence in a trough, but not on mounds favors hypotheses 2 and 4. It indicates support for the role of an ice vein in the layer's formation since ice veins are commonly found in troughs in polygonal terrain on Earth. However, there is additional support for hypothesis 4 from the work of *Cull et al.* [2010], who find residual ice in troughs in the spring season; this makes hypothesis 4 the most likely mechanism.

2.10 Conclusions

Phoenix Robotic Arm telemetry, used in conjunction with landing site images, provides useful information about soil properties. The data allow estimation of soil cohesion at various locations within the landing site workspace, as well as an estimation of an average angle of internal friction for the site. The angle of internal friction is 38°±5° based on the angle of repose of disaggregated dump piles (assumed to be cohesionless). Mean cohesion values of *in situ* soils were calculated for a selection of trenches; these values range from between $0.2^{+0.4}_{-0.2}$ kPa to $1.2^{+1.8}_{-1.2}$ kPa with the highest soil cohesion at the center of a polygon mound. These cohesion values are consistent with the stability of steep trench walls. Of the three types of soil discovered at the Viking landing sites, the crusty to cloddy soil encountered by Viking Lander 2 best matches both the cohesion and the angle of internal friction of Phoenix soil [*Moore and Jakosky*, 1989].

Cohesion at the Phoenix site increases with proximity to the buried ice table as well as with proximity to relatively pure, penetrable ice. This is likely due to an increased presence of pore ice, adsorbed water, or both. A platy, or bladed, soil horizon was uncovered in a trough and probably formed via interactions with water. This soil did not require excavation forces of significantly different magnitude than those required by other soils at the landing site; this is due to the low inter-plate cohesion of the soil.

Figures

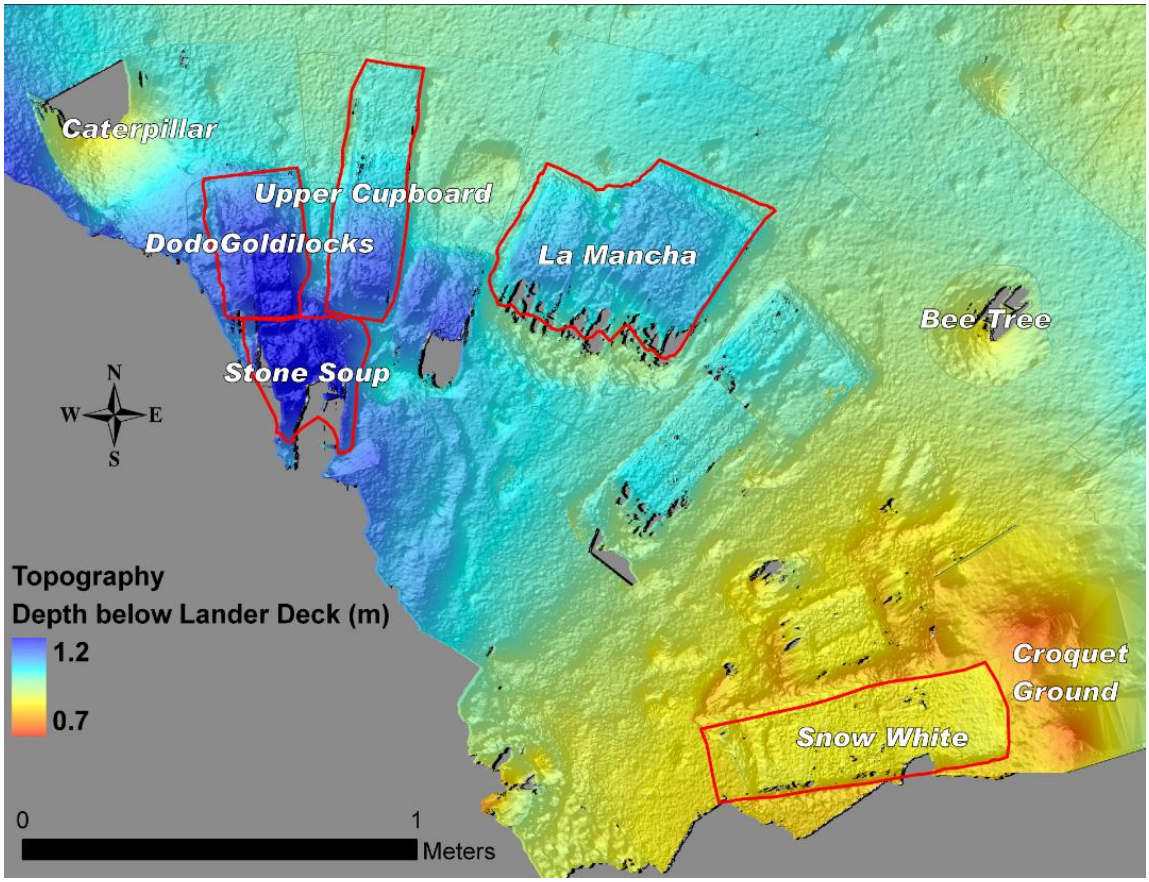

Figure 2.1. Phoenix landing site workspace elevation map after modification by RA. Trenches and dump piles were named after characters and objects in fairy tales and other stories. Trenches discussed in this paper have been outlined in red. The curve in the outline of Stone Soup trench is due to part of the lander blocking the view of the surface, and the outline of Lower Cupboard is blocked by tailings from Stone Soup. Note the lander footpad towards the lower center of the figure. DEM is courtesy of Hanna Sizemore.

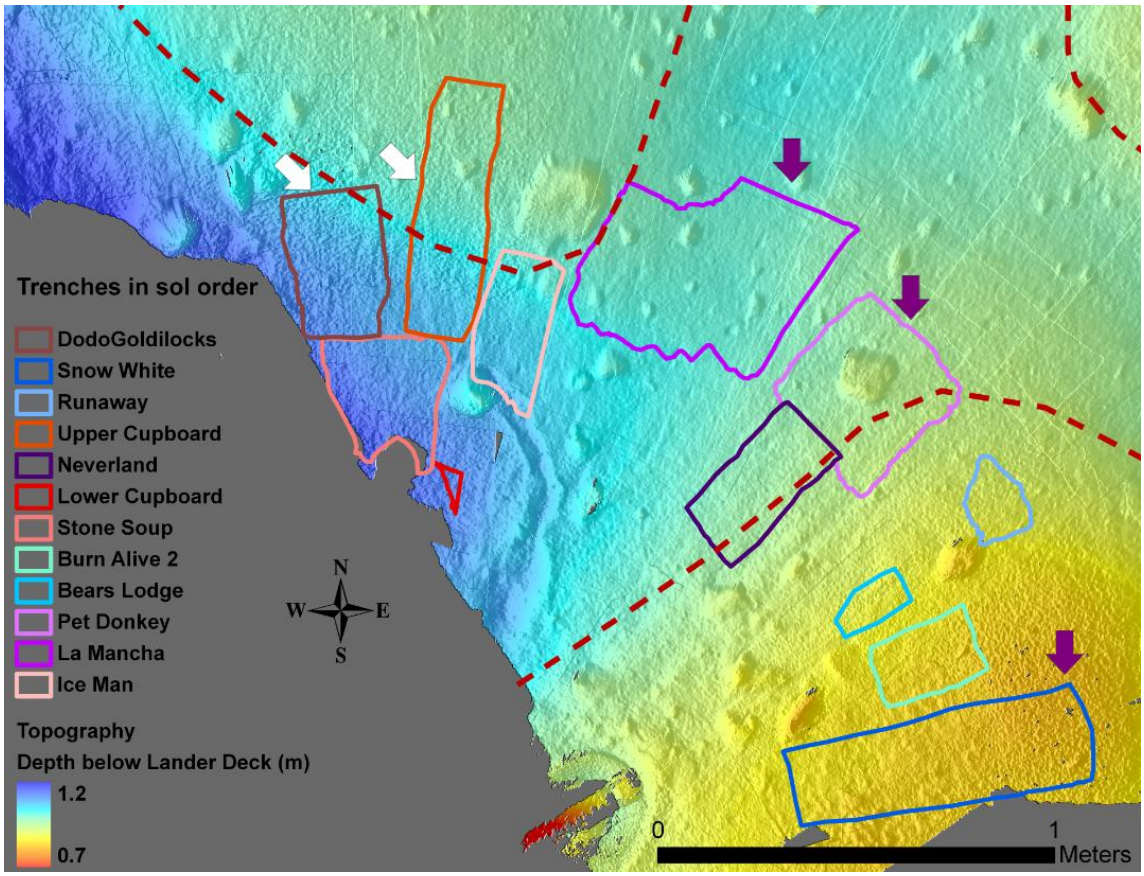

Figure 2.2. Phoenix landing site workspace elevation map before modification by RA. Dashed red lines show approximate polygon outlines. Here all trenches excavated during the mission are outlined. Trenches and dump piles were named after characters and objects in fairy tales and other stories. The curve in the outline of Stone Soup trench is due to part of the lander blocking the view of the surface, and the outline of Lower Cupboard is blocked by tailings from Stone Soup. Note the lander footpad towards the lower center of the figure. White arrows point to trenches in which relatively pure ice was found. Purple arrows point to trenches in which icy soil was found. DEM is courtesy of Hanna Sizemore.

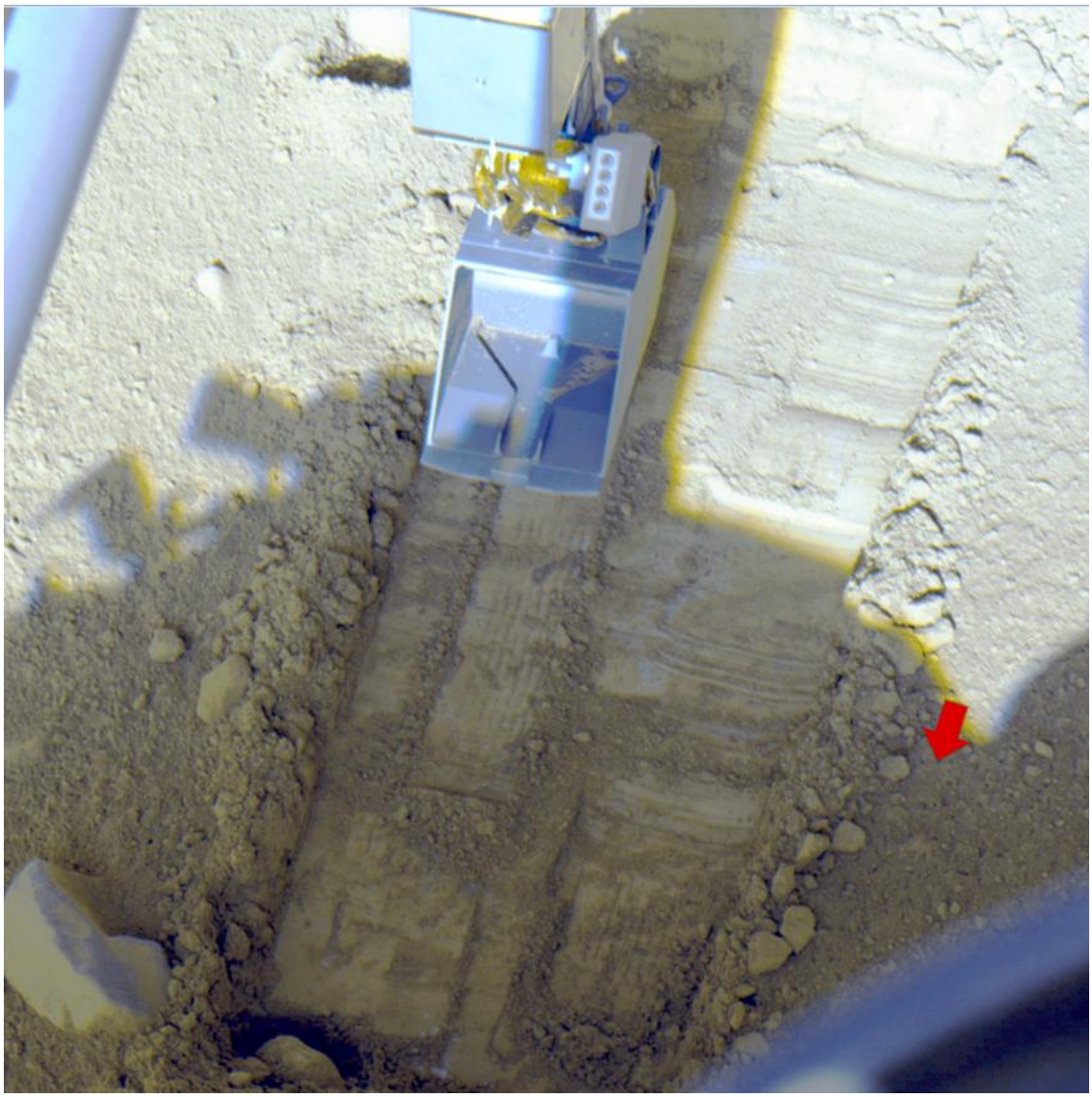

Figure 2.3. False color image of Robotic Arm (RA) scoop in Snow White trench. Red arrow indicates direction of lander as well as direction of scoop motion along the bottom of the trench. This convention will be followed to indicate the direction of the lander in subsequent figures. Surface Stereo Imager (SSI) image SS051IOF900751600_15C60L21TB.

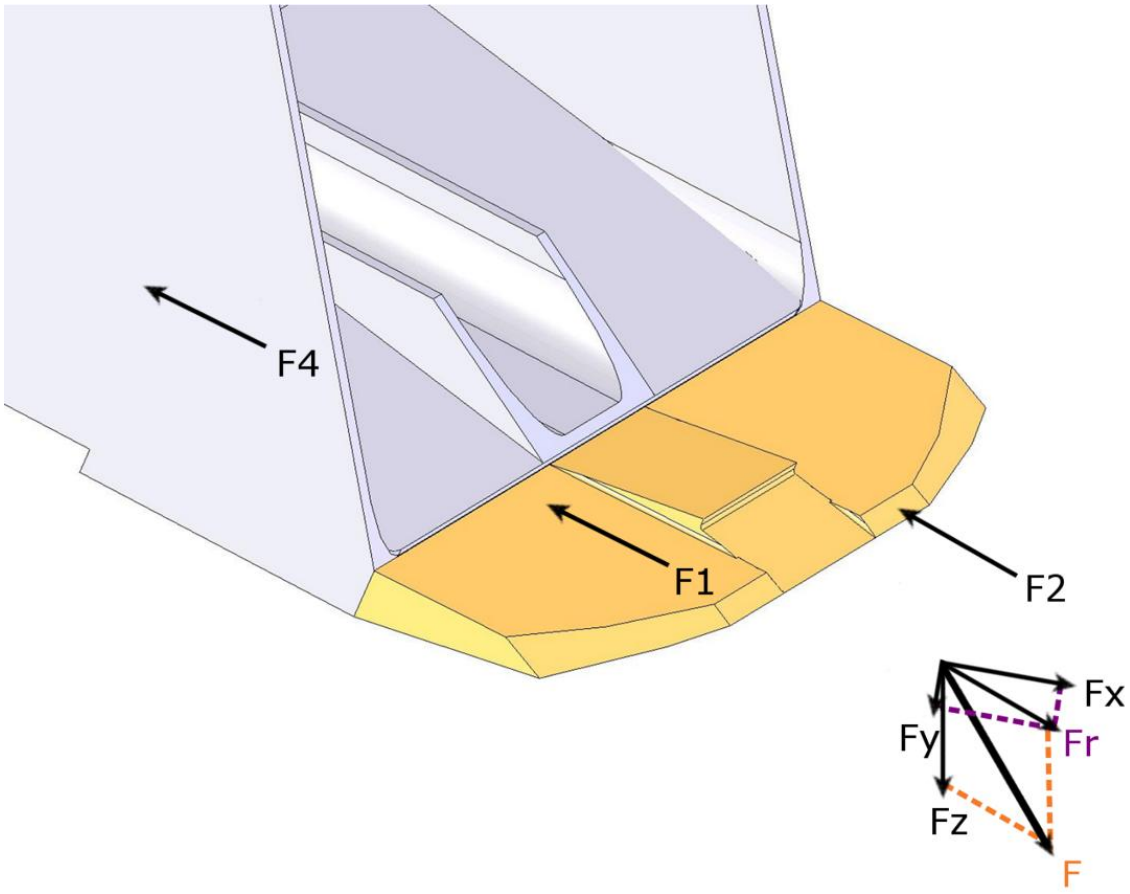

Figure 2.4. Schematic of the scoop with superposed vectors showing the direction of forces during excavation. Fx, Fy, and Fz are aligned with the coordinate axes. Fr is the vector sum of Fx and Fy. F is the vector sum of Fr and Fz. Also shown are F1, F2, and F4, the three contributions to horizontal force described in the section on calculating cohesion. F1, F2, and F4 have been lengthened for purposes of illustration, but in reality their magnitudes would add up to that of Fr.

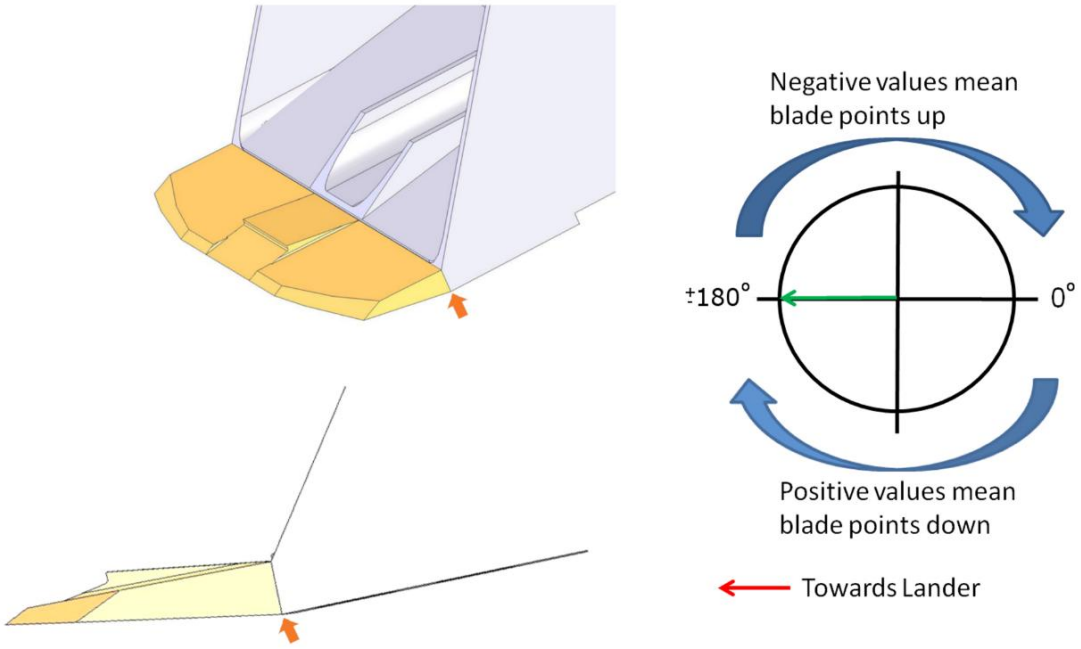

Figure 2.5. Schematics of the scoop. At top left is a 3D schematic of the scoop, and at bottom left is a 2D schematic side view. The orange arrows point to the same location on the scoop in each schematic. At right is a diagram of possible blade angle values with the green arrow indicating the orientation of the blade in the 2D schematic (blade level and pointed toward the lander).

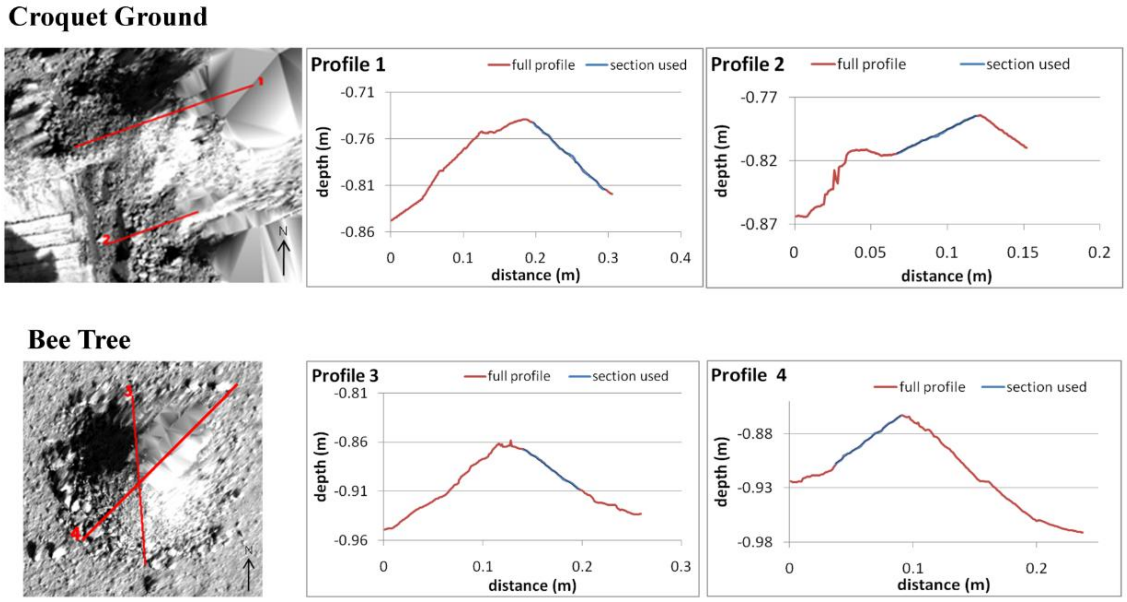

Figure 2.6. Profiles used to calculate slopes for Croquet Ground and Bee Tree Dump Piles (slope values are given in Table 2.2). The average of the dump pile slopes is then used as an estimate for angle of internal friction. Note that far sides of dump piles were not used since the SSI could not view them. SSI images SS108RAL905790842_0117EL1M1 and SS129RAL907652106_1EC26L1M1.

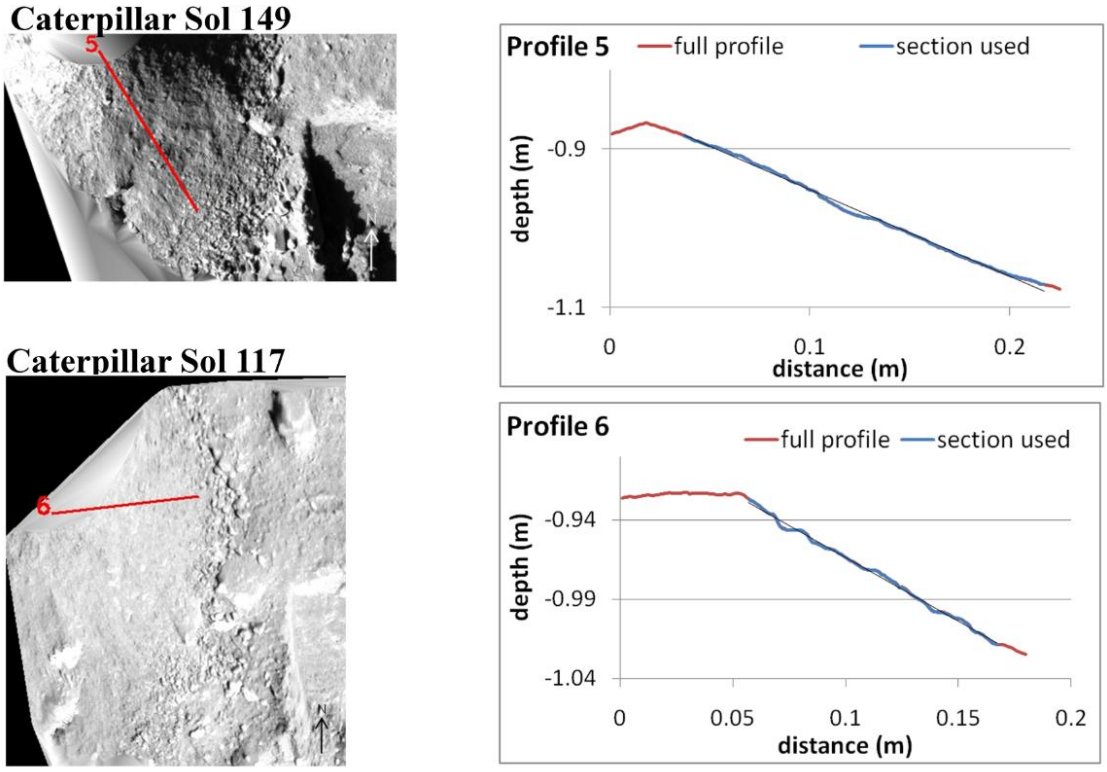

Figure 2.7. Profiles used to calculate slopes for Caterpillar dump pile (slope values are given in Table 2.2). SSI images SS149RAL909445554_207F6L1M1 and SS117RAL906588190_1D856L1M1.

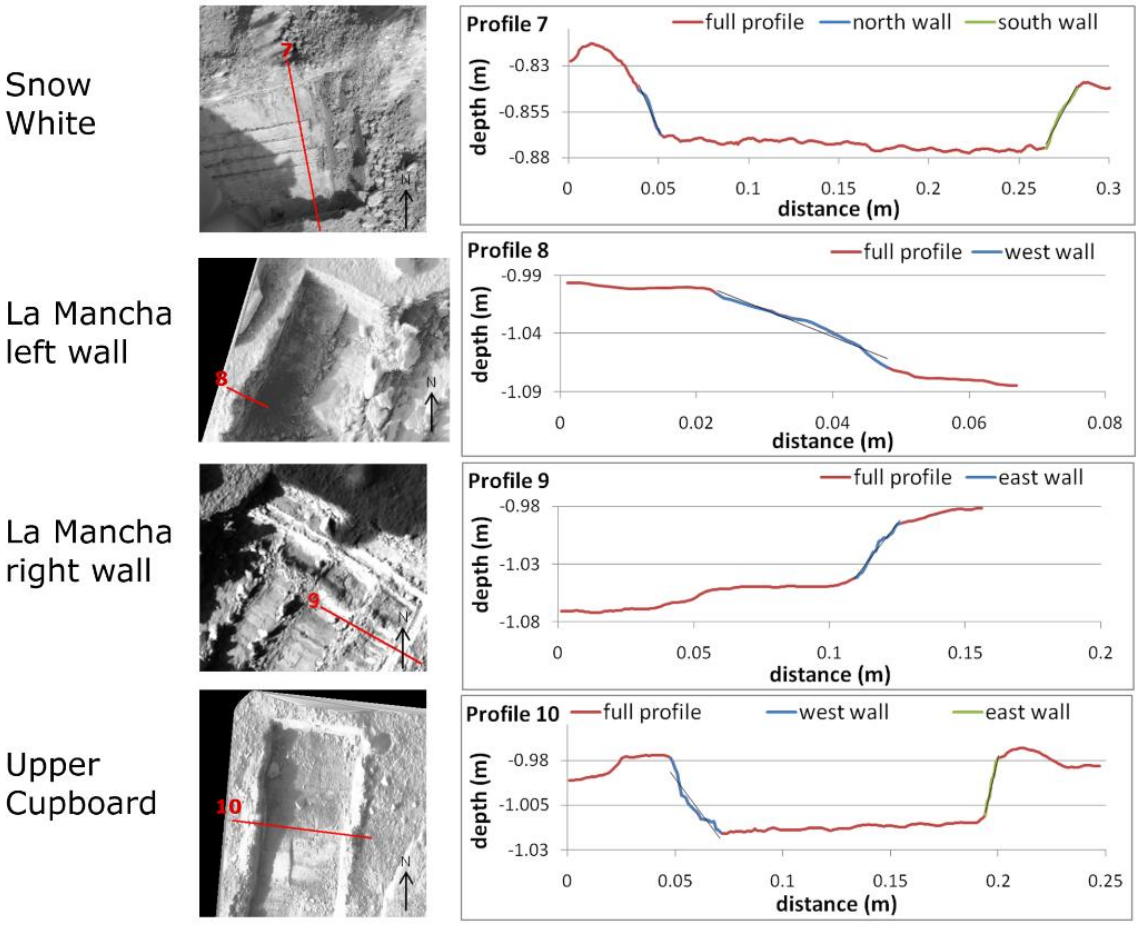

Figure 2.8. Profiles used to calculate slopes for trench walls (slope values are given in Table 2.3). SSI images SS108RAL905790842_0117EL1M1, SS148RAL909363043_20566L1M1, and SS147RAL909270572_20456L1M1.

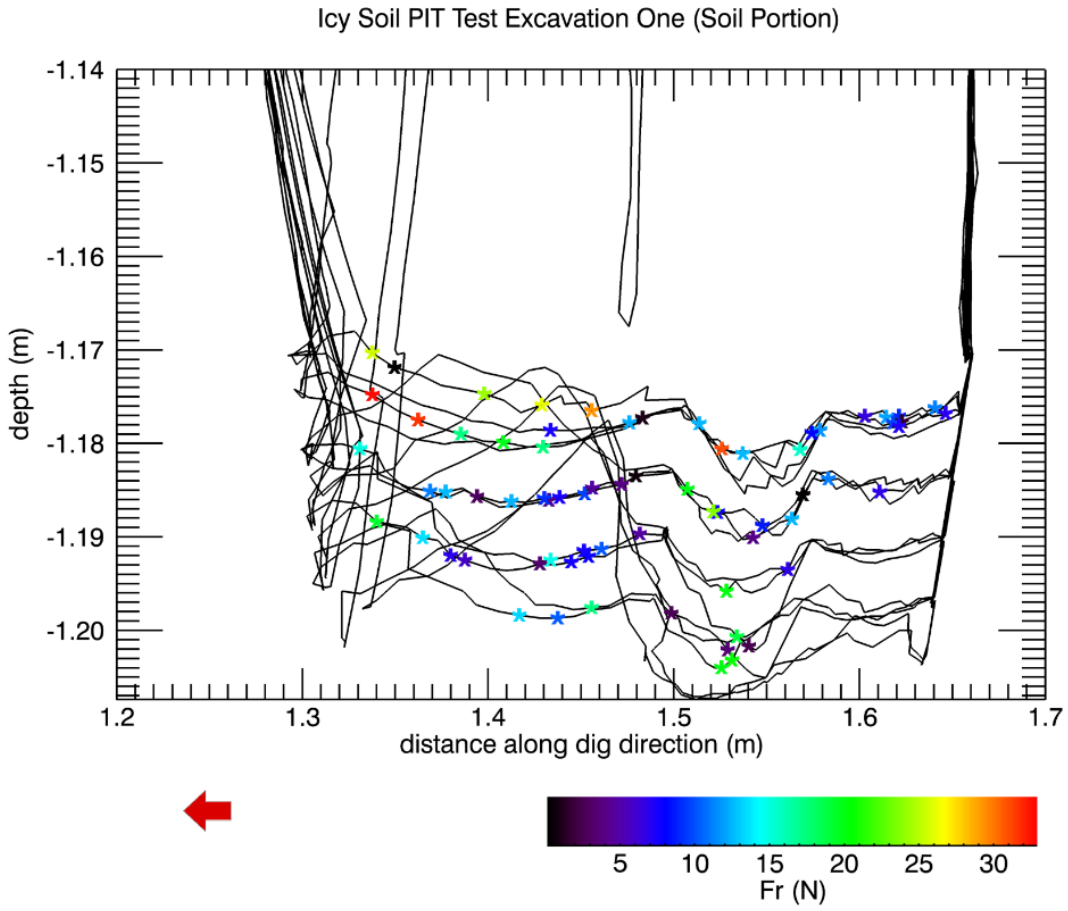

Figure 2.9. Excavation one of the Icy Soil PIT Test. The cement icy soil simulant is not actually encountered until excavation two (see Figure 2.10). Red arrow gives direction of lander. Vertical lines represent free-space moves where the scoop is entering or leaving the trench. The color-coded stars represent locations along the trajectory for which force data (in the direction of the lander) was returned. Note that force does not increase with depth or with proximity to underlying hard cement layer.

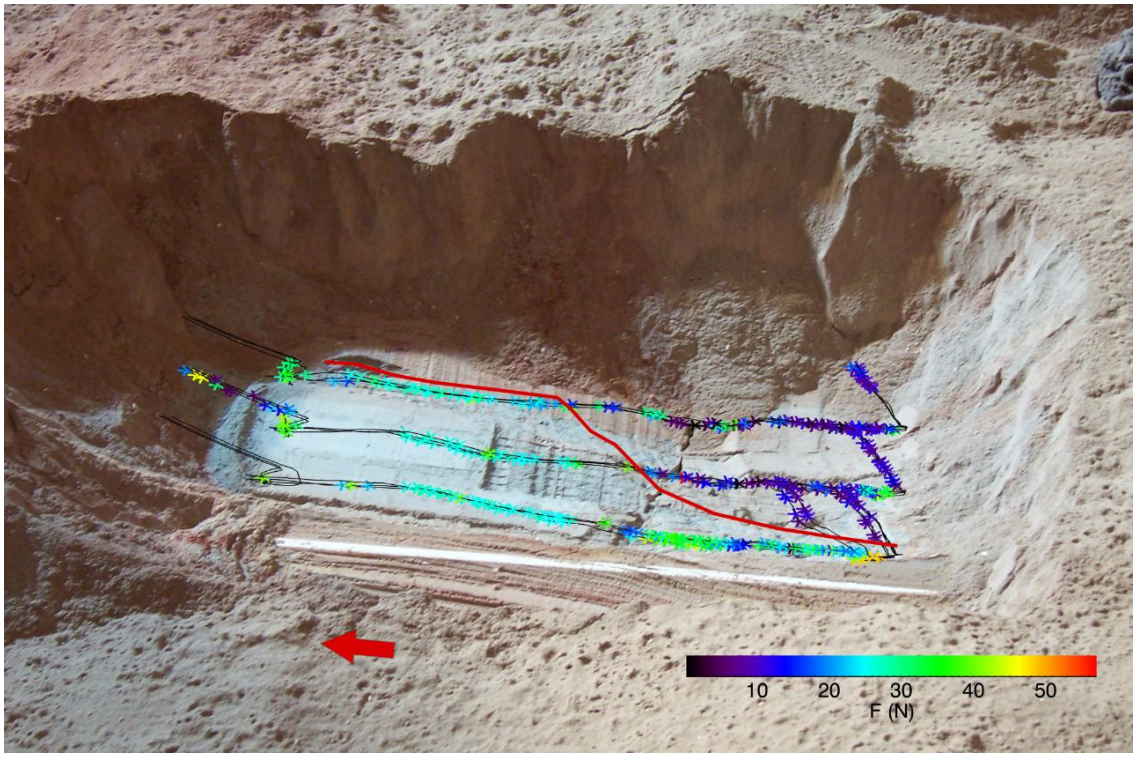

Figure 2.10. Laboratory testing which involved using the Robotic Arm to dig through Mars soil simulant and then buried cement icy soil simulant. The red line represents an approximate division between the two. Also shown is a close overlay of force values from part 2 of the excavation (part 1 is shown in Figure 2.9). As can be seen from the color-coded data points, forces are much higher over the icy soil simulant; this indicates the relative hardness of the material. Red arrow gives direction of lander. Note that additional tests were performed on this trench between when the force data was collected and when the image was taken, this includes activities that formed the deeper striations in the middle of the trench.

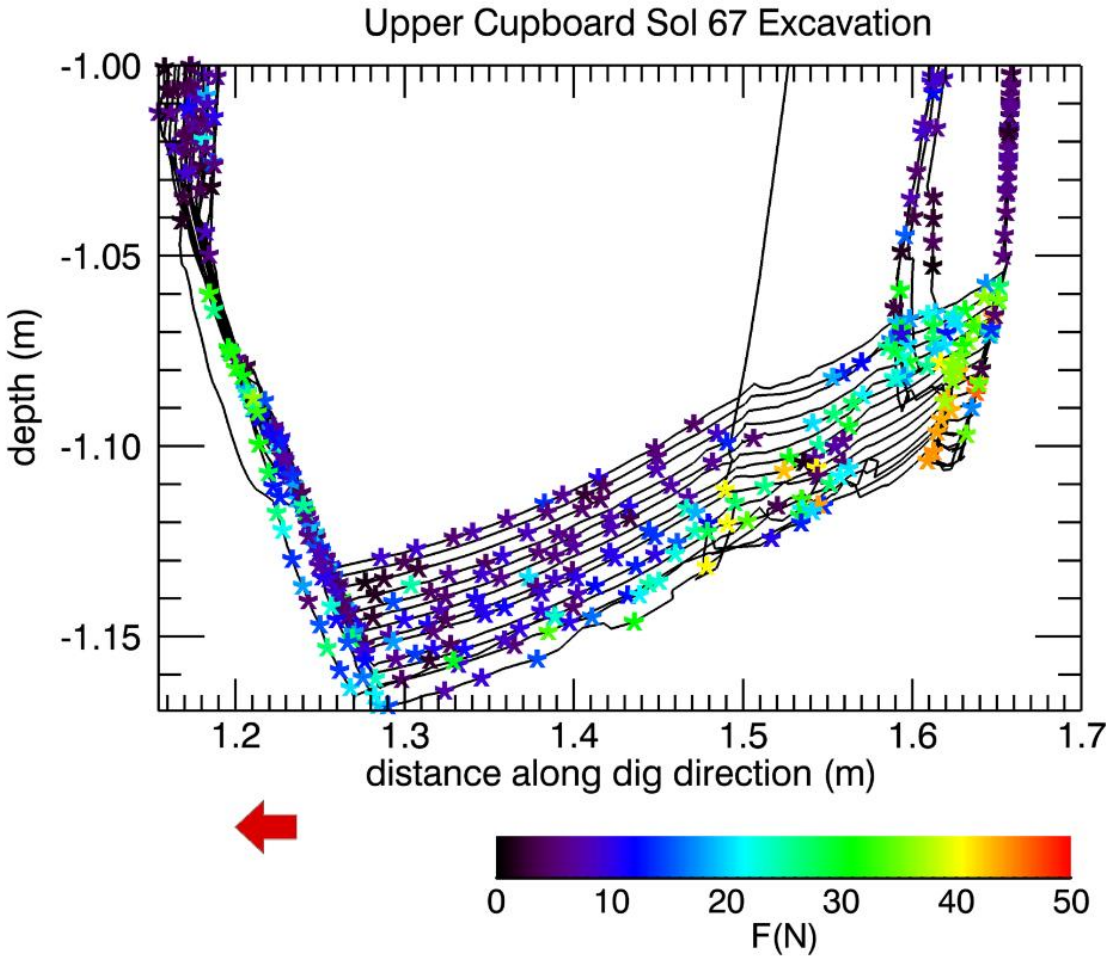

Figure 2.11. Trajectory color-coded by force for trenching in Upper Cupboard on sol 67. Red arrow gives direction of lander. Note the increase in force towards the lower far side of the trench (to the right of the figure) and compare with the location of ice in Figure 2.12.

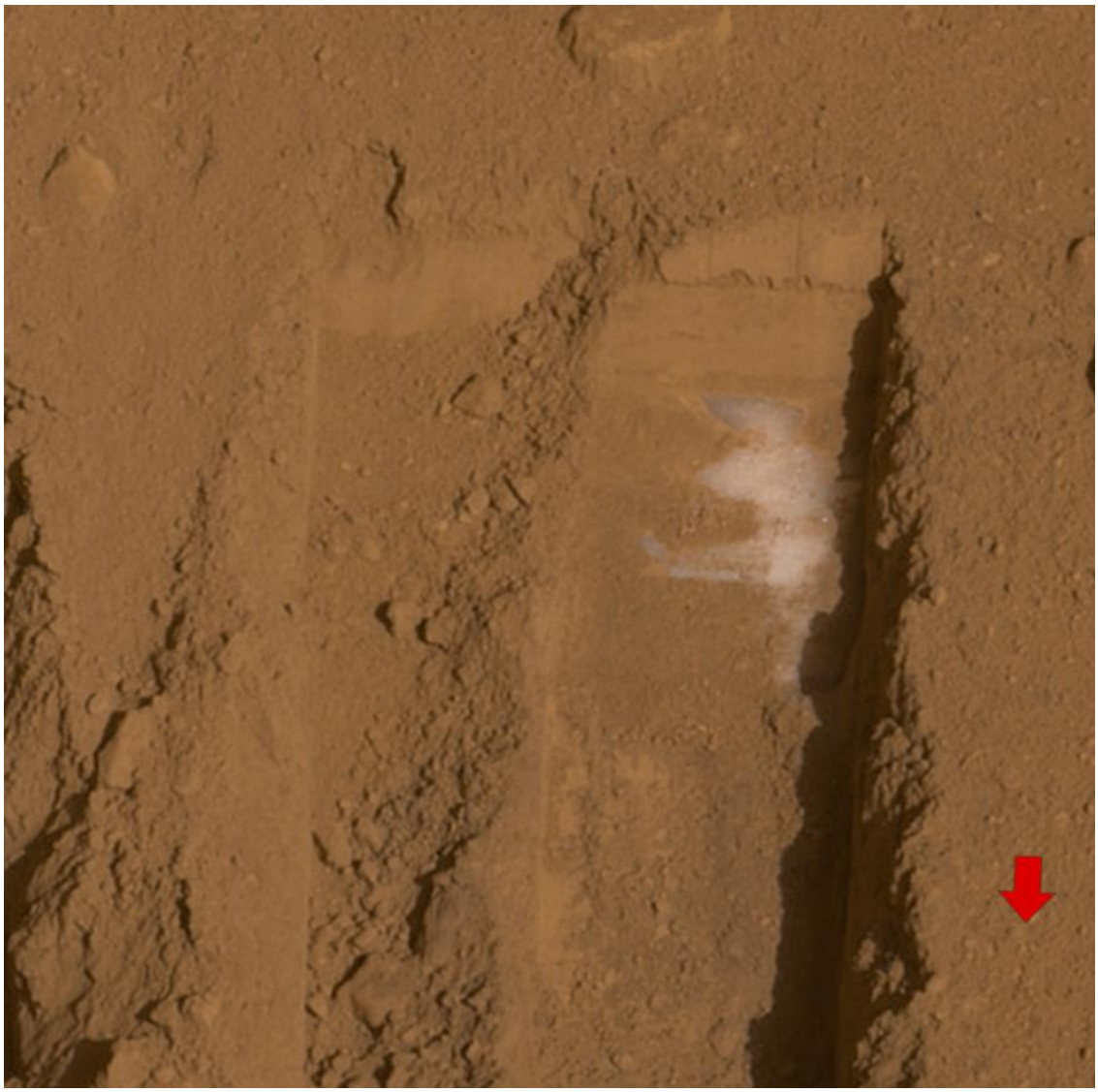

Figure 2.12. Upper Cupboard Trench. Ice is evident in the upper right section of the trench. Red arrow gives direction of lander. SSI image SS084IOF903660997_19CA0L21TB.

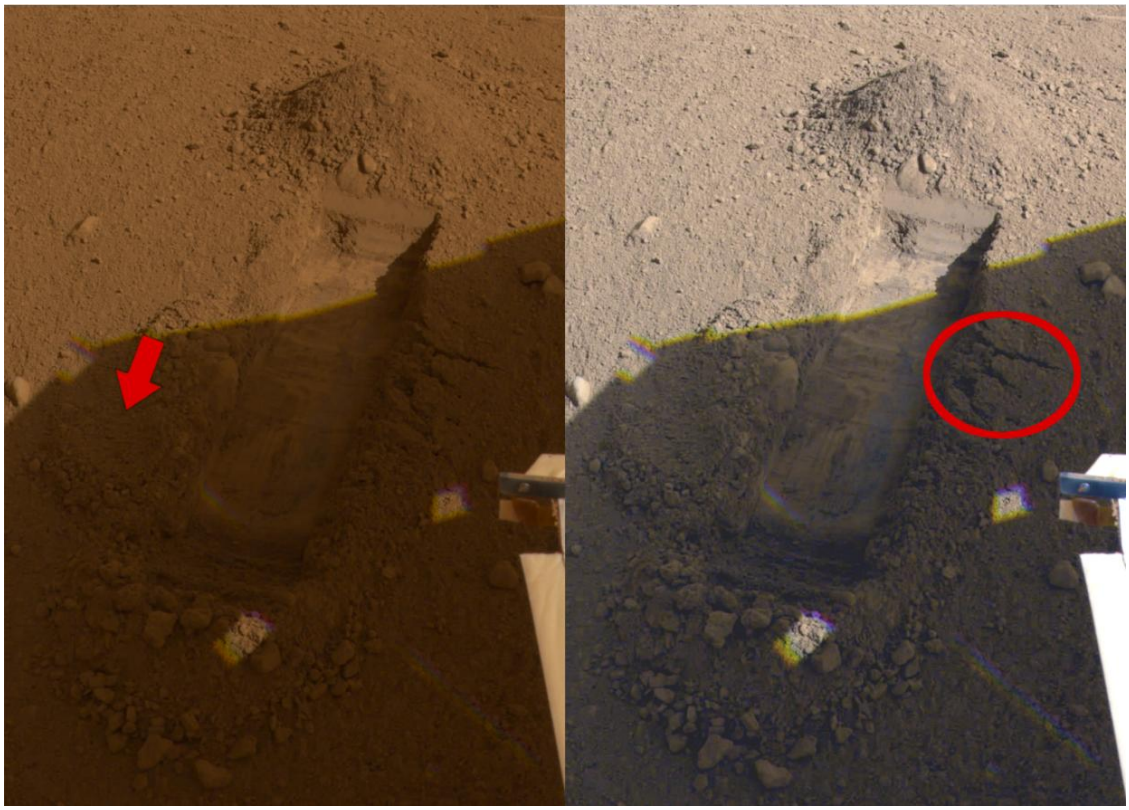

Figure 2.13. Snow White trench. At left, contrast has been sacrificed in preference for approximate true color. At right, a false color image (SSI filters 10, 11, and 12 [*Zamani et al.*, 2008]) gives a clearer view of darker areas of the trench floor that mark the presence of icy soil. A morphological expression of surface cohesion can be seen in the red circle. Red arrow gives direction of lander. SSI image SS022IOF898161657_12CAERCBA1TB.

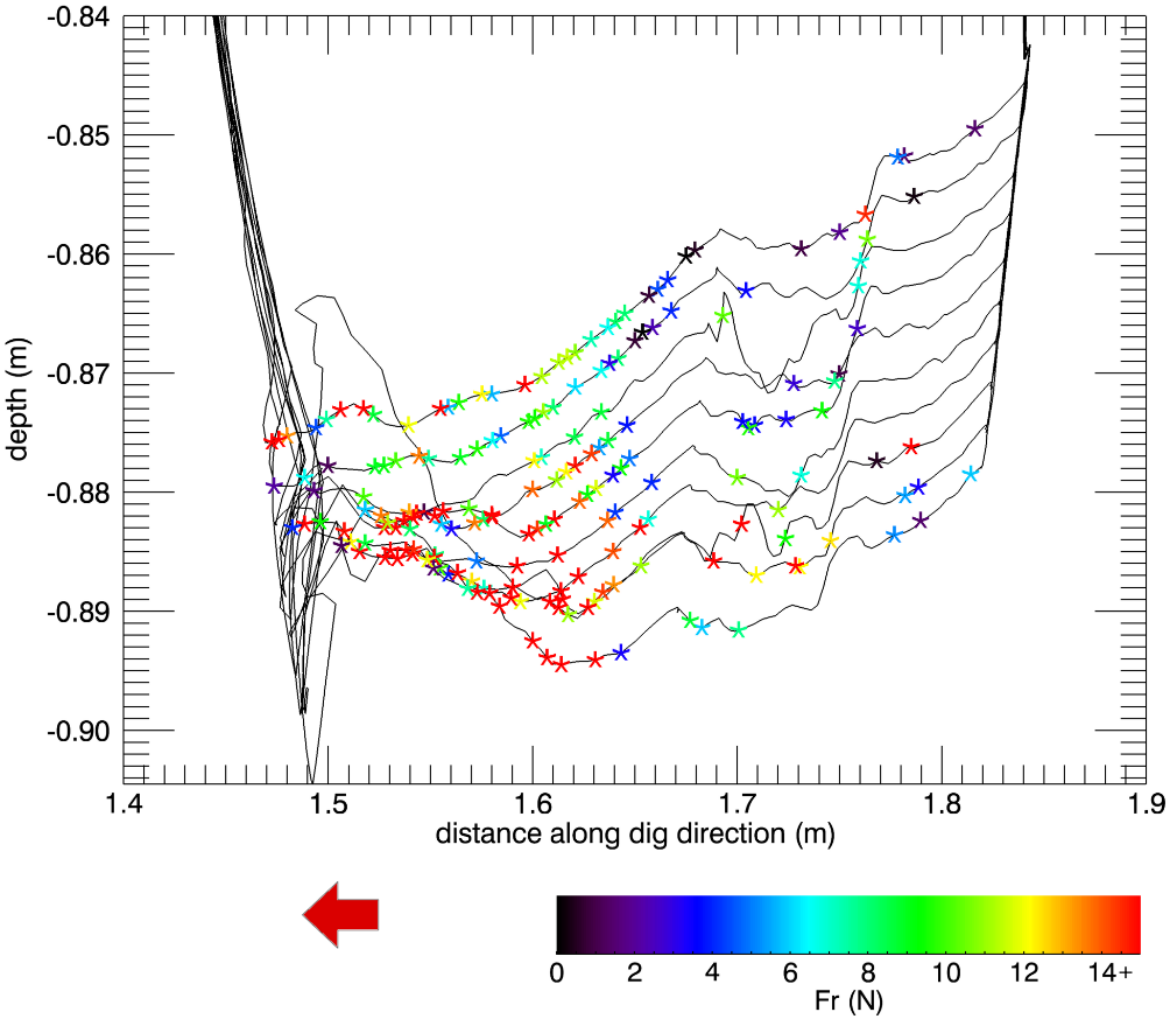

Figure 2.14. Trajectory followed by the RA in the first excavation in Snow White Trench. The stars represent locations along the trajectory for which force data (in the direction of the lander) was returned. Red arrow gives direction of lander. Note the higher forces on the landerward side of the trench, near the icy soil.

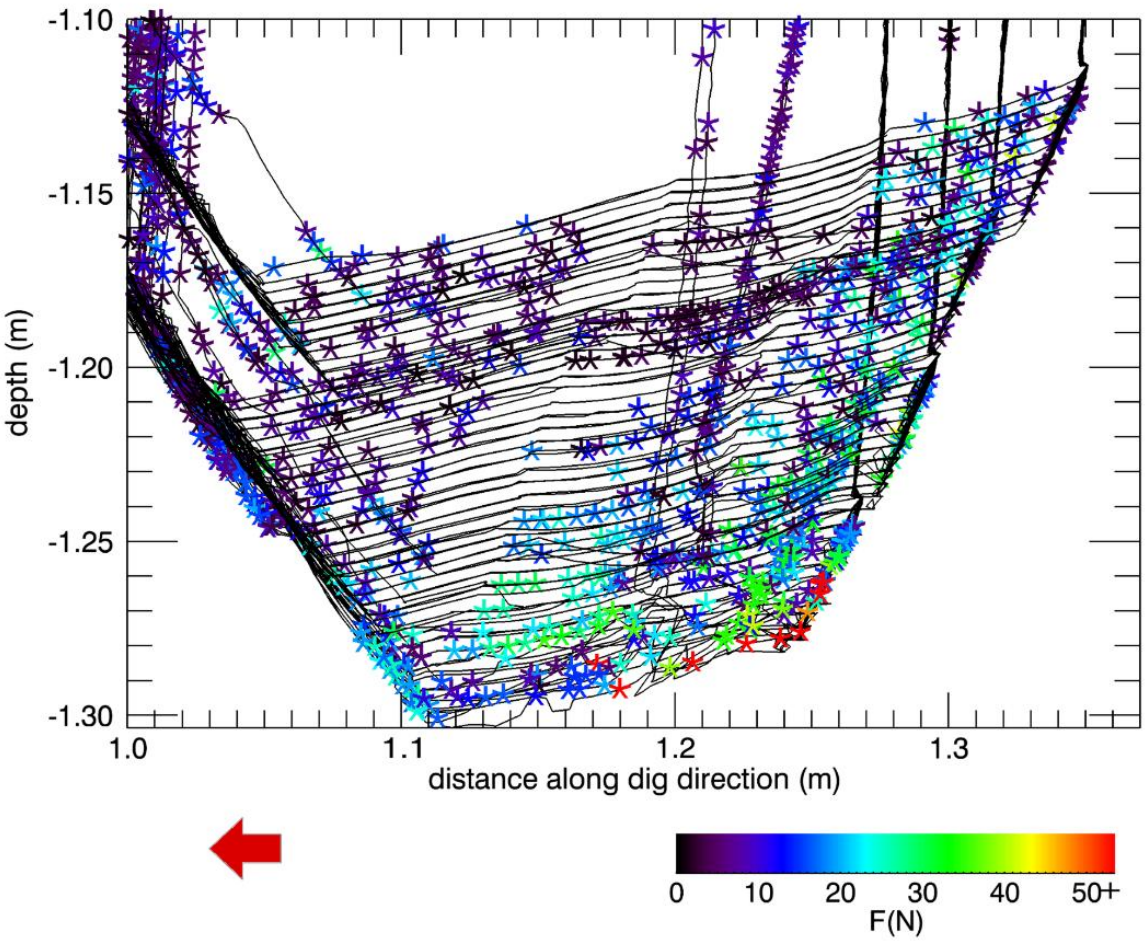

Figure 2.15. Trajectory color-coded by force for Stone Soup trench from sols 74, 76, 85, and 88. Force is the total force in the plane of excavation. Vertical lines represent free-space moves where the scoop is entering or leaving the trench. Red arrow gives direction of lander. Note the higher forces near the bottom of the headwall.

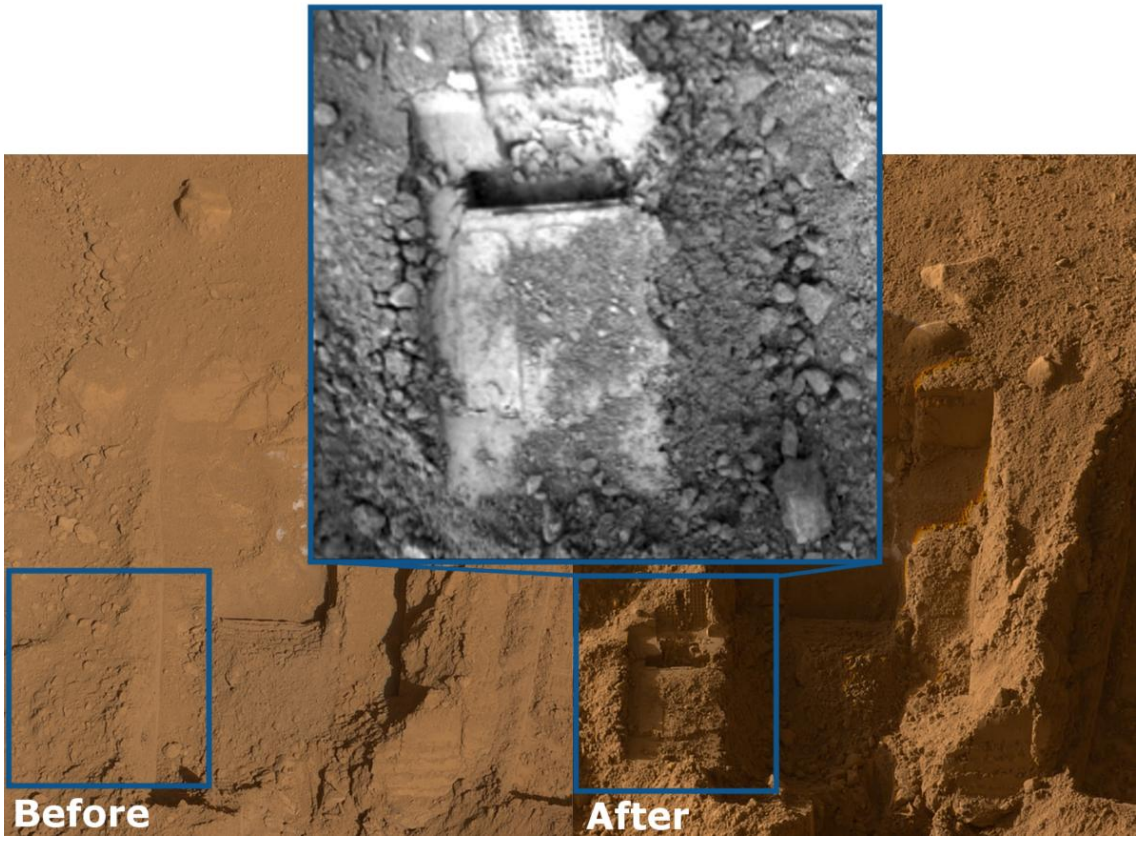

Figure 2.16. DodoGoldilocks wall stress test. Shown at left is the DodoGoldilocks trench before its western wall was stressed by pushing the bottom of the scoop into the soil. At right is an image taken after. At center is a close-up of the affected section of the wall. The imprint of the scraper blade and of the load plate around the rasp can also be seen. Also note the cracks in the upper left of the close-up image. SSI images SS116IOF906529195_1D720RCBA1TB and SS116IOF906500372_1D650RCBA1TB. RAC image RS116RAL906506990_1D77EMBM1.

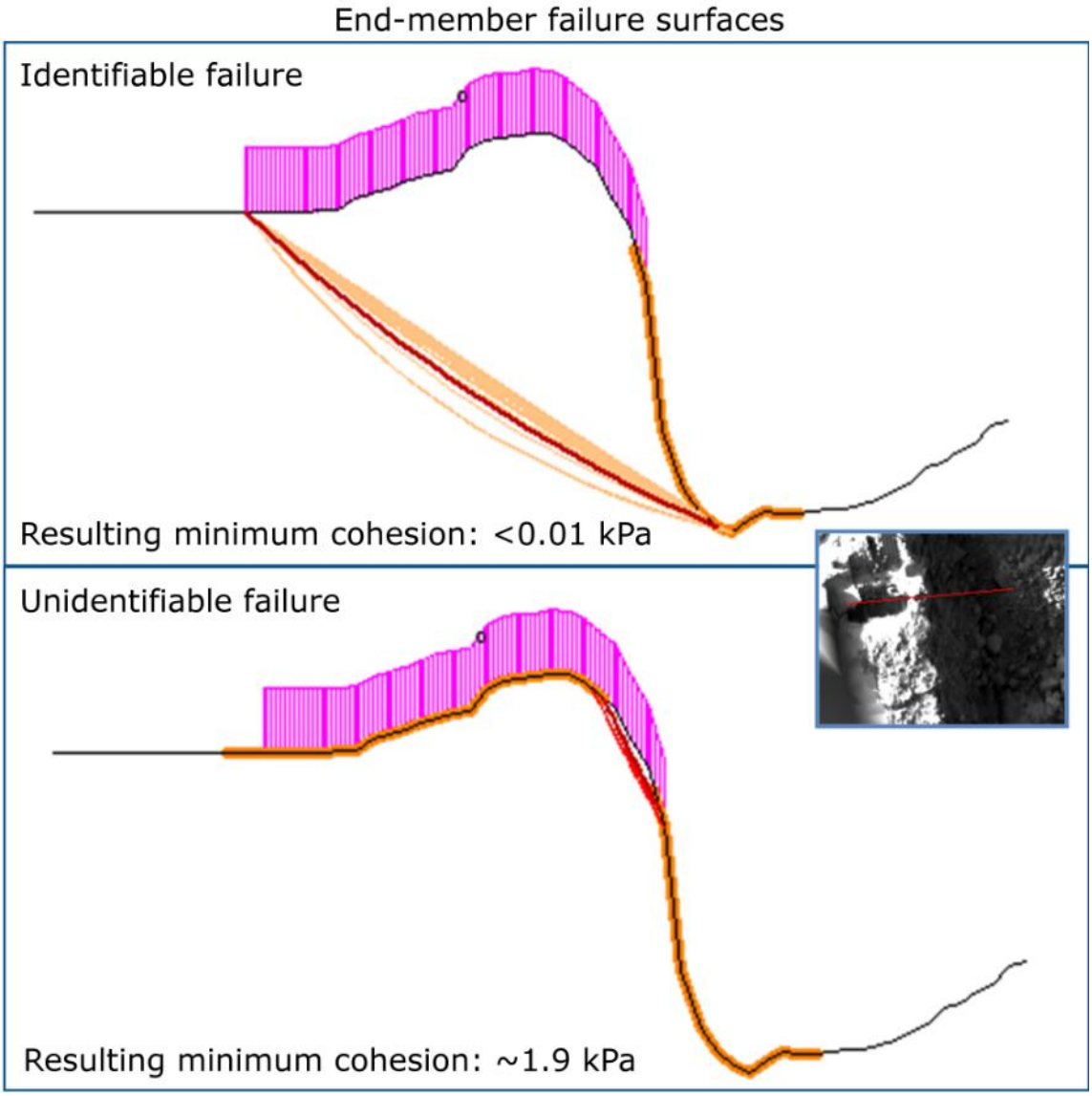

Figure 2.17. Cross-sections of possible failure surfaces overlain over a profile across the western wall of DodoGoldilocks trench (before the wall was stressed). Dark red failure surfaces are critical. Several other failure surfaces with higher Factors of Safety are also shown. Vertical pink lines represent the vertical stress from the scoop. Orange lines indicate the extent to which boundary points for the failure surface were allowed to vary. Inset shows the transect across the imprint from the bottom of the scoop. In the top

profile, the failure surface is one that we might intuitively expect, as it goes through a discontinuity in stress and through the toe of the slope. The failure surface in the bottom profile is one that would not be morphologically identifiable (due to considerations of noise and sampling) in the digital elevation maps (DEMs) from which the profile is obtained. Note that the flat-line to the left of the profiles is imposed because the lander deck obstructed retrieval of a DEM for this portion. SSI image SS116RAL906529012_1D726L1M1.

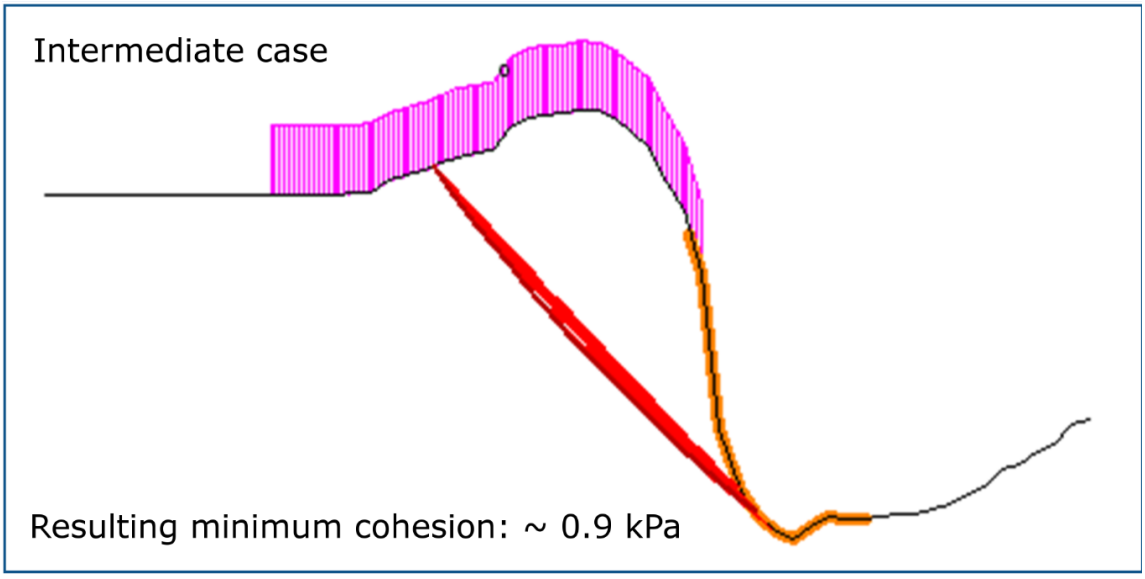

Figure 2.18. An intermediate failure surface for DodoGoldilocks trench. This figure is similar in nature to Figure 2.17, except it shows an intermediate failure surface along with those of higher Factor of Safety.

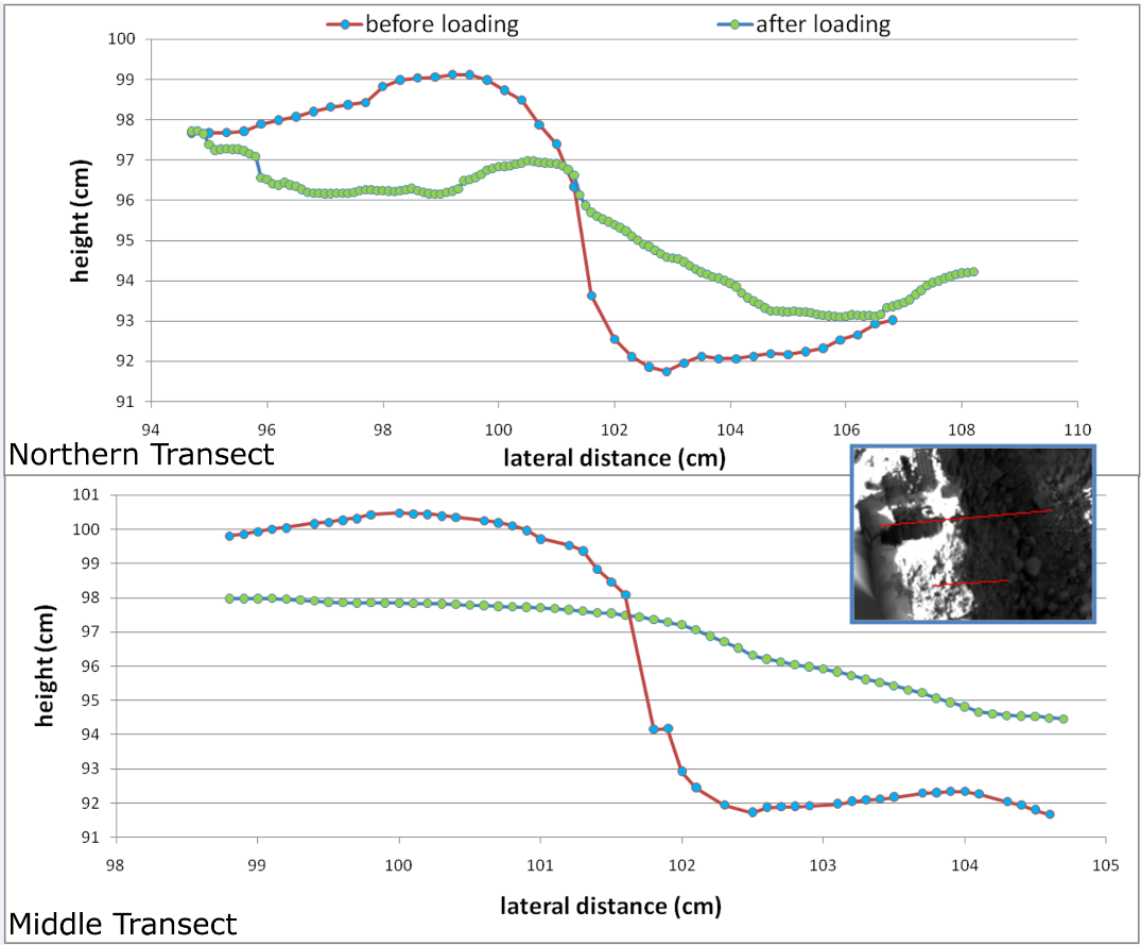

Figure 2.19. Topography profiles that show the effect of stressing a trench wall. Post-stress topography profiles have been superposed on pre-stress profiles for two transects (shown in inset). Note that the dip in the left section of the post-stress profile for the northern transect is due to the effect of the scraper blade. Figure axes have an arbitrary origin. SSI image SS116RAL906529012_1D726L1M1.

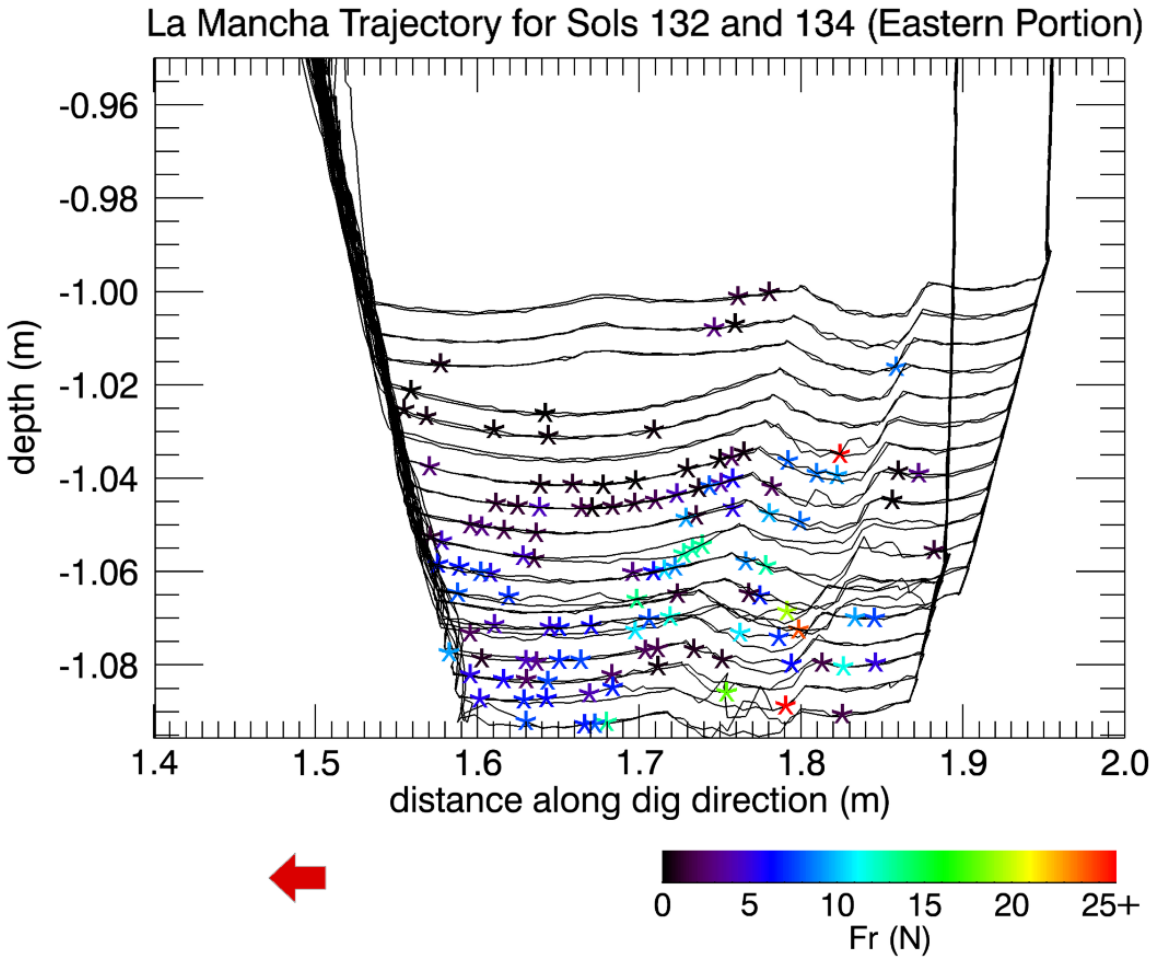

Figure 2.20. Trajectory color-coded by horizontal, radial force for the easternmost swaths in La Mancha trench from sols 132 and 134. Red arrow gives direction of lander.

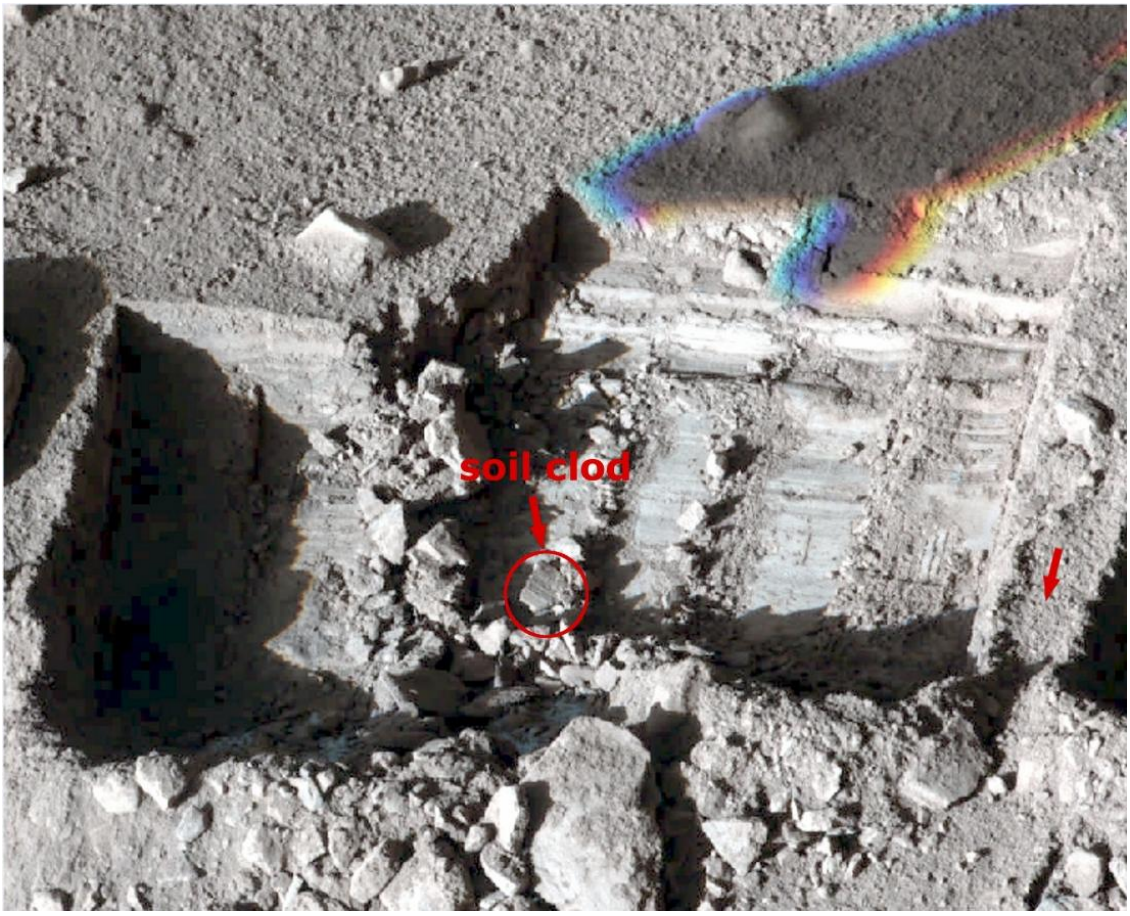

Figure 2.21. False-color image of La Mancha trench, from which platy soil clods were excavated. Partially excavated plate is circled. Red arrow on the right indicates direction of lander. SSI image SS148IOF909363226_20560RCBA1TB.

Figure 2.22. Bee Tree dump pile with material from La Mancha trench. Arrows indicate where plates can be seen in cross-section. Platy structure is evident in several other slabs as well. SSI image SS134IOF908124442_1F3C0R2CBA18TB.

Tables

Mission	c (kPa)	φ(°)
Viking (drift)	0-3.7; avg: 1.6±1.2	avg: 18±2.4
Viking (blocky)	2.2-10.6; avg: 5.1±2.7	avg: 30.8±2.4
Viking (crusty to cloddy)	0-3.2; avg: 1.1±0.8	avg: 34.5±4.7
Pathfinder	0.12-0.356; avg: 0.238	31-41; avg: ~36.6
MER A	5.2	30-37; avg: 33.5
MER B	4.7-5.6; avg: 5.13	30-37; avg: 33.5

Table 2.1. Cohesion (c) and angle of internal friction (φ) found for various landed missions. Note that while the ranges given here are those typical of soils at each site, there were outliers that are not considered in this table. For more information, see: *Moore and Jakosky* [1989], *The Rover Team* [1997], and *Sullivan et al.* [2007].

dump pile	slope(°)	transect #
Croquet Ground sol 108 north pile	36.4	1
Croquet Ground sol 108 middle pile	29.8	2
Bee Tree* sol 129 #1	36.8	3
Bee Tree* sol 129 #2	40.0	4
Caterpillar sol 149	47.6	5
Caterpillar sol 117	38.8	6

*Bee Tree was measured before the platy slabs were dumped on it.

Table 2.2. Dump pile slopes (see Figure 2.1 for dump pile locations in the workspace and Figures 2.6 and 2.7 for accompanying transects and profiles). These values allow for estimation of the angle of internal friction.

trench wall	slope(°)	shadowed?	transect #
Snow White sol 108 north wall	65.6	no	7
Snow White sol 108 south wall	61.7	yes	7
La Mancha sol 148 left wall	66.7	yes	8
La Mancha sol 148 right wall	71.6	no	9
Upper Cupboard sol 147 left wall	58.3	yes	10
Upper Cupboard sol 147 right wall	79.4	no	10
DodoGoldilocks sol 149 right wall	57.1	no	N/A
DodoGoldilocks sol 116 left wall	83.4	no	N/A

Table 2.3. Trench wall slopes (see Figure 2.1 for trench locations in the workspace;

Figure 2.8 shows accompanying transects and profiles for a sampling of the trenches).

excavation	SW22d1soil	SW22d2soil	ISd1 (soil portion)	UC67soil	UC67ice-affected soil
Fr (horizontal force; N)	8.96	12.07	12.11	3.22	9.58
z (depth between passes; m)	0.0030	0.0020	0.0060	0.0029	0.0029
th (blade angle; °)	147.25	149.44	151.00	161.57	141.95
resulting cohesion (kPa)	*0.6*	*1.2*	*0.4*	*0.2*	*0.6*
F1 (N)	0.86	1.13	1.18	0.32	0.95
F2 (N)	0.41	0.79	0.27	0.12	0.48
F4 (N)	7.69	10.15	10.67	2.78	8.14
2sigma uncertainty in Fr (N)	10.66	16.17	16.59	4.69	17.15
error estimate for c (kPa)	+0.8, -0.6	+1.8,-1.2	+0.7, -0.4	+0.4,-0.2	+1.2,-0.6

excavation	LM132d2east	SS74	SS76	SS85	SS88
Fr (horizontal force; N)	4.78	3.89	3.39	4.60	5.12
z (depth between passes; m)	0.0050	0.0029	0.0029	0.0029	0.0029
th (blade angle; °)	162.18	146.10	146.10	143.81	139.80
resulting cohesion (kPa)	*0.2*	*0.3*	*0.2*	*0.3*	*0.3*
F1 (N)	0.48	0.38	0.33	0.45	0.52
F2 (N)	0.11	0.19	0.16	0.23	0.27
F4 (N)	4.19	3.33	2.90	3.92	4.34
2sigma uncertainty in Fr (N)	10.28	6.79	6.45	5.69	9.05
error estimate for c (kPa)	+0.5,-0.2	+0.5,-0.3	+0.5,-0.2	0.5,-0.3	+0.7,-0.3

Table 2.4. Average cohesions from various trenches. Parameters used to calculate cohesion are also listed. The above use 1235 kg/m^3 density, 8.6 cm blade width, 3.76 m/s^2 gravity. Note that the error given corresponds to the average cohesion and there are gradients within the populations. SW= Snow White. IS = Icy Soil PIT (Payload Interoperability Testbed) Test. UC = Upper Cupboard. LM= La Mancha. SS = Stone

Soup. Numbers after each of these abbreviations stand for the sol of the activity. d1=dig1. d2=dig2. See the text for descriptions of parts F1, F2, and F4 of the force. Part 3 is not used because the passes were not deep enough for side-wall cutting action to be a factor.

depth level	scoop velocity (cm/s)	del v (cm/s)
1	3.48	
2	3.43	-0.05
3	3.35	-0.08
4	3.35	0.00
5	**2.91**	**-0.44**
6	**2.27**	**-0.64**
7	**1.65**	**-0.63**
8	1.61	-0.04
9	1.53	-0.08
10	1.42	-0.10

Table 2.5. Scoop velocity during excavation of Snow White trench. Each depth level corresponds to a lower pass than the previous one (by ~0.3 cm). This information is for the first of two sol 22 excavations conducted in Snow White. The rows in bold represent large amounts of velocity change. This occurs roughly 1.5-2 cm below the surface.

References

Arvidson, R. E., R. G. Bonitz, M. L. Robinson, J. L. Carsten, R. A. Volpe, A. Trebi-Ollennu, M. T. Mellon, P. C. Chu, K. R. Davis, J. J. Wilson, A. S. Shaw, R. N. Greenberger, K. L. Siebach, T. C. Stein, S. C. Cull, W. Goetz, R. V. Morris, D. W. Ming, H. U. Keller, M. T. Lemmon, H. G. Sizemore, M. Mehta (2009), Results from the Mars Phoenix Lander Robotic Arm Experiment, *J. Geophys. Res.*, *114*, E00E02, doi:10.1029/2009JE003408.

Balovnev, V. I. (1983), *New methods for calculating resistance to cutting of soil*, Amerind Publishing (Translation), P. Datta translator and Rosvuzizdat, New Delhi, Available from National Technical Information Service, Springfield, VA 22161.

Bishop, A. W. (1955), The use of the slip circle in the stability analysis of earth slopes, *Geotechnique, 5*, 7-17.

Blaney, D. L., D. Archer, R. E. Arvidson, S. Cull, M. Ellehoj, D. Fisher, M. Hecht, M. T. Lemmon, M. T. Mellon, R.V. Morris, T. Pike, P. Smith, C. Stoker, Phoenix Science Team (2009), Multi-Spectral Imaging of the Phoenix Landing Site: Characteristics of Surface and Subsurface Ice, Rocks, and Soils, LPS XL Abstract # 2047.

Blouin, S., A. Hemami, M. Lipsett (2001), Review of resistive force models for earthmoving processes, *J. Aerospace Eng., 14*(3), 102-11.

Boynton, W. V., W. C. Feldman, S. W. Squyres, T. H. Prettyman, J. Bruckner, L. G. Evans, R. C. Reedy, R. Starr, J. R. Arnold, D. M. Drake, P. A. J. Englert, A. E. Metzger, I. Mitrofanov, J. I. Trombka, C. d'Uston, H. Wanke, O. Gasnault, D. K. Hamara, D. M. Janes, R. L. Marcialis, S. Maurice, I. Mikheeva, G. J. Taylor, R. Tokar, C. Shinohara (2002), Distribution of hydrogen in the near surface of Mars: Evidence for subsurface ice deposits, *Science, 297*, 81–85, doi:10.1126/science.1073722.

Boynton, W. V., D. W. Ming, S. P. Kounaves, S. M. M. Young, R. E. Arvidson, M. H. Hecht, J. Hoffman, P. B. Niles, D. K. Hamara, R. C. Quinn, P. H. Smith, B. Sutter, D. C. Catling, R. V. Morris (2009), Evidence for Calcium Carbonate at the Mars Phoenix Landing Site, *Science, 325*, 61, doi: 10.1126/science.1172768.

Bonitz, R. G., L. Shiraishi, M. Robinson, R. E. Arvidson, P. C. Chu, J. J. Wilson, K. R. Davis, G. Paulsen, A. G. Kusack, D. Archer, P. Smith (2008), NASA Mars 2007 Phoenix Lander Robotic Arm and Icy Soil Acquisition Device, *J. Geophys. Res., 113*, E00A01, doi: 10.1029/2007JE003030.

Clover Technology (2006), GALENA Slope Stability Analysis System Users' Guide Version 5.0, Clover Associates Pty Limited, Robertson NSW 2577 Australia.

Cull, S., R. E. Arvidson, D. Blaney, R. V. Morris (2008), Spectral Modeling of Ground Ices Exposed by Trenching at the Phoenix Mars Landing Site, *Eos. Trans. AGU, 89*(53), Fall Meet. Suppl., Abstract U11B-0027.

Cull, S. C., R.E. Arvidson, M.T. Mellon, S.Wiseman, R.Clark, T. Titus, R.V. Morris, P. McGuire (2010), Seasonal H2O and CO2 Ices at the Mars Phoenix Landing Site:

I. Results from Pre-Landing CRISM and HiRISE Observations, *J. Geophys. Res*., *115*, E00D16, doi:10.1029/2009JE003340.

Hecht, M. H., S. P. Kounaves, R. C. Quinn, S. J. West, S. M. M. Young, D. W. Ming, D. C. Catling, B. C. Clark, W. V. Boynton, J. Hoffman, L. P. DeFlores, K. Gospodinova, J. Kapit, P. H. Smith (2009), Detection of Perchlorate and the Soluble Chemistry of Martian Soil at the Phoenix Lander Site, *Science, 325*, 64, doi: 10.1126/science.1172466.

Heet, T. L., R. E. Arvidson, S. C. Cull, M. T. Mellon, K. D. Seelos (2009), Geologic Setting of the Phoenix Lander Mission Landing Site, *J. Geophys. Res.*, *114*, E00E04, doi:10.1029/2009JE003416.

Jones, T. A. (2006), MATLAB functions to analyze directional (azimuthal) data – I: Single-sample inference, *Computers and Geosciences, 32*, 166-175.

Keller, H. U., W. Goetz, H. Hartwig, S. F. Hviid, R. Kramm, W. J. Markiewicz, R. Reynolds, C. Shinohara, P. Smith, R. Tanner, P. Woida, R. Woida, B. J. Bos, M. T. Lemmon (2008), Phoenix Robotic Arm Camera, *J. Geophys. Res., 113*, E00A17, doi: 10.1029/2007JE003044.

Kounaves, S. P., M. H. Hecht, J. Kapit, K. Gospodinova, L. DeFlores, R. C. Quinn, W. V. Boynton, B. C. Clark, D. C. Catling, P. Hredzak, D. W. Ming, Q. Moore, J. Shusterman, S. Stroble, S. J. West, S. M. M. Young (2010), The Wet Chemistry Experiments on the 2007 Phoenix Mars Scout Lander Mission: Data Analysis and Results, *J. Geophys. Res*., *115*, E00E10, doi:10.1029/2009JE003424.

Lemmon, M. T., R. E. Arvidson, D. Blaney, E. Dejong, M. B. Madsen, M. Malin, M. T. Mellon, R. Morris, W. T. Pike, P. H. Smith, C. Stoker, P. S. Team (2008), Phoenix landing site and sample context images from the Surface Stereo Imager, *Eos Trans. AGU, 89*(53), Fall Meet. Suppl., abstract U14A-02.

Mellon, M. T., W. V. Boynton, W. C. Feldman, R. E. Arvidson, T. N. Titus, J. L. Bandfield, N. E. Putzig, H. G. Sizemore (2008), A prelanding assessment of the ice table depth and ground ice characteristics in Martian permafrost at the Phoenix landing site, *J. Geophys. Res.,113*, E00A25, doi:10.1029/2007JE003067.

Mellon, M. T., M. C. Malin, R. E. Arvidson, M. L. Searls, H. G. Sizemore, T. L. Heet, M. T. Lemmon, H. U. Keller, J. Marshall (2009), The Periglacial Landscape at the Phoenix Landing Site, *J. Geophys. Res., 114*, E00E06, doi:10.1029/2009JE003418.

Moore, H. J., R. E. Hutton, G. D. Clow, C. R. Spitzer(1987), *Physical Properties of the Surface Materials at the Viking Landing Sites on Mars*, U. S. Geological Survey Professional Paper 1389, United States Government Printing Office, Washington.

Moore, H. J., and B. M. Jakosky (1989), Viking Landing Sites, Remote-Sensing Observations, and Physical Properties of Martian Surface Materials, *Icarus, 81*, 164-184.

Mutch, T. A., R. E. Arvidson, A. B. Binder, E. A. Guinness, E. C. Morris (1977), The Geology of the Viking Lander 2 Site, *J. Geophys. Res., 82*, 4452-4467.

Poulet, F., Y. Langevin, J.-P. Bibring, R. E. Arvidson, G. Boubin, B. Gondet(2009), Mineralogy of the high latitudes of Mars including the Phoenix landing site, LPS XL Abstract # 1551.

The Rover Team (1997), Characterization of the Martian Surface Deposits by the Mars Pathfinder rover, Sojourner, *Science, 278*, 1765-1768.

Scholtes L., B. Chareyre, F. Nicot, F. Darve (2009), Micromechanics of granular materials with capillary effects, *International Journal of Engineering Science, 47*, 72.

Sizemore, H. G., M. T. Mellon, M. L. Searls, M. T. Lemmon, A. P. Zent, T. L. Heet, R. E. Arvidson, D. L. Blaney, H. U. Keller (2010), In Situ Analysis of Ice Table Depth Variations in the Vicinity of Small Rocks at the Phoenix Landing Site, *J. Geophys. Res*., *115*, E00E09, doi:10.1029/2009JE003414

.

Smith, P. H., L. Tamppari, R. E. Arvidson, D. Bass, D. Blaney, W. Boynton, A. Carswell, D. Catling, B. C. Clark, T. Duck, E. DeJong, D. Fisher, W. Goetz, P. Gunnlaugsson, M. Hecht, V. Hipkin, J, Hoffman, S. F**.** Hviid, H. U**.** Keller, S. Kounaves, C. Lange, M. Lemmon, M. B**.** Madsen, M. Malin, W. Markiewicz, J. Marshall, C. McKay, M. Mellon, D. Michelangeli, D. Ming, R. V. Morris, W. T. Pike, N. Renno, U. Staufer, C. Stoker, P. Taylor, J. Whiteway, S. Young, A. Zent (2008), Introduction to special section on the Phoenix Mission: Landing Site Characterization Experiments, Mission Overviews, and Expected Science, *J. Geophys. Res., 113*, E00A18, doi: 10.1029/2008JE003083.

Smith, P. H., L. Tamppari, R. E. Arvidson, D. Bass, D. Blaney, W. Boynton, A. Carswell, D. Catling, B. C. Clark, T. Duck, E. DeJong, D. Fisher, W. Goetz, P.

Gunnlaugsson, M. Hecht, V. Hipkin, J, Hoffman, S. F. Hviid, H. U. Keller, S. Kounaves, C. Lange, M. Lemmon, M. B. Madsen, W. Markiewicz, J. Marshall, C. McKay, M. Mellon, D. Ming, R. V. Morris, W. T. Pike, N. Renno, U. Staufer, C. Stoker, P. Taylor, J. Whiteway, A. Zent (2009), H2O at the Phoenix Landing Site, *Science, 325*, 58, doi: 10.1126/science.1172339.

Spencer, E. (1968), Effect of Tension on Stability of Embankments, *ASCE, J. Soil Mech Found Div, 94*, SM5, 1159-1173.

Spong, M. W. and M. Vidyasagar (1989), *Robot Dynamics and Control*, John Wiley & Sons, New York.

Sullivan, R., R. Anderson, J. Biesiadecki, T. Bond, H. Stewart (2007), Martian regolith cohesions and angles of internal friction from analysis of MER wheel trenches, LPS XXXVIII Abstract # 2084.

Van Vliet-Lanoe, B., J. Coutard, and A. Pissart (1984), Structures caused by repeated freezing and thawing in various loamy sediments: a comparison of active, fossil, and experimental data, *Earth Surface Processes and Landforms, 9*, 553-565.

Wilkinson, A., and A. DeGennaro (2007), Digging and pushing lunar regolith: Classical soil mechanics and the forces needed for excavation and traction, *Journal of Terramechanics, 44*, 133-152.

Zamani, P., D. Alexander, R. Deen(2008), Phoenix Software Interface Specification, Natl. Aeronaut. and Space Admin.,Washington, D. C. (Available at http://an.rsl.wustl.edu/phx/solbrowser/browserFr.aspx?tab=res).

Zent, A. P., M. H. Hecht, D. R. Cobos, S. E. Wood, T. L. Hudson, S. M. Milkovich, L. P. DeFlores, M. T. Mellon (2010), Initial Results from the Thermal and Electrical Conductivity Probe (TECP) on Phoenix, *J. Geophys Res*., *115*, E00E14, doi:10.1029/2009JE003420 .

Chapter 3 : Derivation of Surface Scattering Properties

3.1 Introduction

The focus of this chapter is the use of CRISM spectrophotometric data coupled with surface observations from the Opportunity rover in order to derive surface scattering properties for Victoria crater's ejecta apron and its surroundings. This region was chosen because it has the highest quality spectrophotometric coverage, and this coverage was acquired because this region has a variety of geologic features and diverse terrain. In Section 3.2, the CRISM dataset is described in detail and its suitability for analysis of scattering properties is discussed. In Section 3.3, an in-depth treatment of the modeling process is provided. The material is divided into three parts: (1) the surface model that is used in this work is introduced, (2) the atmospheric model is outlined, and (3) the simultaneous implementation of both models is addressed. Interpretation of the scattering properties in terms of surface characteristics is reserved for Chapter 4.

3.2 Description of Primary Dataset

CRISM measures the radiance of the surface of Mars as seen through its atmosphere (see Section 3.3.2 for a discussion of atmospheric correction). CRISM [*Murchie et al*., 2006] has several types of observation modes; the most useful for surface photometry is the FRT or Full Resolution Targeted mode, which has the maximum phase angle coverage (the phase angle is the angle between the incident and scattered rays of light). A schematic of the acquisition of CRISM FRTs is shown in Figure 3.1 [*Murchie et al*., 2006]. CRISM collects data as it flies from south to north, the gray arrows in the figure show this flight path. While collecting data, CRISM gimbals, which means that it

alters its viewing angle to track a target patch of ground as it flies over, allowing the measurement of light that the target has scattered to different directions and therefore the determination of how the scattering of light varies with phase angle.

There are 11 images associated with an FRT[1]; five of which (labeled 01 to 05 in CRISM product files) are acquired at discrete viewing geometries as MRO flies toward a target (purple lines of sight in Figure 3.1), one of which (labeled 07) is acquired as a near-nadir scan with continuously varying viewing geometry (for which several lines of sight are shown in green in Figure 3.1), and the last five images (labeled 09 to 0D) are acquired at discrete viewing geometries as MRO flies away from the target (red lines of slight in Figure 3.1). Geometry products are available for each of the 11 images; these products give incidence, emergence, and phase angles[2] for every pixel (this information is derived from several SPICE kernels). For the emergence angle coverage of each image in FRT0000B6B5, see Table 3.1. The images in an FRT vary in spatial resolution because they are taken at varying distances from the target. The central scan has the highest spatial resolution at ~15-20 meters per pixel (see Table 3.2 for information specific to FRT0000B6B5). The first and last images of the sequence have the largest

[1] FRTs taken after September of 2010 contain only six associated images due to a change in gimbal performance, this means that FRTs taken after this date have less phase angle coverage.

[2] The incidence angle is the angle incident light makes with the surface normal. The emergence angle is the angle emergent light makes with the surface normal. The phase angle is the angle between the incident and emergent rays of light.

pixel sizes, at about 350-400 meters per pixel. For ease of analysis (i.e. to enable phase function extraction via ENVI ENvironment for Visualizing Images and the IDL Interactive Data Language programming environment and to result in quicker computation times), all images were resampled to seven times the resolution of the central scan.

All 11 images in an FRT are hyperspectral in nature, which means they use all of CRISM's available channels (536 bands from 0.365 to 3.937 micrometers, split across two detectors called 'S' for short-wavelength and 'L' for long-wavelength). The images result from the readout of detectors which are 640 columns wide in the cross-track direction, and each element in a column corresponds to a separate band (channel) in wavelength-space. The detectors are swept along-track to achieve the second spatial dimension of each image.

For this work, a subset of six spectral bands was used: 0.566 μm, 0.801 μm, 0.951 μm, 1.277 μm, 1.513 μm, and 2.271 μm. These bands are well spaced to cover much of CRISM's spectral range and are outside of atmospheric gas (CO_2, CO, H_2O) absorption bands. This selection of bands reduces computation time and potential sources of error. Note that atmospheric modeling is still performed in order to account for light scattering from and absorption by aerosols (especially important for wavelengths shorter than 0.7 μm, where aerosol iron mineralogy has a significant effect). Also note that the wavelengths used are in a region of the spectrum in which solar radiation is the dominant factor affecting the signal (i.e. surface blackbody radiation thermal effects do not become an issue until wavelengths greater than 3 μm).

Numerous FRT observations have been acquired around Opportunity's traverse area; Figure 3.2 shows the footprints (i.e. areal coverage) of these observations in white and red, as well as the rover traverse in black (courtesy of the rover localization and mapping work of Ron Li and the OSU Mapping and GIS Laboratory). The FRT used in this work was FRT0000B6B5 (Figure 3.3; Table 3.2) because a substantial surface area was covered by all 11 images in the observation (i.e. the most phase angle information for the largest region) and it was taken during a period of low atmospheric opacity (see Section 3.3.2). When this image was acquired, sunlight was incident from an azimuth of 212.167 degrees clockwise from the east (so approximately from the northwest). For this analysis, the input data is the CRISM standard I/F product (TRR3 version, which is the latest at the time of writing, and includes improved noise correction compared to the older version: TRR2). The quantity contained in the CRISM I/F product is actually the radiance factor (rf), which is similar to I/F in that I/F is radiance at sensor (I) normalized by the incoming solar irradiance (F), whereas rf is I normalized by the radiance ($I_L = F/\pi$) that would be observed if the same incoming solar irradiance was normally incident on and scattered by a Lambertian surface. Therefore, CRISM I/F = rf = $I/(F/\pi)$.

3.3 Modeling Atmospheric and Surface Radiance Contributions

3.3.1 The Surface Model

To model light scattering from the surface, a simplified version of the Hapke model (Equations 3.1-3.3; [*Hapke*, 1993]) was used in order to minimize the number of parameters being fitted, so well-constrained fits are obtained over most of the study area, as will be further discussed in Section 4.3.

$$rf = \left(\frac{w}{4}\right)\left(\frac{\mu_0}{\mu_0 + \mu}\right)\left[p(g) + H(\mu_0)H(\mu) - 1\right] \tag{3.1}$$

$$p(g) = \frac{1 - b^2}{\left[1 + b^2 + 2b\cos(g)\right]^{3/2}} \tag{3.2}$$

$$H(\mu) \sim \frac{1 + 2\mu}{1 + 2\sqrt{1 - w}\mu} \tag{3.3}$$

where *rf* is radiance factor, *p(g)* is the average one-term Henyey-Greenstein single particle phase function (note that although *p(g)* is intended to describe scattering from a single particle, it will be used here as a more general parameterization of the surface, including surface roughness, see Chapter 4 for more details), *g* is the phase angle, *w* is the average single particle scattering albedo (an indicator of surface reflectivity, this parameter is the ratio of the scattering efficiency to the sum of the scattering and absorption efficiencies and therefore ranges from 0 to 1), *H* is the multiple scattering function, μ_0 is the cosine of the incidence angle, μ is the cosine of the emergence angle, and *b* is the asymmetry parameter. *b* varies from -1 to 1 and describes how asymmetrically the surface is scattering the incoming light; negative values indicate a backward-scattering surface and positive values indicate a forward-scattering surface. Note that this convention is very different from the one used for the asymmetry parameter for the two-term Henyey-Greenstein phase function, where *b* describes the directivity, or width, of the scattering lobes and ranges from 0 to 1 in value. Also note that it is not possible to constrain the two-term Henyey-Greenstein phase function with only 11 viewing geometries ranging from about 40° to slightly over 100° in phase angle.

The version of the Hapke model used here is basically a radiative transfer model for particulate surfaces that includes the effects of multiple scattering (through the H-function shown in Equation 3.3), and it is used in conjunction with the one-term Henyey-Greenstein phase function. Inputs at each iteration include the radiance at the surface and the illumination and viewing geometry, and the parameters being fit for are *w* (which is independent of illumination and viewing geometry) and *b* (describes the degree to which the phase function is anisotropic) for each 11-frame deep pixel (i.e. for 11 different combinations of emergence angle, phase angle, and I/F). Note that the simplified version of the Hapke model used here does not have surface roughness as a separate parameter; therefore the effects of surface roughness are included in and end up dominating the expression of *b*, allowing the generation of maps of surface roughness (this interpretation is backed by comparisons to studies using near-surface data, as will be discussed in Chapter 4). In contrast to other versions of the Hapke Model, no constraints are imposed on the symmetry of the roughness elements. Also note that in Equation 3.1, the opposition effect is not modeled since this effect is only important at smaller phase angles, and the phase coverage of FRT0000B6B5 does not extend below 39° (see Table 3.2).

3.3.2 The Atmospheric Model

To model the atmosphere, Discrete Ordinate Radiative Transfer (DISORT; [*Stamnes et al.*, 1988]) is used. DISORT is a model of the transfer of radiation from one location to another by scattering, emission, and absorption in an atmosphere with plane-parallel layers (15 computational layers are used) and a lower bound specified by the

surface model described above; the discrete ordinates refer to the discrete polar angles at which the radiative transfer is evaluated. Along with DISORT, a Mars-specific interface is used. This interface, called DISORT_multi, was developed by *Wolff et al*. [2009], and modified, for the purposes of this work, to include a one-term Henyey-Greenstein surface phase function (Equation 3.2). As with any model, several input parameters are required, and for some of these, the results of previous workers are used. For example, an atmospheric dust particle radius of 1.5 μm (constant with height above the ground) is used, along with a constant vertical dust mixing ratio and wavelength-dependent dust particle phase function (64-term Legendre expansion) and albedo [*Wolff et al*., 2009]. The value for dust particle radius mentioned above is quite close to the value obtained by *Lemmon et al.* [2004]: 1.52 ± 0.18 μm using observations of the atmosphere made using the Panoramic Cameras on the Opportunity rover to look at the sky (i.e. no surface contribution to separate out). Note that there are slight offsets between the wavelengths for which *Wolff et al.* [2009] have derived atmospheric dust scattering parameters and the wavelengths used in this work to derive surface scattering parameters; both sets of wavelengths are shown in Table 3.3. Dust is assumed to be present from 0 to 150 kilometers height in the martian atmosphere. Further inputs to the atmospheric model include surface pressure based on fits to Viking Lander pressure data (differences in elevation are also taken into account assuming an atmosphere in hydrostatic equilibrium) [*Tillman et al*., 1993] and temperature profiles (with a surface temperature of 260.6 Kelvin and atmospheric temperatures ranging from 205.6 Kelvin just above the surface to 134.1 Kelvin at 55.2 kilometers height at the time FRT0000B6B5 was taken) as well as

atmospheric water vapor column abundance (9.1 precipitable micrometers when FRT0000B6B5 was taken) from TES (Thermal Emission Spectrometer, which was on Mars Global Surveyor) climatological data [*Smith*, 2002] for the appropriate latitude, longitude, and solar longitude L_s (i.e. time of year; see Table 3.2) from Mars Year 26 (corresponding to April 2002 – March 2004) which is taken to be a representative year (spacecraft observations have shown that martian atmospheric patterns tend to repeat from year to year [*Smith*, 2008]). The value for the atmospheric optical depth due to dust was taken from *Wolff et al*. [2009], who derived optical depth for each CRISM Emission Phase Function (EPF) and FRT observation, including FRT0000B6B5 (for this FRT, nadir-looking dust optical depth was 0.43 ± 0.04 at 0.9 micrometers) this is consistent with the optical depth value obtained via the Panoramic Camera (Pancam) on board the Opportunity rover which gave an estimate of 0.449 ± 0.04 at 0.88 micrometers on sol 1584 of rover operations, which corresponds to the date FRT0000B6B5 was taken (PDS Optical Depth Database; see *Lemmon et al*. [2004] for a description of how optical depth values were obtained). The 0.9 μm optical depth was used to obtain the optical depths at the wavelengths of interest (see Section 3.2) through linear extrapolation, taking into account the effective aerosol extinction cross-section as a function of wavelength for martian dust [*Wolff et al.*, 2009]. Computations involve 16 streams, or discrete polar angles. The consistency of our results (both the self-consistency and the consistency with *in situ* and near-surface data sets; discussed in Chapter 4) indicate that the assumptions mentioned above are reasonable.

3.3.3 Implementation

To derive the best-fit surface scattering parameters, modeled CRISM I/F values are compared to the actual CRISM I/F data. To model these data, the surface and atmospheric models (sections 3.3.1 and 3.3.2) are simultaneously implemented in an iterative process that uses the Levenberg-Marquardt least squares approach [*Markwardt*, 2008]. Input seed values for the surface parameters are fed to the combined surface and atmospheric model. DISORT is used to model the radiative transfer of sunlight as it passes through the martian atmosphere, then the resulting radiative output is used as input for the surface model (the Hapke model) which is defined within DISORT and gives the amount of light scattered from the surface, this output is then fed back into the atmospheric radiative transfer model within DISORT since the light interacts with the martian atmosphere again on its way up to the CRISM detector (note that although the surface model is defined within DISORT, it consists of a separate type of radiative transfer model than what DISORT uses for the atmosphere, as described earlier). The result is the modeled I/F at the CRISM detector, which is compared to the CRISM I/F measurement. The surface scattering parameters *w* and *b* are then adjusted and the procedure is repeated until the best fit to the CRISM data is achieved.

Before using this technique on each individual 11-image deep pixel in a phase cube[3], a preliminary investigation is conducted in order to find the general region of the parameter space in which the global minimum in χ^2 is located; this preliminary work will

[3] As opposed to a spectral cube, a phase cube has phase angle as its third dimension instead of wavelength.

allow the determination of appropriate seed values for each parameter to be used for the pixel-by-pixel fits to obtain parameter maps for the study area. This exploratory work is accomplished in an efficient manner by taking the whole study area as input for the combined surface and atmospheric model. In this manner, average best-fit scattering parameter values are obtained for each point on a grid of initial parameter values; this reveals all local minima. Then a grid search is performed to obtain a global minimum in χ^2 space.

After completing the procedure described above, pixel-by-pixel fits are performed, allowing the generation of maps of *w* and *b* that can be used to compare the scattering properties of various surface units. To generate these maps, each pixel (corresponding to 11 values of *e* and *g* since there are 11 images taken at 11 different viewing angles) is now subjected to the model described in sections 3.3.1 and 3.3.2. The seed values obtained as described earlier in this section are used to initialize the fitting procedure. The results are presented in Chapter 4 along with their interpretation.

3.3.4 Error Estimation

In this section, two types of error are discussed: absolute error and relative error. Absolute error does not affect resulting trends other than by shifting all values by the same amount (in scattering parameter space; i.e. all pixels in an image will be affected in the same manner). Relative error, or pixel-to-pixel error, does affect trends.

The principal contributors to absolute error are uncertainties in atmospheric opacity and atmospheric dust particle radius. Absolute error is of the same order as the standard deviation in single scattering albedo and asymmetry parameter over all values

covering the study area at a particular wavelength, a quantity which encompasses terrain variations as well as instrument noise; however, changing the optical depth and the atmospheric dust particle radius (note that average values of these quantities are used for the whole scene) did not appreciably change the resulting patterns of variation for either the single scattering albedo or the asymmetry parameter. This result, taken together with the fact that parameter maps correlate with surface features (as opposed to any less obvious atmospheric features that may be present) indicates that the value of the relative pixel-to-pixel error is much smaller than the absolute error. 0.801 μm is a useful wavelength for identifying surface features, and this band from the high-resolution central scan of FRT0000B6B5 is shown in Figure 3.3 and is depicted in large format in Figure 4.20. In Figure 4.20, surface features such as craters, wind streaks, strips of bedrock-rich terrain, and an ejecta apron are clearly visible. Given the discussion above, comparing values for different units in FRT0000B6B5 is more accurate then comparing them with units imaged in other FRTs that are taken at different times and therefore different atmospheric conditions (for which one would apply the absolute error values that will be discussed later in this section), although both types of comparisons will provide useful information. A quantitative procedure for obtaining relative error will also be discussed later in this section.

To obtain an estimate for the magnitude of the absolute error associated with scattering parameter results, tests of the sensitivity of the results to both the input optical depth and the atmospheric dust particle radius were conducted. Input optical depth values one standard deviation away from the estimated best value were input into the

model and this sensitivity test resulted in a change in the average parameter values over the study area by +0.016, -0.017 in single scattering albedo and +0.020, -0.023 in asymmetry parameter. To test the effect of the atmospheric dust radius being used in the atmospheric correction, this parameter was varied within its error limits and the effect on scattering parameter results was observed. Changing the dust radius from 1.5 μm to 1.7 μm would test the outer bound on the error limit, but dust scattering parameters have not been calculated for 1.7 μm radius dust particles, so 2.0 μm was used as the dust radius in this sensitivity test. Table 3.4 shows the results. Using a larger dust particle radius in the model causes the surface to appear less backscattering and the single scattering albedo to appear higher. Using the results at 1.5 μm and at 2.0 μm to linearly interpolate to 1.7 μm, we obtain an error estimate of ±0.0044 in single scattering albedo and ±0.0076 in asymmetry parameter due to the uncertainty in dust particle radius. Totaling the contributions from both the uncertainty in atmospheric dust particle radius and the uncertainty in atmospheric opacity, absolute error in single scattering albedo is ±0.02, and absolute error in asymmetry parameter is ±0.03.

Also of interest is the relative error, which affects the reliability of pixel-to-pixel comparisons in the retrieved scattering parameter maps. To obtain estimates for relative error, a pixel (which has associated w, b, and χ^2 values) was randomly picked from those that had χ^2 values close to the mean (within a fifth of a standard deviation) and the combined modeling described above was run 50 times for that pixel, but random error in I/F was introduced into all but the first run. The standard deviation of the scattering parameters was then taken to be the error in those parameters. In this process, for all

except the first run, for each of the 11 input values of I/F, error in I/F was either added or subtracted based on a random Boolean generator. The magnitude of the error in I/F was determined by taking the standard deviation in I/F of a relatively homogenous region (Figure 3.4) of the central scan for each wavelength. Error bars showing the magnitude of relative error at each wavelength are included with the scattering parameter spectra presented Chapter 4 (specifically, Figures 4.10 and 4.12).

Other factors that were investigated in order to determine their contributions to error include the computational polar angles used when modeling radiative transfer and the seed parameter values used when searching for the best-fit between model and data. To determine whether running DISORT with 16 computational polar angles was sufficient to model the radiative transfer, or whether more computational rigor (i.e. more computational polar angles) would improve results, DISORT was also run with double the number of computational polar angles, or streams (at 0.801 μm). Table 3.4 shows the results. The differences in parameter statistics are minimal, and therefore it is unnecessary to conduct the much slower 32-stream runs. Table 3.4 also shows a test on the sensitivity to the seed parameter value. It was determined that unless the seed parameter value is at the edge of the parameter space, one can have large differences in seed parameters without much difference in resulting best-fit parameter statistics. If the procedure outlined earlier in this section is followed, seed parameters will be robust enough to yield reliable results. Table 3.4 does indicate that results have more of a dependence on seed parameters than they do on number of computational polar angles. Choice of seed parameters does affect the number of outlier pixels.

Figures

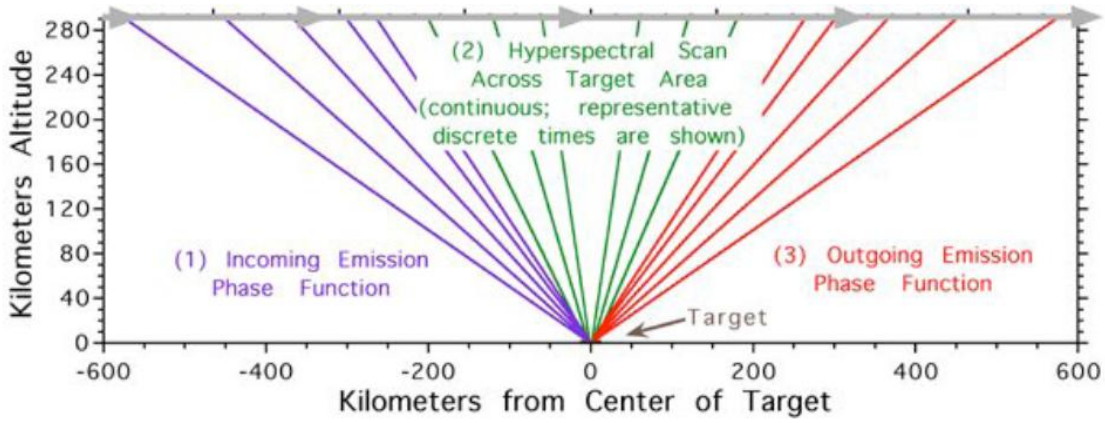

Figure 3.1. Schematic of the acquisition of a CRISM targeted observation. Reproduced from CRISM SIS [*Murchie et al.*, 2006]. The gray arrows represent the spacecraft flight path, and the colored lines represent lines of sight to the surface target. Note that emergence angle (angle between the emergent light and the surface normal), and therefore phase angle, changes throughout the course of the observation.

Figure 3.2. CRISM coverage in the region around the Opportunity traverse. Background is CTX (Context imager on MRO) mosaic with thermal inertia from THEMIS (Thermal Emission Imaging System on ODY). Differences in thermal inertia indicate differences

in surface properties; see Chapter 4 for more details. FRT0000B6B5 central scan footprint (red line) and Opportunity traverses (black line) are overlain.

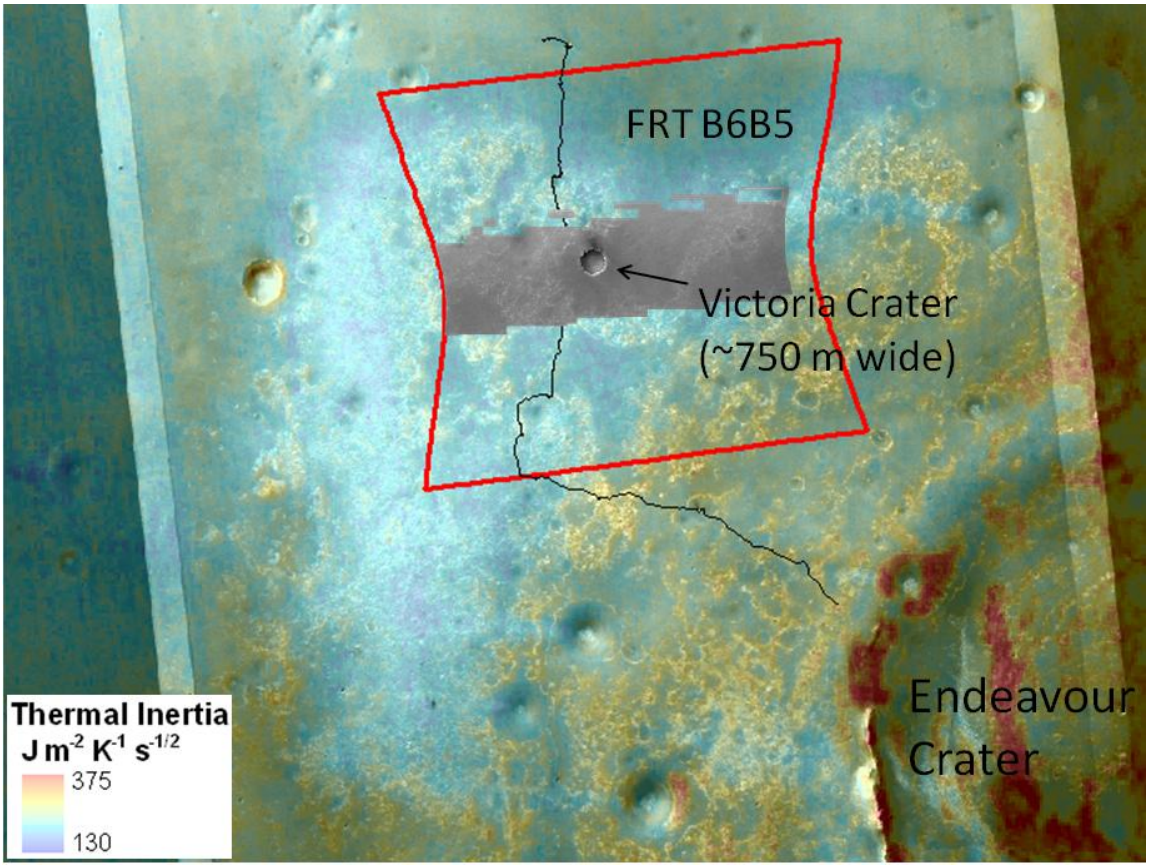

Figure 3.3. Photometric coverage for FRT0000B6B5. Grayscale region shows where all ten off-nadir frames overlap with the central scan.

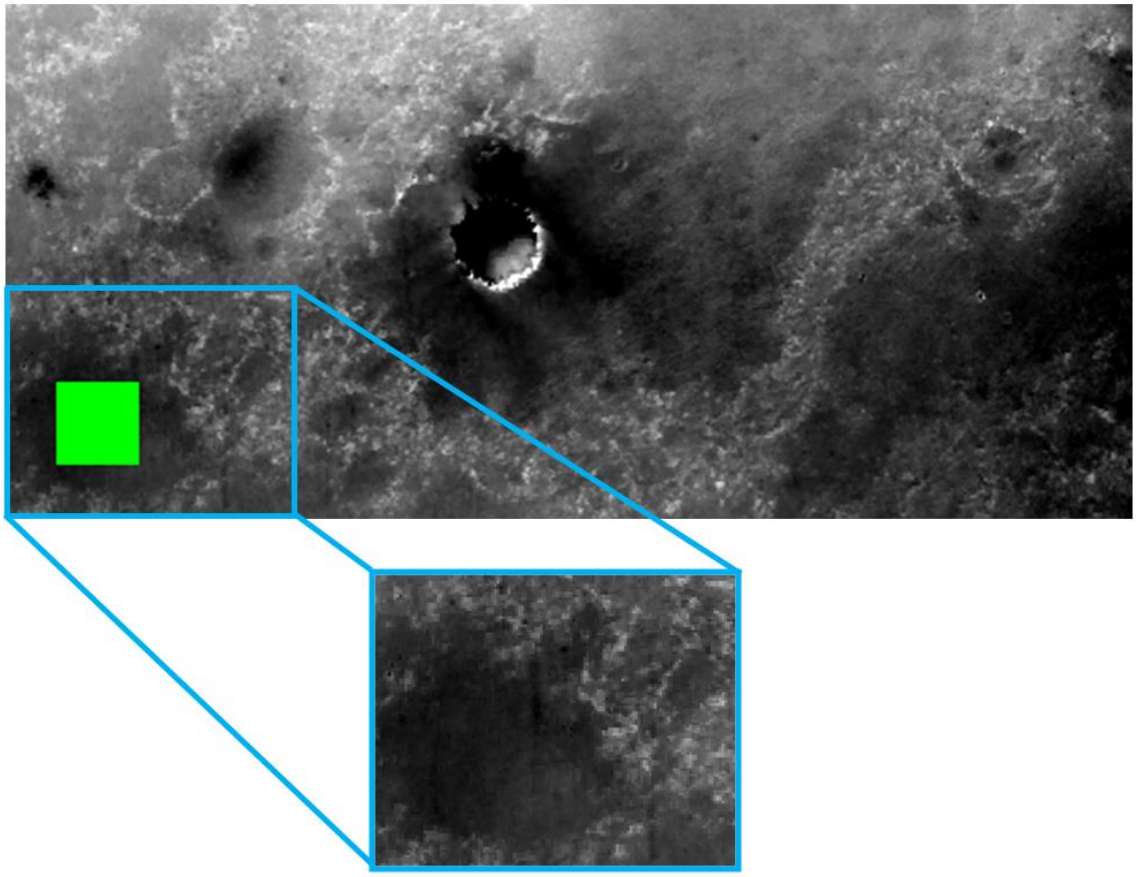

Figure 3.4. Region used to estimate error in I/F. The green region is relatively homogeneous compared to other areas in the scene, and because of this, the standard deviation of the I/F values in this region was used as an estimate of error in I/F.

Tables

FRT Image Segment	Emergence angle coverage (°)
01	68.1-68.5
02	61.4-61.6
03	54.7-55.4
04	58.3-48.8
05	41.9-43.5
07	0.1-21.3
09	44.8-46.1
0A	50.9-51.3
0B	56.6-57.4
0C	~63.1
0D	69.4-69.9

Table 3.1. Emergence angle coverage for each image in FRT0000B6B5.

Parameter	Value for FRT B6B5
L_s (°)	96*
Mars Year	29
Date of acquisition (MM/DD/YY)	07/08/08
DOY	190
Latitude (°N)	-2.05656
Longitude (°W)	5.48452
Local time (hours:min)	15:24
Phase angle coverage (°)	39.18 - 106.48
Resolution of image 01 (m/pixel)	371.4
Resolution of central scan (m/pixel)	17.9
Resolution of image 0D (m/pixel)	391.4

Table 3.2. Observation information for FRT0000B6B5. The given latitude and longitude are for the spatial center of the FRT's high-resolution central scan.

* This solar longitude corresponds to just after the middle of winter in the southern hemisphere.

λ_CRISM (μm)	λ_dust (μm)
0.566	0.575
0.801	0.800
0.951	0.950
1.277	1.300
1.513	1.505
2.271	2.250

Table 3.3. Wavelengths at which analyses were conducted (λ_CRISM) compared to wavelengths with derived dust parameters (λ_dust).

	reference	32-stream	seed w=0.2, b=-0.3	2-μm dust radius
minimum w	0.472	0.473	0.472	0.485
maximum w	0.578	0.578	0.596	0.586
average w	0.557	0.557	0.557	0.568
standard deviation w	0.009	0.009	0.009	0.009
minimum b	-0.260	-0.258	-0.258	-0.238
maximum b	-0.140	-0.141	0.000	-0.124
average b	-0.198	-0.198	-0.198	-0.179
standard deviation b	0.010	0.010	0.013	0.010
minimum χ2	0.794	0.797	0.793	0.280
maximum χ2	47.550	47.745	47.550	50.636
average χ2	3.653	3.657	3.721	2.553
standard deviation χ2	1.873	1.877	2.424	1.878

Table 3.4. The effects that various changes to the scattering parameter calculation have on parameter statistics. The reference computation is 16-stream with a seed value of w=0.5, b=-0.2. Sensitivity tests shown here were conducted at 0.801 μm. Sensitivity tests at 2.277 μm gave similar results.

References

Hapke, B. (1993), *Theory of Reflectance and Emittance Spectroscopy,* Cambridge Univ. Press, New York.

Lemmon, M. T., M. J. Wolff, M. D. Smith, R. T. Clancy, D. Banfield, G. A. Landis, A. Ghosh, P. H. Smith, N. Spanovich, B. Whitney, P. Whelley, R. Greeley, S. Thompson, J. F. Bell III, S. W. Squyres (2004), Atmospheric imaging results from the Mars Exploration Rovers: Spirit and opportunity, *Science*, 306, 1753–1756, doi:10.1126/science.1104474.

Markwardt, C. B. (2008) "Non-Linear Least Squares Fitting in IDL with MPFIT," in proc. *Astronomical Data Analysis Software and Systems XVIII.*

Murchie, S., E. Guinness, and S. Slavney (2006), CRISM Data Product Software Interface Specification, Natl. Aeronaut. and Space Admin.,Washington, D. C. (Available at http://pds-geosciences.wustl.edu/mro/mro-m-crism-2-edr-v1/mrocr_0001/document/crism_dpsis.pdf)

Smith, M. D. (2002), The annual cycle of water vapor on Mars as observed by the Thermal Emission Spectrometer, *Journal of Geophysical Research*, 107(E11), 5115, doi:10.1029/2001JE001522.

Smith, M. D. (2008), Spacecraft Observations of the Martian Atmosphere, *Annu. Rev. Earth Planet. Sci.*, 36, 191-219.

Stamnes, K., S. Tsay, W. Wiscombe, K. Jayaweera (1988), Numerically stable algorithm for discrete-ordinate-method radiative transfer in multiple scattering and emitting layered media, *Applied Optics*, 27, 2502-2509.

Tillman, J. E., N. C. Johnson, P. Guttorp, and D. B. Percival (1993), The Martian annual atmospheric pressure cycle – Years without great dust storms, *of Geophysical Research*,

98, 10963–10971.

Wolff, M. J., M. D. Smith, R. T. Clancy, R. Arvidson, M. Kahre, F. Seelos IV, S. Murchie, and H. Savijärvi (2009), Wavelength dependence of dust aerosol single scattering albedo as observed by the Compact Reconnaissance Imaging Spectrometer, *Journal of Geophysical Research*, 114, E00D04, doi:10.1029/2009JE003350.

Chapter 4 : Interpretation of Surface Scattering Properties at Opportunity's Traverse Region

4.1 Introduction

This chapter focuses on the interpretation of the surface scattering properties derived using the methods outlined in Chapter 3. First, an overview of the region traversed by the Opportunity rover is presented (Section 4.2), paying particular attention to the area around Victoria, a large crater visited by the rover, over which a particularly high-quality CRISM observation was acquired. Then in Section 4.3, the scattering parameter results are described. In Section 4.4, these results are compared to the results of previous workers who have spectrophotometrically analyzed the near-surface data provided by Opportunity. In Section 4.5, results are interpreted in terms of surface roughness, and it is shown that, while large-scale roughness in the form of ripples does not affect backscatter, small-scale roughness in the form of hematite-rich spherules dominates the observed backscatter patterns.

4.2 The Opportunity Traverse Region: An Overview

The investigation of surface scattering properties presented in this dissertation is focused on the region where the only (at time of publication) operational spacecraft on the surface of Mars, the Opportunity rover is located. Opportunity's landing site is relatively close to the equator (1.95 $^{\circ}$S, 354.47 $^{\circ}$E), in a region called Meridiani Planum, which is Noachian or Early Hesperian in age based on crater-counting statistics [*Arvidson et al*., 2006]. For an overview of the Opportunity mission and results, see *Arvidson et al*. [2011] and *Squyres et al*. [2006].

The region around the traverse consists of variable thicknesses of soil over bedrock, with bedrock exposed in some regions (based on images from the High Resolution Imaging Science Experiment (HiRISE on MRO), the Context Camera (CTX on MRO), and Pancam). Soil consists of basaltic grains, dust, and hematite (Fe_2O_3) -rich spherules (lower limit 24% hematite [*Morris et al*., 2006]). Other workers have discussed the history of water in this region, so only a few brief points are mentioned here. *Andrews-Hanna et al*. [2007] showed that the original deposits in Meridiani likely formed from groundwater upwelling and subsequent evaporation which left behind layered sulfate-rich sediment. Hematite-rich spherules are present in the region and indicate diagenesis via liquid water [*Squyres et al*., 2006]. Additionally, the presence of sulfate-rich cross-laminated bedrock is evidence for rock formation in flowing water [*Squyres et al*., 2004a; *Squyres et al*., 2004b, *Squyres et al*., 2006].

The majority of the rover's 34.4-km traverse (as of 5/7/2012) occurred over a high-elevation (generally 10-15 meters above surrounding terrain) aeolian ripple-rich semi-triangular feature located northwest of the 22-kilometer-wide Endeavour crater (Figure 3.3; as of 5/7/2012, the Opportunity rover is located on the rim of Endeavour). This semi-triangular feature has wider ripples and lower thermal inertia (Figure 4.1) than surrounding areas, with the exception of similarly heavily-rippled, low thermal-inertia areas that comprise the wind streaks extending from small nearby craters (Figure 4.2). The lower thermal inertia of the semi-triangular region indicates that the material within the top few centimeters of the semi-triangular feature has a smaller particle size and/or is less indurated than surrounding surfaces [*Mellon et al*., 2000]. In Figure 4.1, the visible

portion of the semi-triangular region has been outlined. Note that this most densely-rippled area occurs within the low-thermal inertia region. The ripple maps in Figures 4.1 and 4.2 were generated from images from HiRISE using a terrain classifier developed by Yasuhiro Katayama and run by Paolo Bellutta at NASA's Jet Propulsion Laboratory. For a description of the ripple map generation using a machine vision algorithm involving image segmentation through pattern (texture) recognition, see *Golombek et al.* [2012]. The algorithm identifies features and uses their spatial distribution, size, and alignment to classify terrain. Thermal inertia information was derived by Michael Mellon using data from the Thermal Emission Imaging System (THEMIS) onboard the Mars Odyssey (ODY) spacecraft.

The Opportunity rover spent considerable time around Victoria crater (Figure 4.3) [*Squyres et al.*, 2006]. At about 750-meters in diameter and about 75 meters deep [*Grant et al.*, 2008], Victoria is the second largest crater visited by the rover, and it was the largest at the time FRT0000B6B5 was acquired. Likely, when Victoria formed, it was ~600 meters in diameter and ~125 meters deep [*Grant et al.*, 2008]. Victoria crater has several wind streaks emanating from the northern and eastern sections of its rim, and observations from the Opportunity rover indicate that the streaks consist in large part of basaltic sand that had been trapped in the crater and subsequently blown out in streaks [*Geissler et al*., 2008]. The relatively soft sulfate-rich ejecta blocks have been eroded to the level of the surrounding surface and are visible only near the inner edge of the 4-5 meter-high, 120-200 meter-wide rim and the top of the crater walls [*Squyres et al*., 2009; *Arvidson et al*., 2011].

4.3 Scattering Property Results at the Opportunity Traverse Region

Using the method described in Chapter 3, maps of single scattering albedo, *w* (Figure 4.4) and asymmetry parameter, *b* (Figure 4.5) were generated for each of the wavelengths studied. These maps cover the area traversed by Opportunity on sols 791-813 and 848-1793. Associated χ^2 values for the maps are shown in Figure 4.6. For many of the pixels where χ^2 greatly exceeds the standard deviation (due to the fit being less well-constrained for particular pixels), *w* and *b* values have been flagged as unreliable and are not shown in parameter maps. Certain pixels with high χ^2 were left in the parameter maps because variations in albedo (observed in the high-resolution central scan or in HiRISE images) contributed to the χ^2, so for these pixels, the χ^2 value does not indicate a poorly constrained fit, rather it indicates the extent to which the returned parameters are averages over the different units contained within pixels of different sizes from each image within the FRT (see Chapter 3 for a description of how pixel size varies and of how the scattering parameter maps were generated). Figure 4.7.a shows how I/F at 0.801 μm varies with phase angle for the CRISM data for a pixel with a χ^2 value close to average (within $1/5^{th}$ of a standard deviation). Also plotted is the I/F resulting from the best-fit parameters (which were w=0.559 and b=-0.187 for this pixel) for comparison. Since the figure includes actual data that were obtained at varying emergence angles, there are two "arms" to the plot, which is actually a projection from a three-dimensional space with axes of I/F, emergence angle, andphase angle onto the two-dimension space depicted by the figure axes. Included in the figure is a plot with an offset from the best-fit *w* value for comparison. Figure 4.7.b shows a similar plot, but for the longest

wavelength analyzed in this study: 2.271 μm. The fit is worse at this wavelength than at 0.801 μm. In fact, the χ^2 value of the fit increases monotonically with wavelength, as shown in Figure 4.8. This trend may be the result of a combination of error in estimates for atmospheric parameters (see Chapter 3), and that the limited forms that a phase function can take when it is described by one parameter may be insufficient to closely match the phase function at longer wavelengths. Despite the higher χ^2 values at longer wavelengths, results are still constrained enough to identify the average scattering parameter trends with wavelength over the whole study area. However, for comparison of less spatially extensive regions within the area of interest, it is advisable to rely on the shorter wavelengths, which have the more reliable fits. Although χ^2 increases monotonically with wavelength, the standard deviation in the generated maps of asymmetry parameter decreases, then increases, and then decreases with wavelength (i.e. no monotonic pattern; see Figure 4.8), indicating that the standard deviation in asymmetry parameter is dominated by variation in surface properties rather than by the error represented by the χ^2 indicator (this result is what one would expect from looking at Figure 4.5, where surface features such as Victoria's ejecta apron are easily identified).

By concatenating the maps of best-fit scattering parameters for several wavelengths (i.e. by creating spectral cubes from these maps), spectra for regions of interest can then be retrieved. Several regions that span the study area (Figure 4.9) were selected, and Figure 4.10 shows single scattering albedo spectra and asymmetry parameter spectra for these regions (See Figure 4.11 for an average, representative I/F spectrum for the study area. Wavelengths for scattering parameter analysis have been

marked on the figure). From the scattering parameter spectra, it is apparent that variations in single scattering albedo are anti-correlated to variations in the asymmetry of the phase function, in the spectral domain. The entire study area is backscattering at all wavelengths studied, however some regions are more backscattering than others. The region (shaded red for visualization in Figure 4.9) located in the southwestern portion of Victoria's ejecta apron is relatively free of aeolian deposits and is more backscattering than other regions of interest (including regions of the ejecta apron where wind streaks are located; see Figure 4.12). Additionally, there is a general trend in which surfaces become more backscattering with increasing wavelength.

Figure 4.13 shows a plot of asymmetry parameter versus single scattering albedo at 0.801 μm for the entire study area. From this plot, it is apparent that, with regard to spatial variation, the asymmetry parameter increases as single scattering albedo increases. Similar plots at other wavelengths show the same trends. However, as discussed earlier in this section, if instead of looking at the spatial variations at any given wavelength, the variations in the spectral domain are considered, the opposite trend is observed (compare Figure 4.10a with Figure 4.10b to see the inverse relationship). Essentially, spatial variations in single scattering albedo have a direct positive correlation with spatial variations in the asymmetry of the phase function, whereas in the spectral domain, variations in single scattering albedo are anti-correlated to variations in the asymmetry of the phase function. This observation does not represent an inconsistency, rather it suggests that the surface property (discussed in Section 4.5) which has a dominant effect on the relationship between spatial variations in w and b is not the same as the surface

property which has a dominant effect on the relationship between variations in w and b in the spectral domain.

To inspect the variations along the trendline in the *b* vs. *w* plot (Figure 4.13), different areas along the trend line were colorized and then mapped to where they occur on the surface. This is shown in Figure 4.14. The top panel shows that the class of region designated by cyan and pink colors has high single scattering albedo and high asymmetry parameter values. The bottom panel of the figure indicates that this class corresponds to a relatively bedrock-rich curved strip of terrain. Classes designated yellow and dark blue are in the middle of the w-b trendline, and they are located on either side of the bedrock-rich strip of terrain. And even further to either side are the green and red classes, which have low single scattering albedos and low asymmetry parameters. The pink and red classes can be taken as end-members. Figure 4.15 shows HiRISE images corresponding to six pixels in the high-albedo, high asymmetry parameter pink class, and Figure 4.16 shows HiRISE images corresponding to six pixels in the low albedo, low asymmetry parameter red class. It is apparent from these HiRISE images that the pink end-member has a greater bedrock component than the red end-member. For classes that are adjacent to each other in *w*-*b* space, the difference is not distinguishable by eye, as it is for the end-members. There are also some regions that are located away from the main trend-line. Notably, several wind streaks emanating from Victoria crater are lower albedo and less backscattering than other soils (Figure 4.17). The nature of the surface units can also be seen in a map of thermal inertia in Figure 4.18 which shows the thermal inertia for the regions presented in Figures 4.9 and 4.17.

Thermal inertia is affected by a number of factors, including the presence of exposed bedrock.

4.4 Comparison of Orbital and Rover Scattering Parameter Results

Meridiani Planum is one of six regions on Mars where there exist both orbital and near-surface observations. This combination of data sources is beneficial for the interpretation and validation of scattering parameter results. While this section focuses on the comparison of the scattering parameters themselves, Section 4.5 deals with near-surface images and how they aid in interpretation of the orbital results. Included in Figure 4.10 is a comparison with the results of *Johnson et al.*'s [2006a] spectroscopic analyses based on data acquired from the ground by the Opportunity rover. The blue curves represent results from near-surface observations of an endmember soil type that is covered densely with hematite-rich, spherical concretions. Note that the trends exhibited in the spectral variation of the scattering parameters are similar for both the orbital and the ground-based analyses. It is not surprising that the single scattering albedo obtained from the orbital observations is higher than that obtained from ground and the asymmetry parameter is lower. This result is partially due to the fact that, in images acquired from orbit, each pixel consists of multiple surface units (often including bright bedrock), not just a spherule-covered soil endmember. Further, *Johnson et al*. [2006a] used a version of the Hapke model that had a separate parameter for roughness [*Hapke*, 1993], so their asymmetry parameter should not be affected as much by roughness. Therefore, differences in results are consistent with what is expected due to differences in models, but results still show marked similarities.

4.5 Surface Roughness at the Opportunity Traverse Region

4.5.1 Large Scale Roughness

Now that surface scattering parameters have been mapped for the extent of the study area, the next step is to determine which surface characteristics are responsible for the observed scattering patterns. There is meter-scale roughness in this region, in the form of north-south trending ripples. It is reasonable to compare scattering patterns seen in Figures 4.4 and 4.5 to ripple wavelength (crest-to-crest distance, which is directly related to ripple height) which varies in this region. Figure 4.2 shows a map of ripple wavelength, with warmer colors indicating larger ripples. There does not appear to be a strong correlation between ripple wavelength and scattering behavior (see Figure 4.19). For example, in terms of ripple wavelength, Victoria's ejecta apron looks relatively homogeneous, whereas, parts of the ejecta apron are more backscattering than other parts. Additionally, there are many large ripples just outside Victoria's apron, but this variation in ripple cover does not appear to translate to a difference in scattering properties. This result is probably at least partially due to the observational setup and its relation to ripple orientation. Ripples in this region trend north-south, and CRISM's flight path is south to north, so all the phase information is in that direction. However, one might expect some slight effect due to the fact that the ripples merge and fork, creating regions where one would expect shadowing in the north-south direction. Ripple characteristics can be seen in the close-in views of ripples shown in Figures 4.15 and 4.16.

4.5.2 Small Scale Roughness

In Section 4.5.1, large scale roughness does not appear to have a strong influence on scattering properties, so there must be a different surface property that can explain the observed scattering patterns. Small scale (millimeter-scale) roughness on and around the Opportunity traverse is dominated by the presence of hematite-rich, spherical concretions and is also affected by differences in bedrock and soil texture. The size and burial depth of the spherules (both of which affect areal abundance) significantly affects the scattering characteristics observed from orbit, as will be shown later in this chapter. Figure 4.20 shows the CRISM I/F at 0.801 μm, a wavelength at which surface features are easily identified. Some features are labeled, several of which incorporate wind-blown material. It is possible, from looking at these features, to make inferences regarding small-scale surface roughness. Aeolian deposition often has a smoothing effect at millimeter scales, and wind streaks, as well as craters filled with aeolian deposits, tend to be relatively smooth at these scales compared with other regions in the study area (see Figure 4.21 for rover observations showing textural smoothing). This smoothness is interpreted to be due to sand and dust, which have been blown into gaps between spherules, thus burying the spherules and smoothing the surface out. In Figure 4.4, wind streaks extending from the eastern rim of Victoria are fainter than wind streaks extending from the northeastern rim (this is likely due to variable basaltic sand cover). In Figure 4.5, it is apparent that even the fainter wind streaks have a higher asymmetry parameter than the rest of the ejecta blanket.

In the region surrounding Opportunity's traverse, hematite-rich spherules are embedded in bedrock, and they are harder than the bedrock, so when the bedrock weathers away, they are preserved as a lag deposit. Therefore the more weathered, soil-rich surfaces will have denser spherule cover and greater small-scale roughness than more bedrock-rich surfaces. Additionally, spherule size decreased as Opportunity drove upslope (and likely upsection) toward Victoria crater; however, spherule size increased again once Opportunity reached Victoria crater's ejecta apron, likely because the ejecta blocks came from depth (layers similar to those seen earlier in the traverse) [*Squyres et al*., 2009]. The spherule size difference related to Victoria's ejecta apron can be seen in Figure 4.22. Looking back at Figure 4.5, Victoria's ejecta apron (excluding sections located on large wind streaks) is more backscattering than surrounding regions, this indicates a correlation between spherule size and amount of backscatter. Interestingly, the fact that the backscattering pattern is dominated by spherule-related roughness rather than ripple-related roughness is in agreement with the work of *Shepard and Campbell* [1998], although that study was conducted on fractal surfaces. After investigating several model surfaces, *Shepard and Campbell* [1998] note: "We hypothesize that the scale which dominates surface shadowing and by extension photometric roughness is the smallest surface scale for which shadows exist." Further, other workers, including *Goguen et al*. [2010] who investigated lunar photometry, have noted that sub-millimeter and millimeter-scale roughness have the greatest effect on observed photometry as compared to larger-scale roughness. The reason small-scale roughness dominates the photometric signature from roughness is likely because, for natural surfaces, slopes are

often highest at small spatial scales. It is at the smaller scales that one is more likely to find higher cohesion values that take the slopes to angles greater than the angle of repose [*Helfenstein*, 1988].

In light of the information presented in this chapter on the relation between asymmetry parameter and millimeter-scale roughness, it is instructive to revisit Figure 4.13. Since a more negative asymmetry parameter indicates a rougher surface at small scales, Figure 4.13 indicates that as single scattering albedo goes up, apparent small-scale roughness decreases. As a consistency check, it is worthwhile to see if the trend between asymmetry parameter and single scattering albedo corresponds to the trend between roughness and single scattering albedo observed by other workers. *Johnson et al*. [2006a, 2006b] see the same trend between roughness (in their case, roughness is in the form of the Hapke roughness parameter Θ-bar) and single scattering albedo in their results based on near-surface Panoramic Camera (Pancam) observations at both Meridiani Planum and Gusev crater. For the study area shown in Figure 4.4, the observed *b* vs. *w* trend in Figure 4.13 is in large part due to surface roughness caused by hematite-rich spherules. As shown in Figure 4.14, the trend-line is a mixing line between bedrock-rich and bedrock-poor end-members. High albedo surfaces are in general more bedrock-rich and bedrock in this area tends to be less rough than soil on millimeter-scales (see Figure 4.23), this is due to fewer hematite-rich spherules on the surface of bedrock than on the surface of soil. These spherules will be discussed in more detail later in this chapter.

As has been shown, for several regions in the study area, small-scale surface roughness can be observed from the ground. These regions include relatively bedrock-

rich areas as well as areas with large ripples, and notably, Opportunity has traversed Victoria's ejecta apron including wind streaks extending away from Victoria's rim. Most of Victoria's apron is very well eroded and exhibits a dense cover of relatively large hematite-rich spherules (Figure 4.22, Figure 4.24). This textural cover results in a more backscattering surface than surrounding regions, as can be seen in the CRISM scattering parameter results (Figures 4.5 and 4.10). Figure 4.25 shows that the same overall patterns occur in maps of asymmetry parameter made at several different wavelengths. There are regions of the ejecta apron that are less backscattering, namely, several wind streaks on the northern and eastern portions of the apron. This correlation indicates that small-scale roughness is dominating the amount of backscatter seen from orbit. Further, there is confirmation of this effect from *in situ* and near-surface observations, specifically rover-acquired data analyzed by *Geissler et al.* [2008]. Figure 4.21 is modified from *Geissler et al.* [2008] and shows images from the rover's Microscopic Imager (MI) taken both off-wind-streak and on-wind-streak. It is apparent that the burial depth of the spherules is greater for areas in wind streaks as material has been deposited between spherules. *Geissler et al*. [2008] also conducted a photometric analysis from rover Pancam images at 0.754 μm showing that areas on the wind streak are less backscattering. Essentially, what is happening is the spherules are topographic elements that create a shadowing effect resulting in the preferential backscatter. For a geometric interpretation of this phenomenon, see Fig. 4.26. This phenomenon has also been observed in lab experiments conducted by *Johnson et al*. [2007] in which hematite-rich spherules were removed from an analog sample paleosol from Sioux City, Iowa and its

scattering properties were determined from matrix powder, then the spherules were reintroduced and a significant increase in backscatter was observed as well as a significant decrease in albedo.

The hematite-rich spherules responsible for the millimeter-scale surface roughness at the Opportunity traverse region have been studied by several workers, and summaries are given by *Calvin et al.* [2008] and *Weitz et al.* [2006]. Therefore, just a few spherule characteristics will be mentioned here. Spherules are 2-5 millimeters in size in the area around Victoria crater [*Geissler et al*., 2008], and on average 2.9 ± 1.2 millimeters over much of the traverse leading to Victoria crater [*Weitz et al*., 2006]. *Hynek and Singer* [2007] found that the size of the hematitic spherules observed by Opportunity appears to be directly correlated with thermal inertia, independent of spherule abundance. Given the variations in spherule size at Victoria's apron, one might expect this variation to translate to variations in thermal inertia (Figure 4.27), however the situation is more complicated because bedrock is also a factor and the transition to the apron is also a transition to very low bedrock exposure; further, spherule burial is a factor.

Earlier in this chapter, it was mentioned that the surfaces in the region Opportunity has been traversing tend to become more backscattering with increasing wavelength. The simplest explanation for this trend would be that the topographic elements (spherules) that are causing the shadowing effect (and therefore the backscatter) have different spectral properties than the rest of the surface. In order to be consistent with the observed spectral trend in backscatter, the ratio of spherule brightness to

substrate brightness must increase at long wavelengths (longer than 1.009 μm). Unfortunately, spherule and substrate spectra at these long wavelengths have not been acquired (the longest wavelength Pancam detects is 1.009 μm). As a qualitative example of the spectral differences that would be in accord with the observed backscatter trend, Figure 4.28 shows spectra of hematite and basalt from the CRISM Spectral Library (available online through the Planetary Data System's Orbital Data Explorer). If the spherules are brighter than the substrate at longer wavelengths, the backscattered light (resulting from a situation similar to that in Figure 4.26.b.) should be redder than the forward scattered light (resulting from a situation similar to that in Figure 4.26.a.). These differences should lead to a pattern where backscattering increases with increasing wavelength (since the spherules would get more reflective with increasing wavelength), as is seen in 4.10.b. To further investigate the implications of the derived wavelength-dependent single scattering albedo and asymmetry parameter, these parameters were used to reconstruct I/F at various illustrative viewing geometries, all corresponding to an incidence angle of 30°, but with varying emergence and phase angles. Figure 4.29 shows the results: the most backscattering geometry corresponds to the reddest spectrum. This agrees with the asymmetry parameter being the most negative at the reddest wavelength (2.27 μm) investigated. This would make sense in terms of the spectral properties of spherules only if they are redder than basalt (i.e. redder slope over the whole wavelength range being considered).

Thus far, the atmospheric and surface contributions to observed reflection have been separated in order to map scattering parameters for the entire study area. Data from

the portion of the study area traversed by the Opportunity rover have been used to confirm that the dominant factor affecting the backscatter pattern is millimeter-scale roughness. Note that no assumptions have been made about how roughness is parameterized, instead, after deriving the phase function, and upon comparison to near-surface observations, it was determined that the dominant effect on the anisotropy of the phase function is millimeter-scale roughness, which in this region is primarily due to the presence, size, and burial depth of hematite-rich spherules. Further, the available information on surface roughness has been extended to a much larger region that stretches for kilometers to the east and west of the rover traverse.

Figures

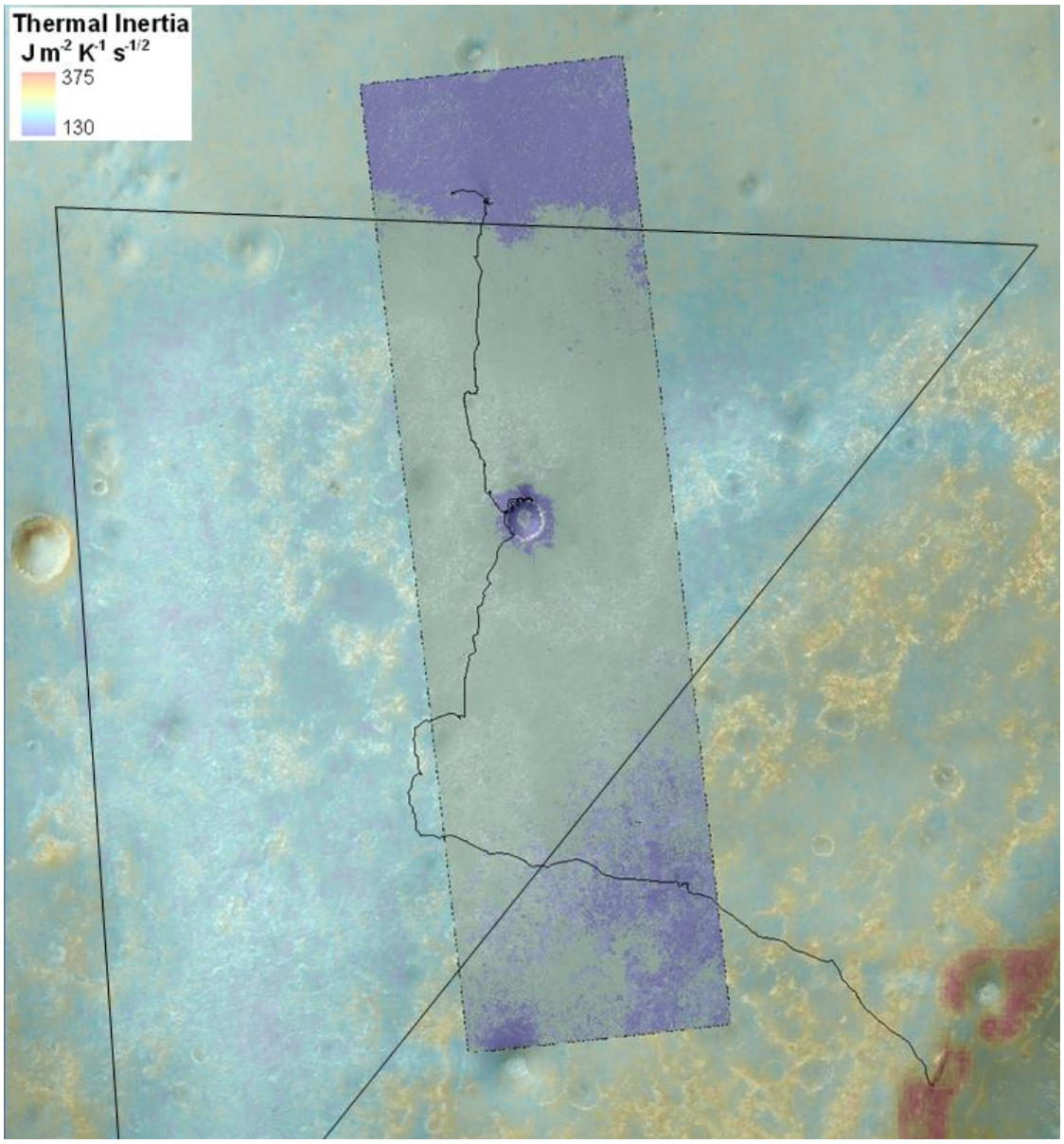

Figure 4.1. HiRISE ripple classification map (green: terrain with many ripples over 3 meters in crest-to-crest distance, blue: terrain with few ripples over 3 meters crest-to-crest) overlain on thermal inertia on CTX. An area of low thermal inertia has been

outlined. The ripple map was generated using HiRISE image PSP_009141_1780_RED. Note that the region with larger ripples also has lower thermal inertia.

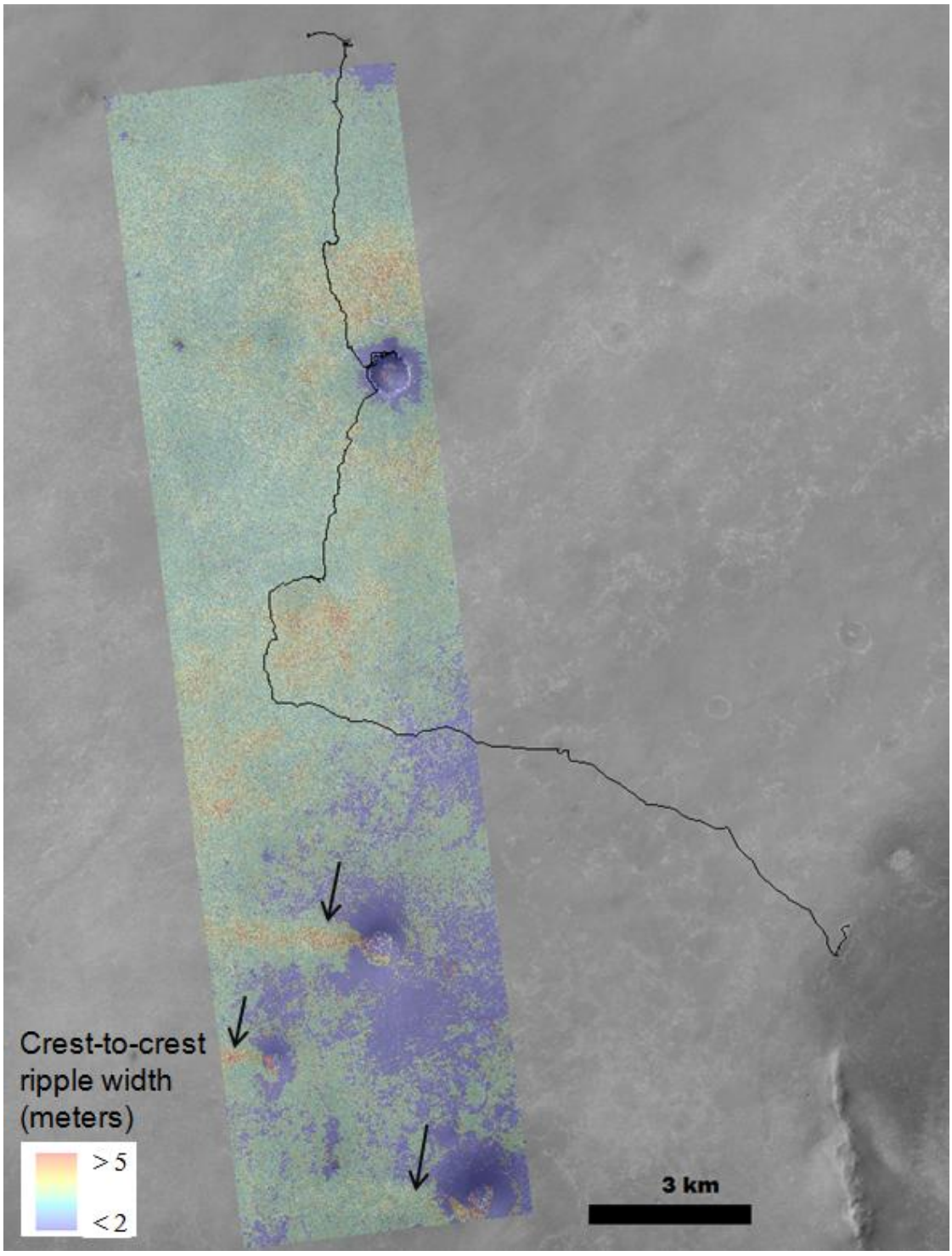

Figure 4.2. Map of approximate ripple width, courtesy of Paolo Bellutta. Warmer colors indicate greater ripple width. The "triangle" shown in Figure 4.1 and nearby wind streaks

(black arrows) are ripple-dominated. The ripple map is based on HiRISE image ESP_016644_1780_RED.

Figure 4.3. Victoria crater (from a portion of HiRISE color image TRA_000873_1780). Dark basaltic streaks are visible coming from the northeastern rim. Fainter streaks emanate from the eastern rim.

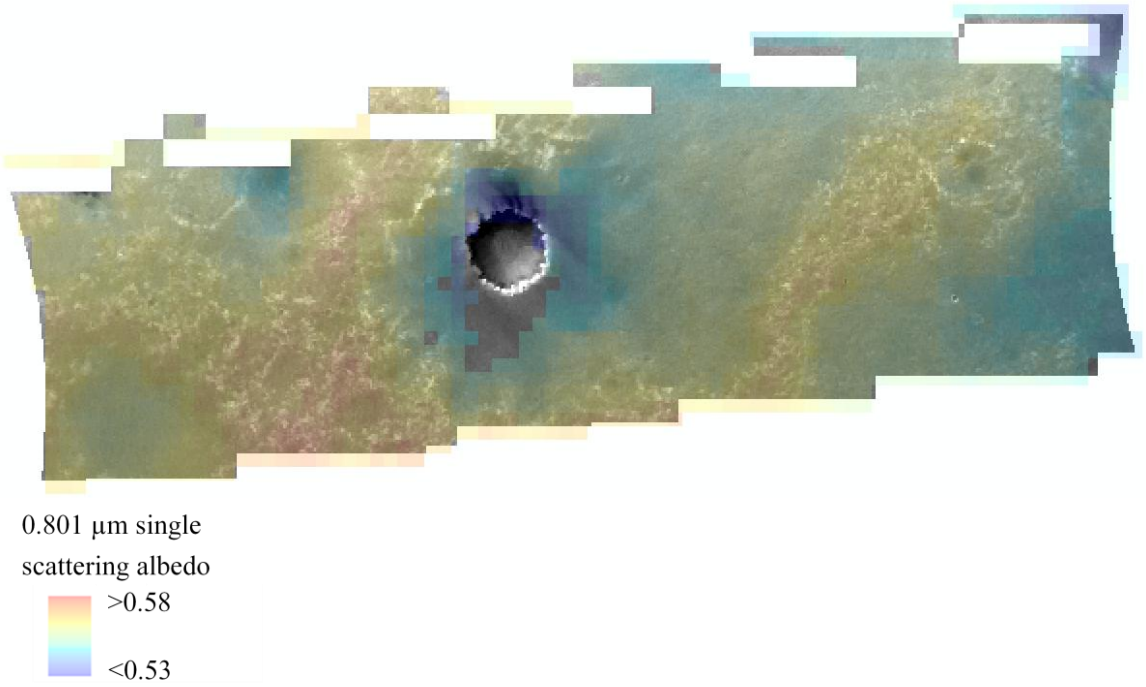

Figure 4.4. Example of a map of single scattering albedo (at 0.801 µm). The pattern is similar to the original I/F pattern (shown in background).

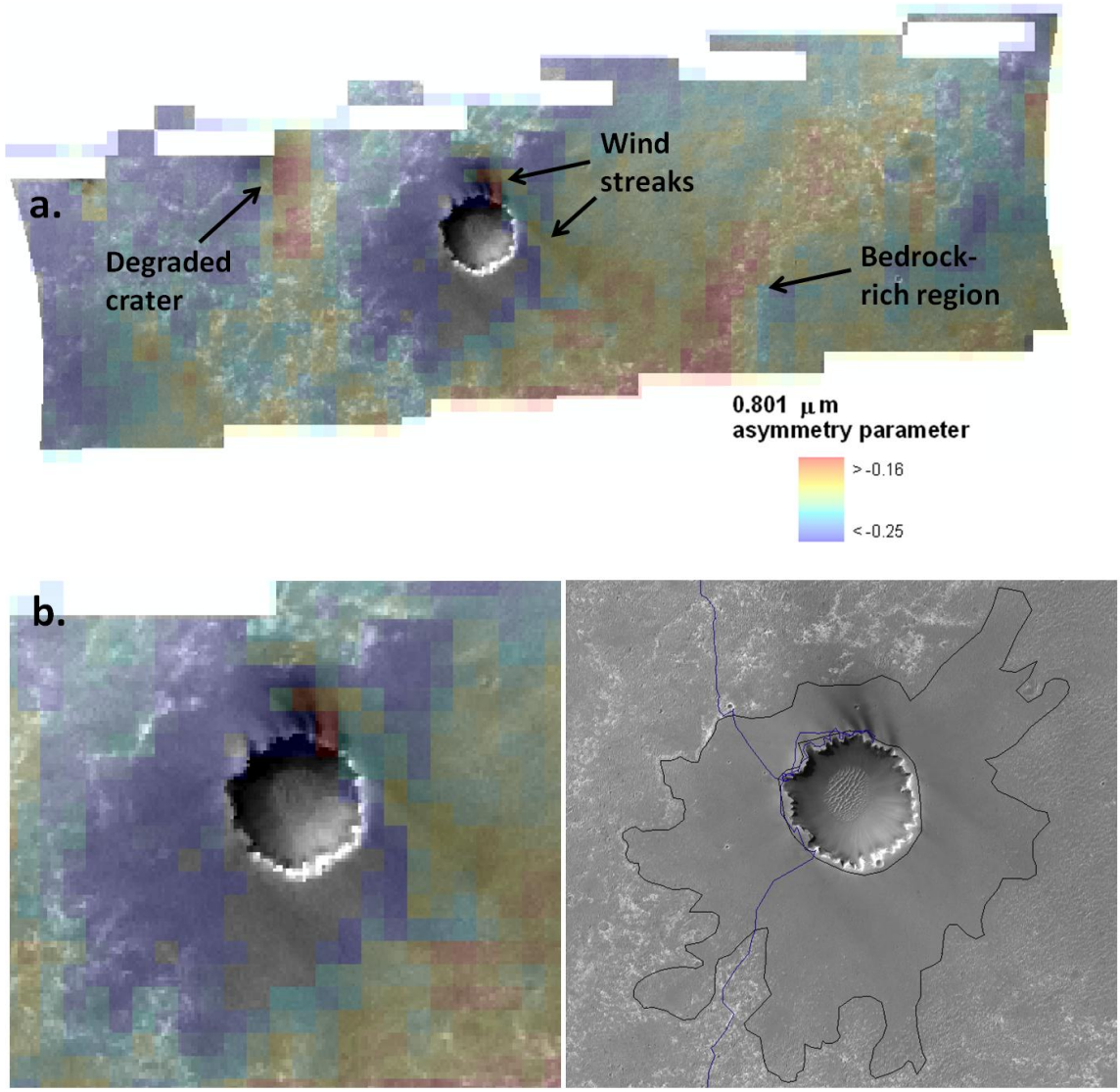

Figure 4.5. Example of an asymmetry parameter map.

a. Full asymmetry parameter map with cooler colors indicating greater small-scale surface roughness. Background is CRISM I/F at 0.801 µm. Artifacts due to topography and other high-χ^2 pixels are removed.

b. (left) Zoom-in on Victoria crater & ejecta apron. (right) HiRISE image of Victoria with outlined apron.

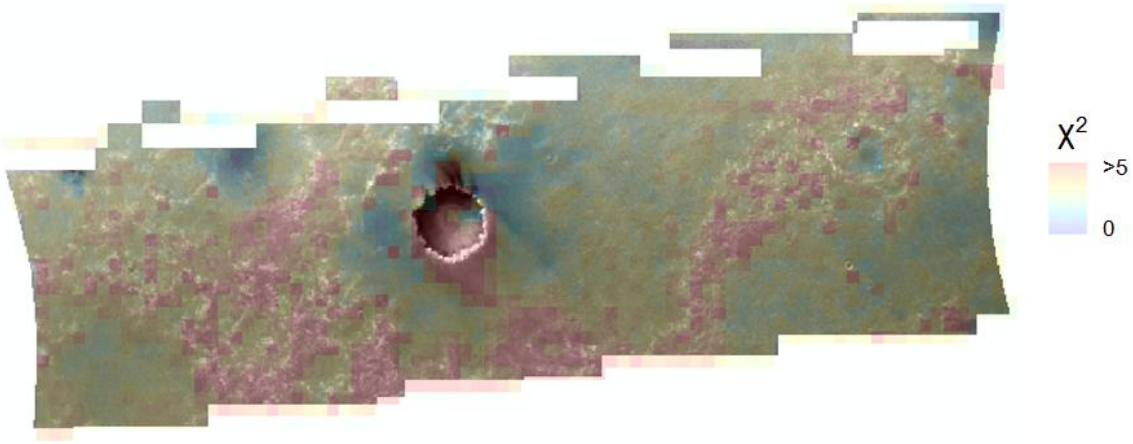

Figure 4.6. Corresponding χ2 values for parameter maps at 0.801 μm.

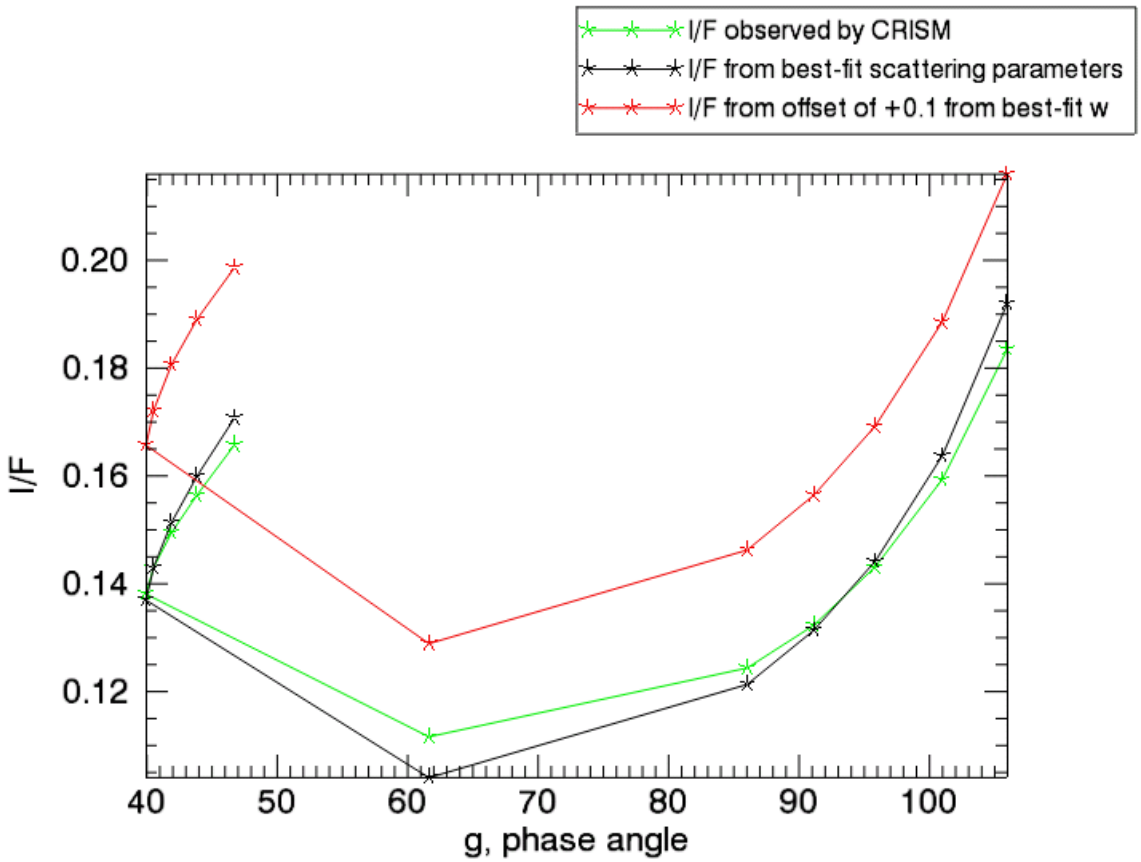

Figure 4.7. Data plotted against fit at two selected wavelengths.

a. Data vs. fit at 0.801 µm for w=0.559 and b=-0.187. The effect of varying w is also shown.

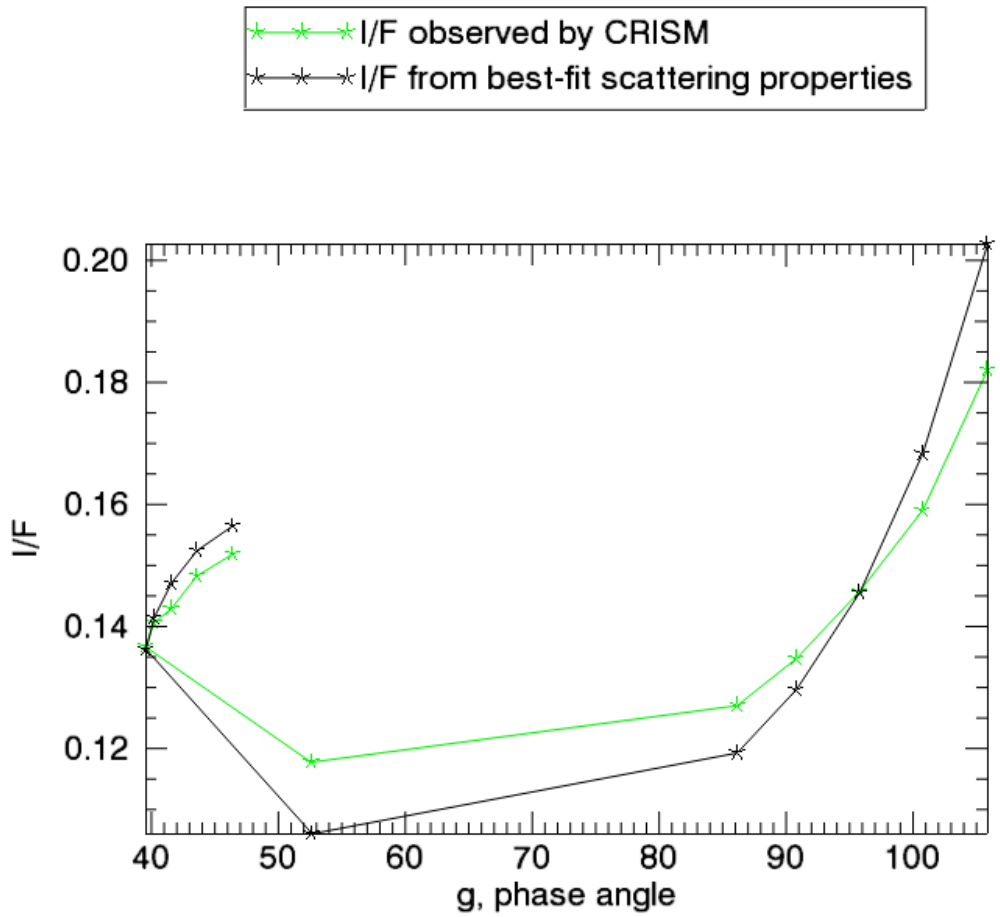

Figure 4.7. b. Data vs. fit at 2.271 μm for w=0.561 and b=-0.250.

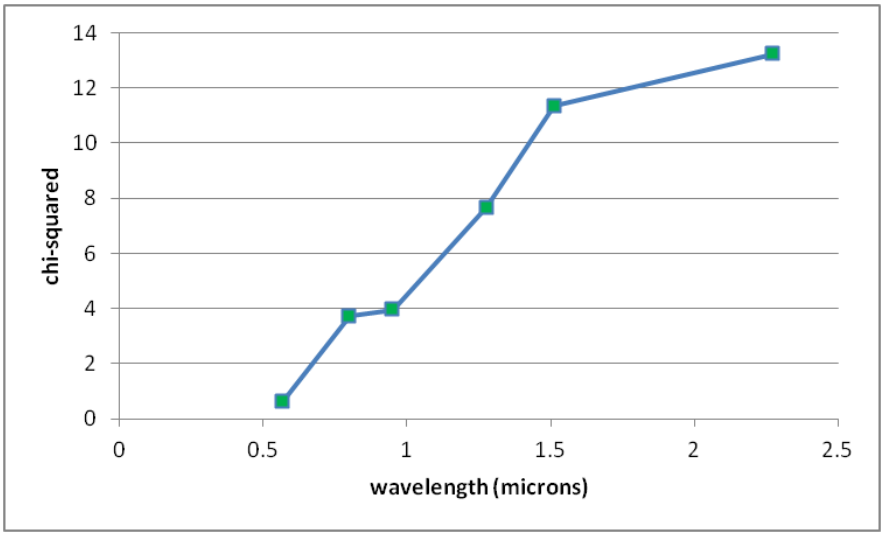

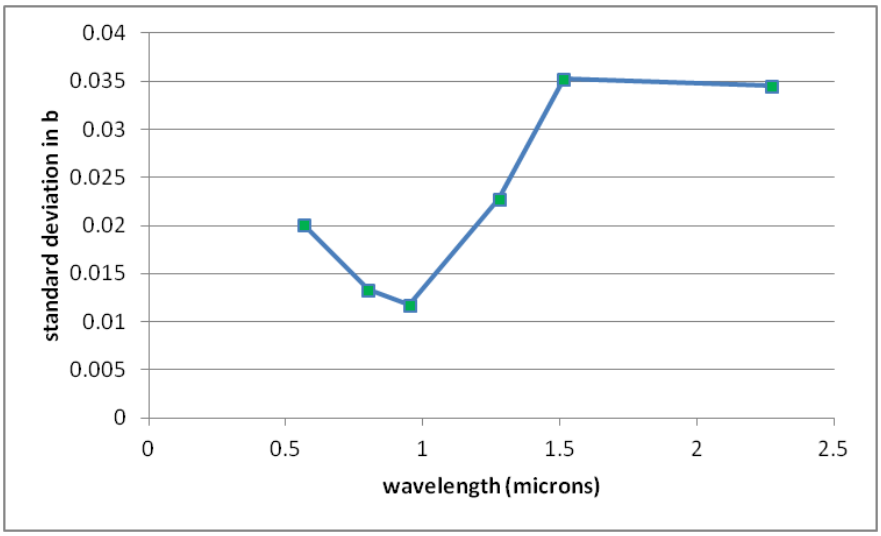

Figure 4.8. Statistics as a function of wavelength. Top panel: χ^2 of the model fits as a function of wavelength. Bottom panel: standard deviation in asymmetry parameter over the entire study area as a function of wavelength.

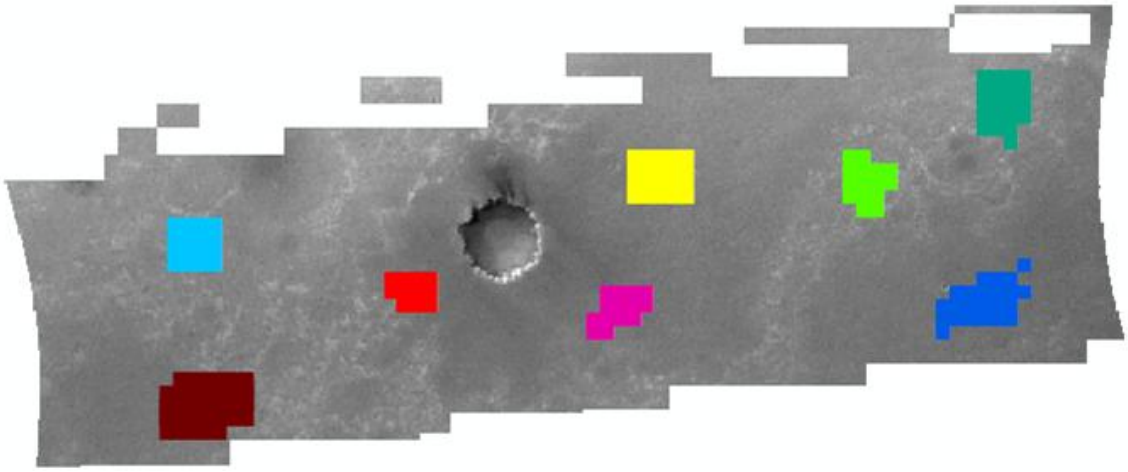

Figure 4.9. Regions of interest corresponding to spectra in Figure 4.10. Some near-surface views of terrain near Victoria crater are shown in Figure 4.24.

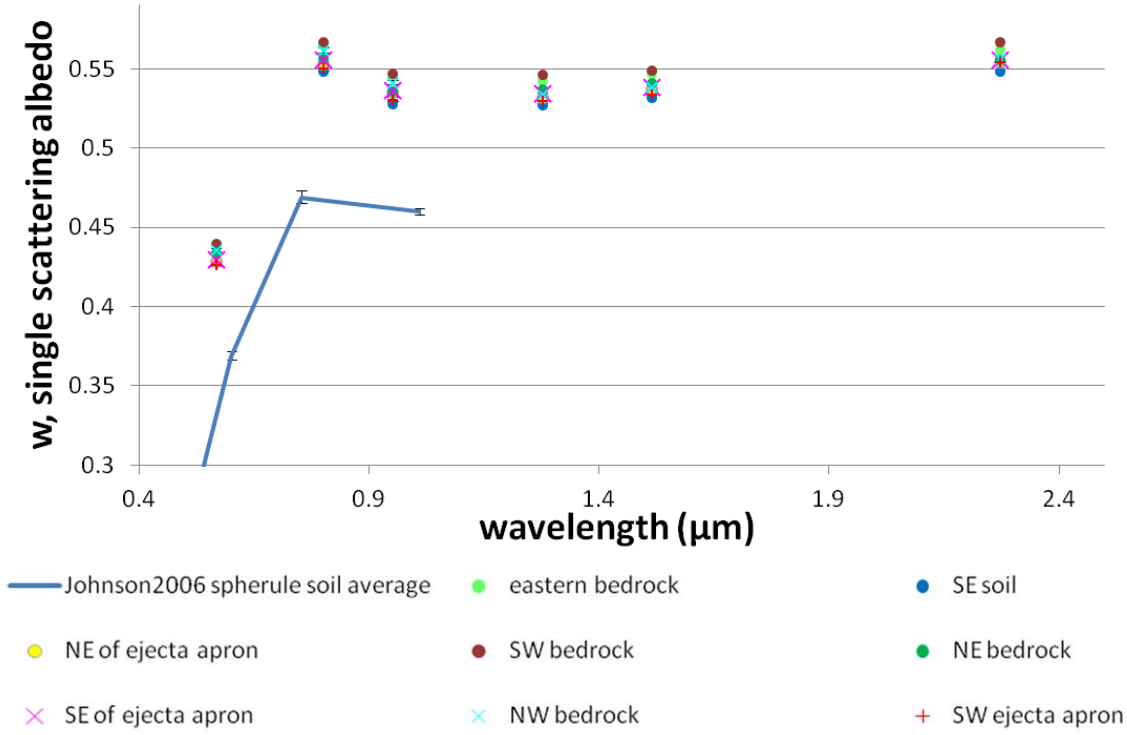

Figure 4.10. Scattering parameter spectra for several regions of interest.

a. Single scattering albedo for the regions of interest shown in Figure 4.9. Near-surface results from *Johnson et al*. [2006a] for regions with an abundance of spherules are included for comparison (blue line). To see these wavelengths relative to a spatially averaged full-spectral resolution original I/F spectrum, see Figure 4.11. Error bars, representing relative error, are the same for all regions and are smaller than the icons representing the regions. Absolute error is ±0.02. While absolute error will not change the trend shown in the figure, it will shift the trend up or down (to higher or lower single scattering albedo). A discussion of relative and absolute error has been included in Chapter 3. Note that the names given to regions of interest are general designators, for

example, the region labeled “NW bedrock” does not consist entirely of bedrock, but is more bedrock-rich than units labeled “soil”.

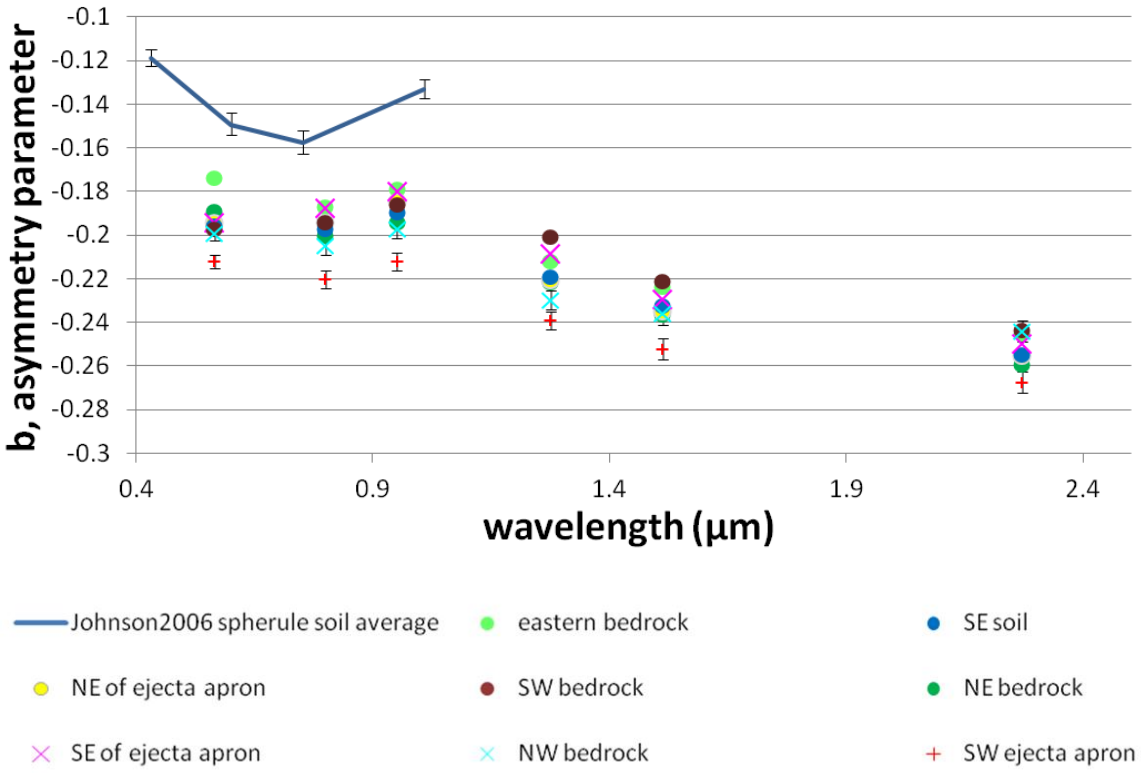

Figure 4.10. b. Asymmetry parameter for the regions of interest shown in Figure 4.9. Near-surface results from *Johnson et al*. [2006a] for regions with an abundance of spherules are included for comparison (blue line). Error bars, representing relative error, are the same for all regions. The error bars are shown on only two regions (southwestern ejecta apron and northwestern bedrock) in order to maintain figure clarity. Absolute error is ±0.03. While absolute error will not change the trend shown in the figure, it will shift the trend up or down (to higher or lower single scattering albedo). A discussion of relative and absolute error has been included in Chapter 3.

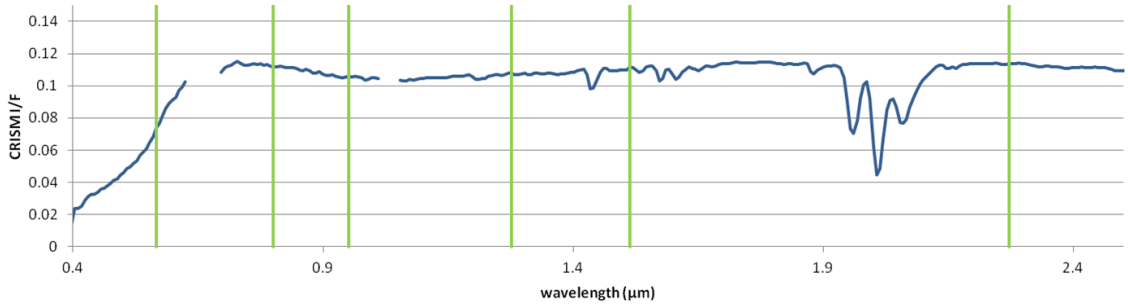

Figure 4.11. Plot of average (100x101 pixel) spectrum, representative of area including Victoria crater and ejecta apron. Spectrum taken from original data. Vertical lines indicate wavelengths used in the analyses presented in this dissertation.

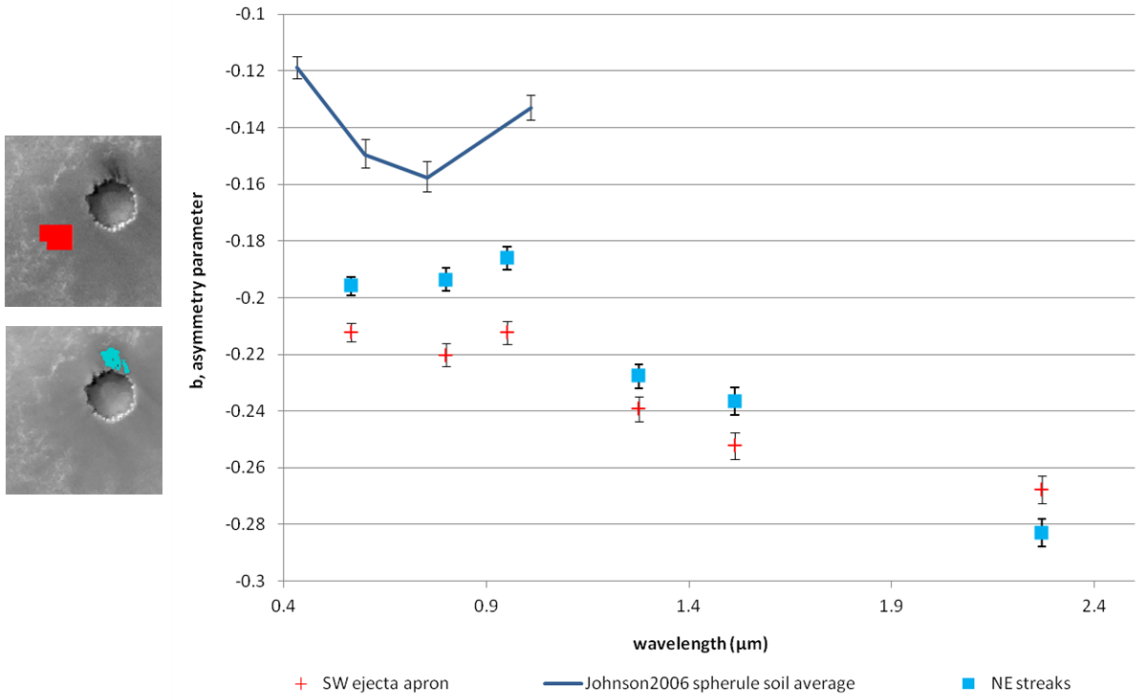

Figure 4.12. A comparison of the backscatter from two regions on Victoria's ejecta apron. The cyan region represents the basaltic wind streaks coming from the northeastern rim of Victoria. The red region represents an area in the southwestern portion of Victoria's apron that, from morphology, is relatively free of aeolian deposits compared to other sections of the ejecta apron. Error bars shown in the figure represent relative, or pixel-to-pixel error. Absolute error, which will not change the trend, but will shift it up or down (to higher or lower asymmetry parameter) is ±0.03 and depends on atmospheric parameter estimates. A discussion of both relative and absolute error is included in Chapter 3.

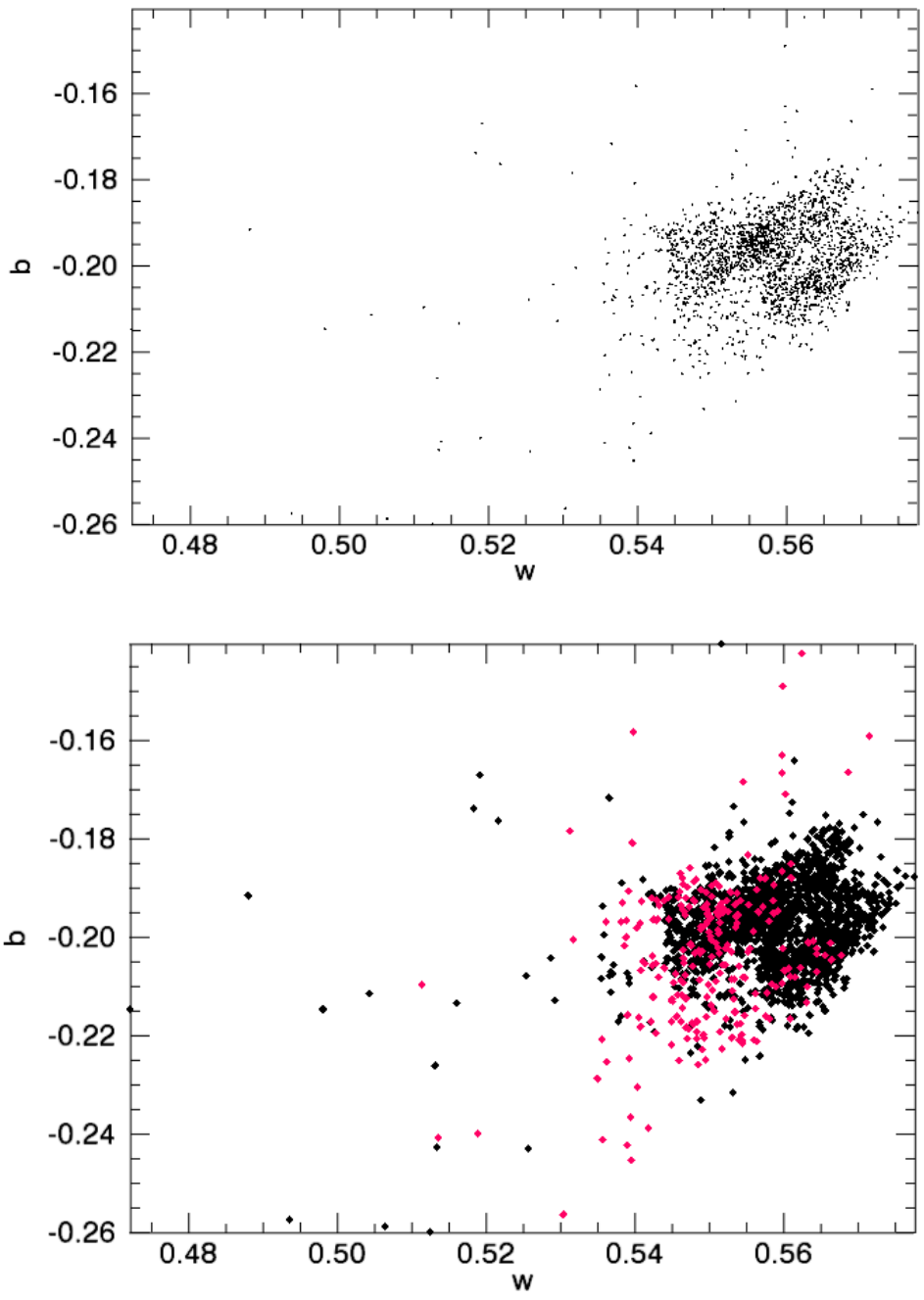

Figure 4.13. Spatial trends in *b* vs. *w* (for the 0.801 µm band). Top panel: plot of *b* vs. *w* for entire study area. Bottom panel: same as top panel except data points from Victoria's ejecta apron are colored magenta.

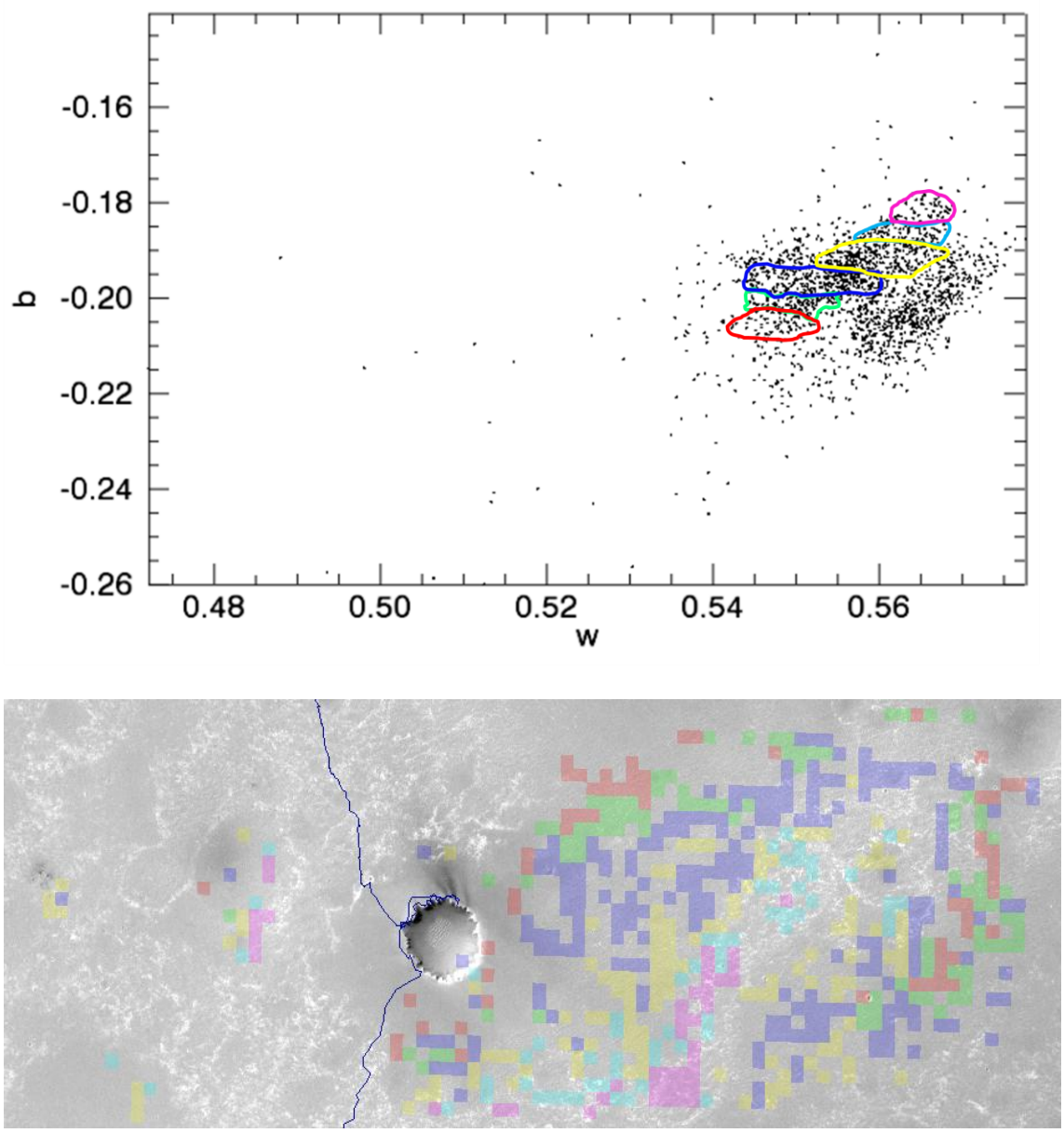

Figure 4.14. A closer look at the b vs. w trend-line. The top panel shows a plot of *b* vs. *w* at 0.801 µm for entire study area, with different sections along the positive trend-line designated by color and mapped to location in the bottom panel. Note that the regions designated by pink and red represent bedrock-rich and bedrock-poor end-members, respectively (see Figures 4.15 and 4.16).

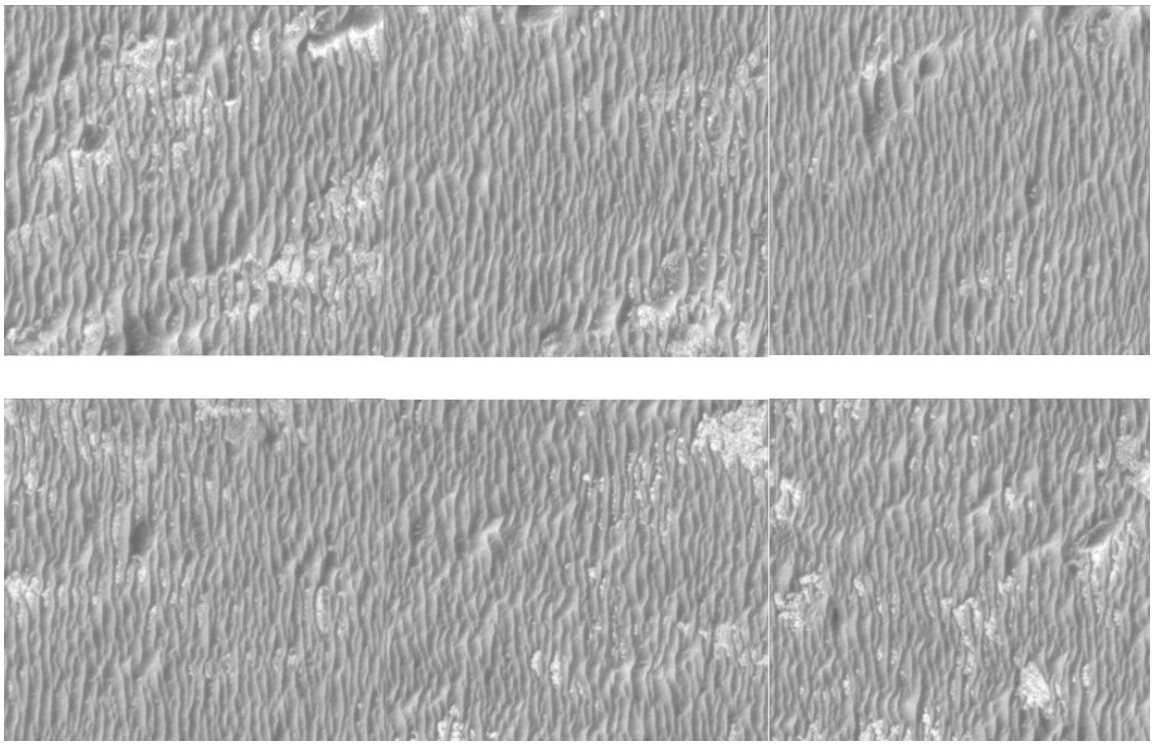

Figure 4.15. HiRISE image subsections that each cover the same area as a pixel from the high-albedo, high-asymmetry parameter class designated in pink in Figure 4.14. Subsections taken from HiRISE image PSP_009141_1780_RED.

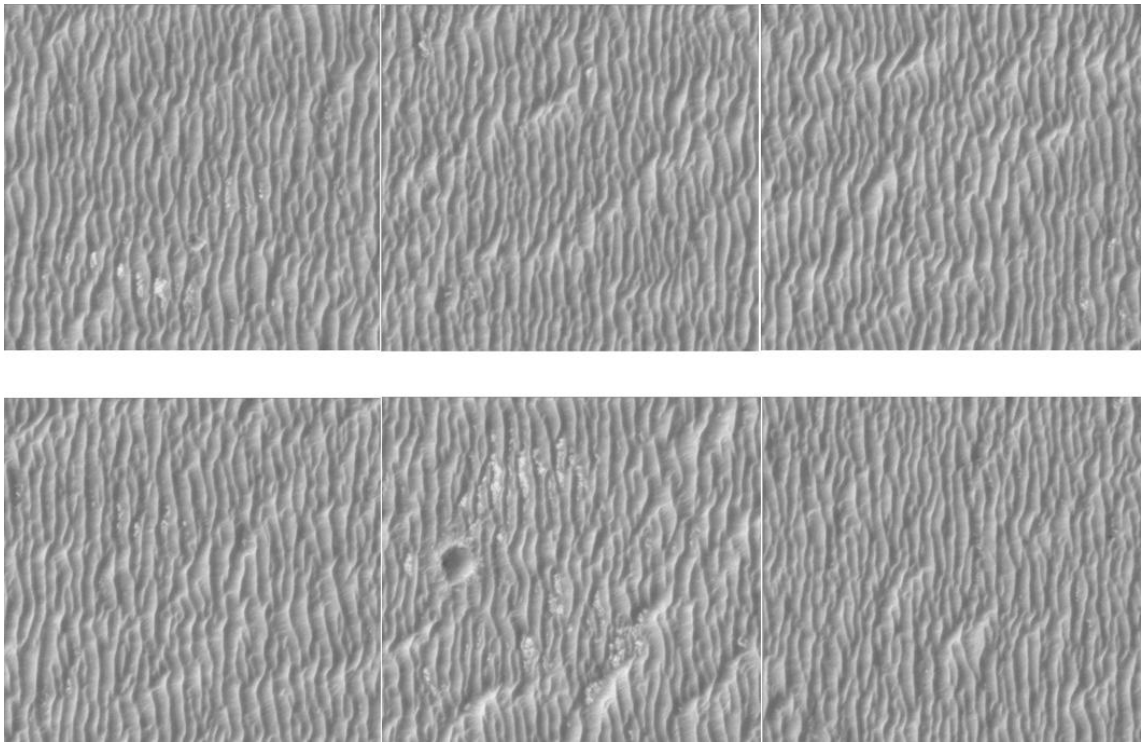

Figure 4.16. HiRISE image subsections that each cover the same area as a pixel from the low-albedo, low-asymmetry parameter class designated in red in Figure 4.14. Subsections taken from HiRISE image PSP_009141_1780_RED.

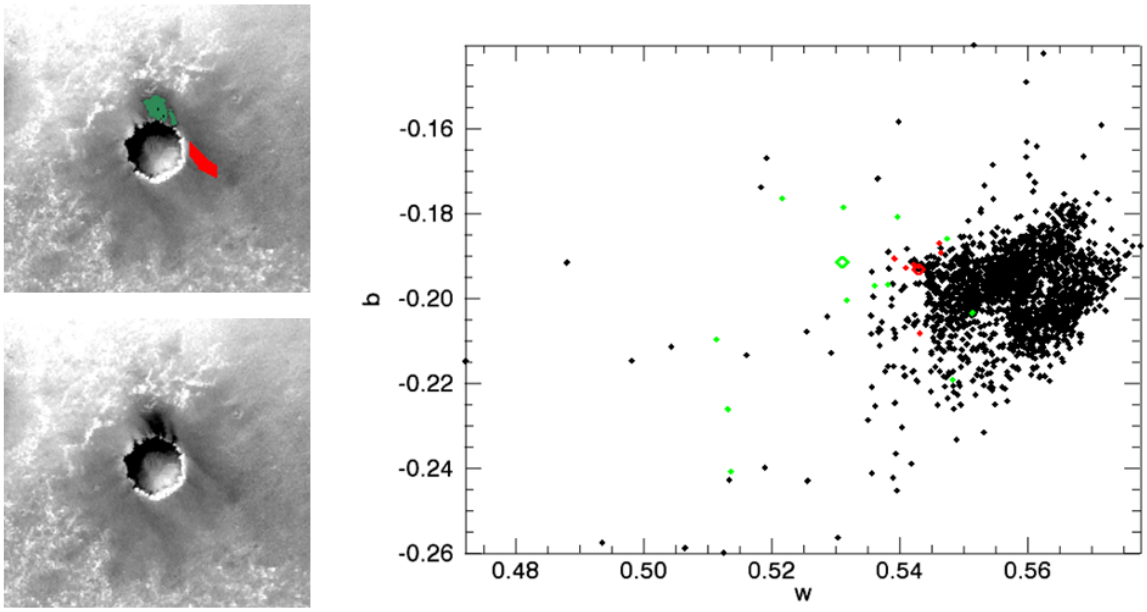

Figure 4.17. *b* vs. *w* for wind streaks. Left panel: Regions of interest shown on original CRISM I/F at 0.801 µm at full resolution for context. Right panel: Plot of *b* vs. *w* at 0.801 µm for the study area. Points in green represent the northern basaltic streaks near Victoria crater, points in red represent the eastern streaks, also near Victoria crater, and points in black represent the rest of the scene. Open diamonds indicate averages for each region, closed diamonds indicate individual pixels. Note that the average parameters for both types of streak indicate that they are off the main trend-line. The streaks are lower albedo and less backscattering than other soils (refer back to Figures 14-16 for an interpretation of the trend-line as a mixing line between soil-rich and bedrock-rich terrain).

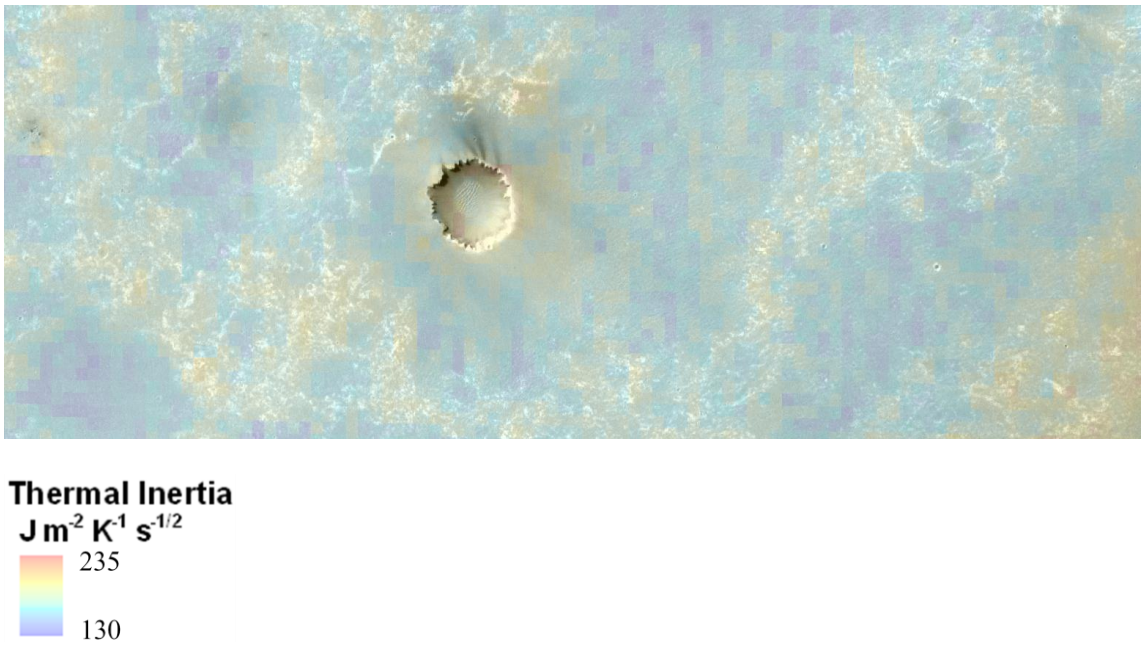

Figure 4.18. Map of thermal inertia over study area. Since thermal inertia is affected by bedrock as well as the presence of spherules and soil covering spherules, spatial correlations between thermal inertia and spherules are not readily apparent.

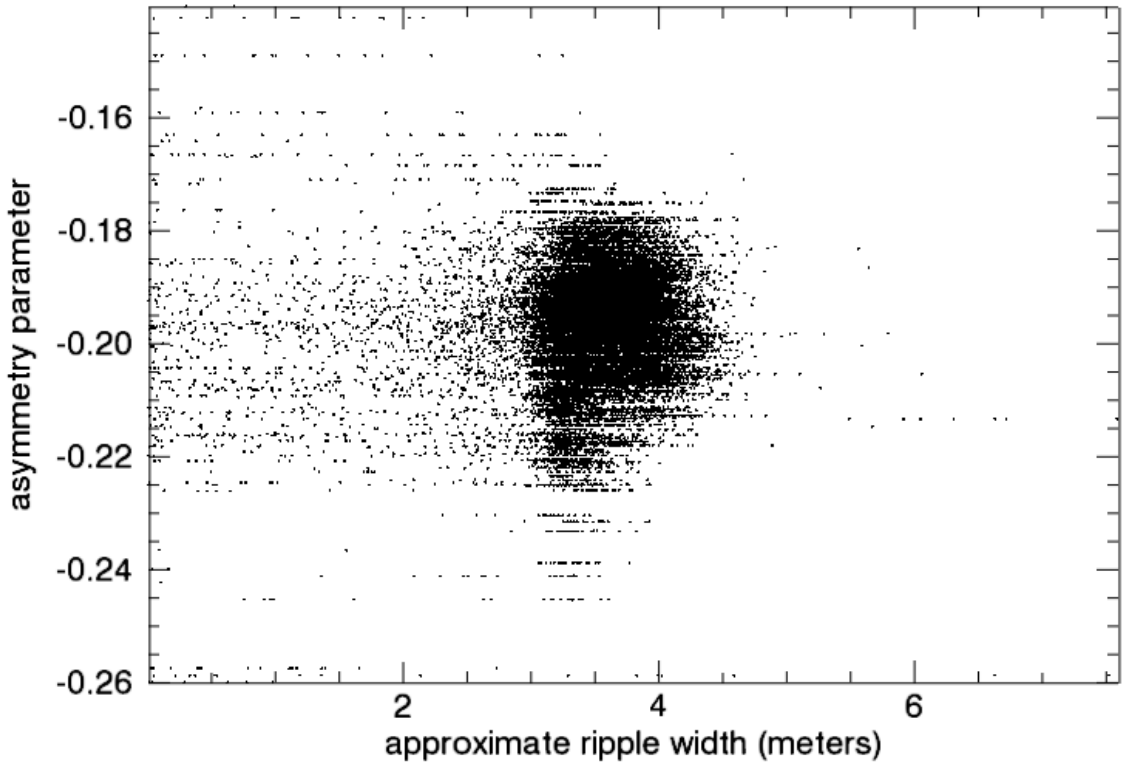

Figure 4.19. Asymmetry parameter at 0.801 µm, plotted against approximate ripple width based on HiRISE image PSP_009141_1780_RED.JP2 (see Figure 4.1 for footprint). There is no apparent trend between asymmetry parameter and approximate ripple width. Horizontal lines are an artifact of resampling (due to the differing resolutions of the scattering parameter maps and the HiRISE image).

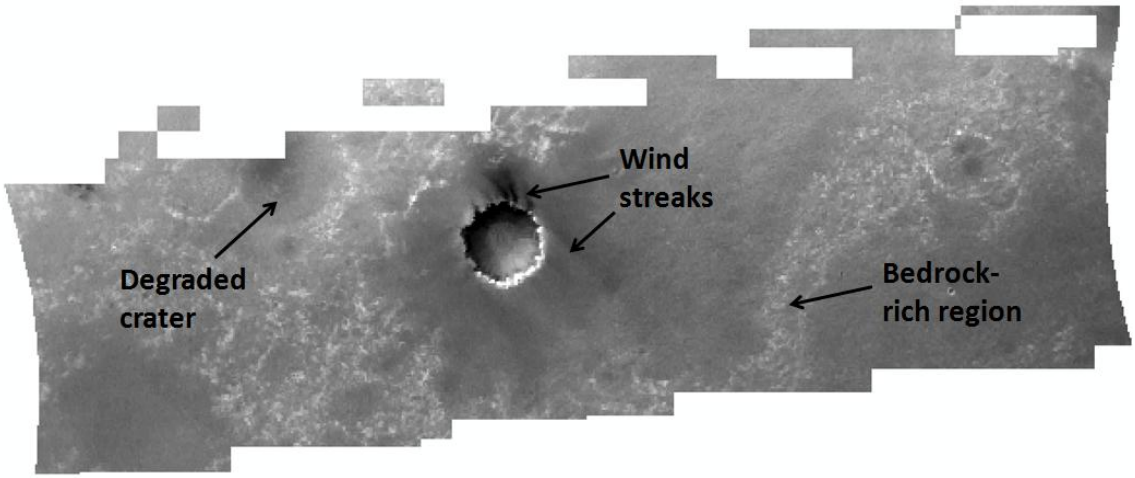

Figure 4.20. I/F at 0.801 μm for study area.

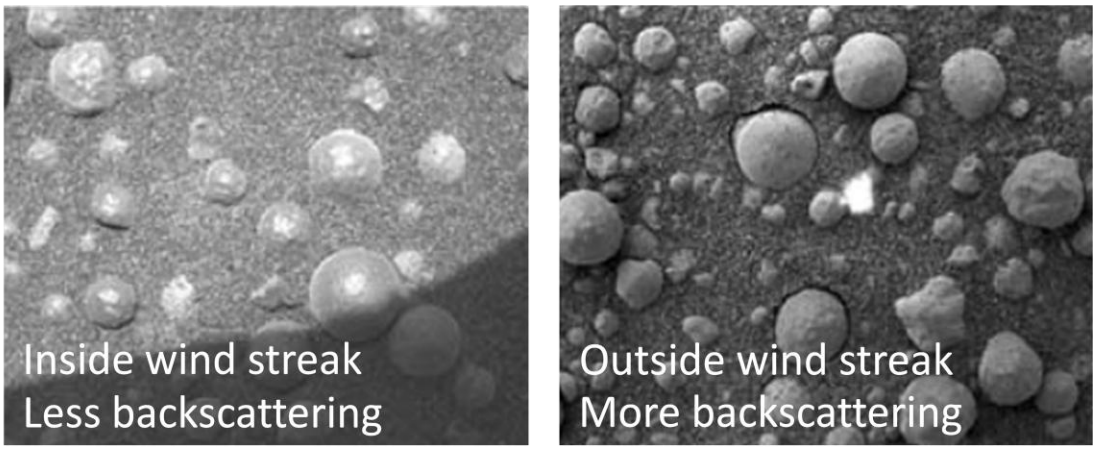

Figure 4.21. Images of hematite-rich spherules taken with the Opportunity rover's Microscopic Imager. In the left panel, spherules have been buried, resulting in a texturally smoothed surface. Whereas, in the right panel, spherules have not been buried as deeply by aeolian material. Adapted from *Geissler et al*. [2008].

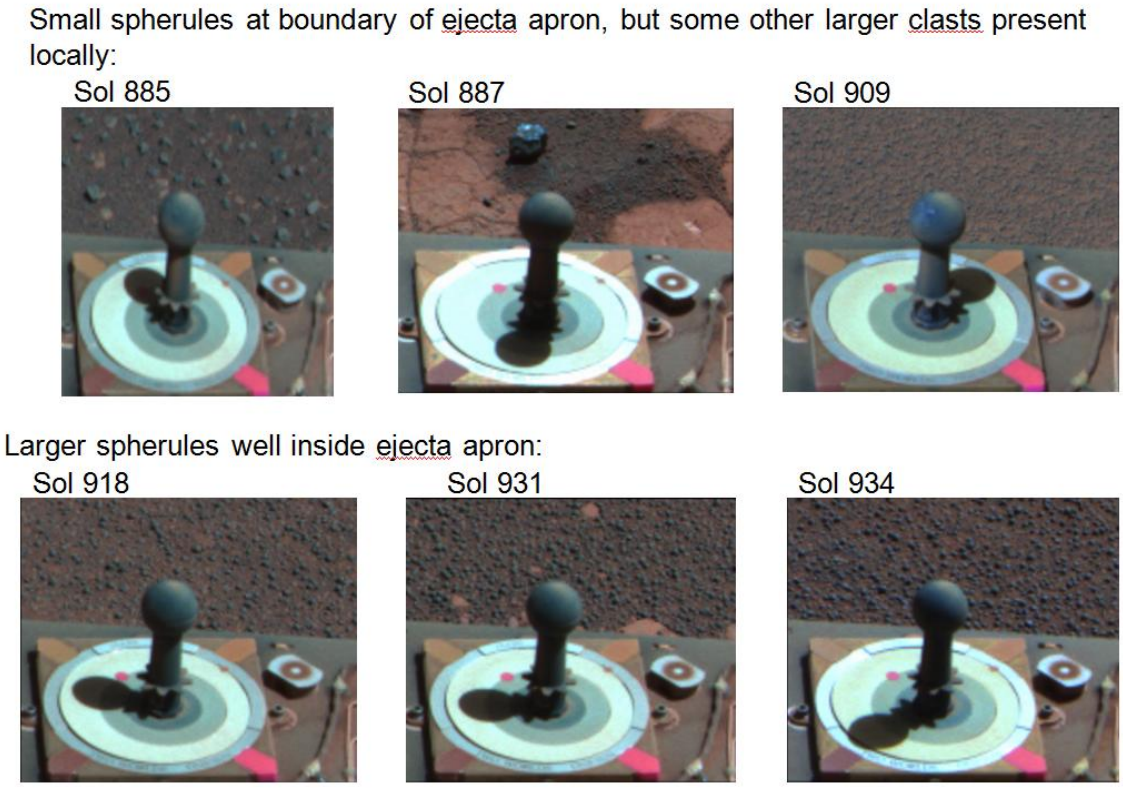

Figure 4.22. Pancam images showing observed differences in spherule size as Opportunity drove farther into Victoria's ejecta apron. Calibration target present for scale.

Figure 4.23. Image of bedrock and soil from Sol 936.

Figure 4.24. View from the ground: these images taken by the Opportunity rover show Victoria's ejecta apron and the bedrock just beyond. Note the small ripples and dense spherule cover on the ejecta apron.

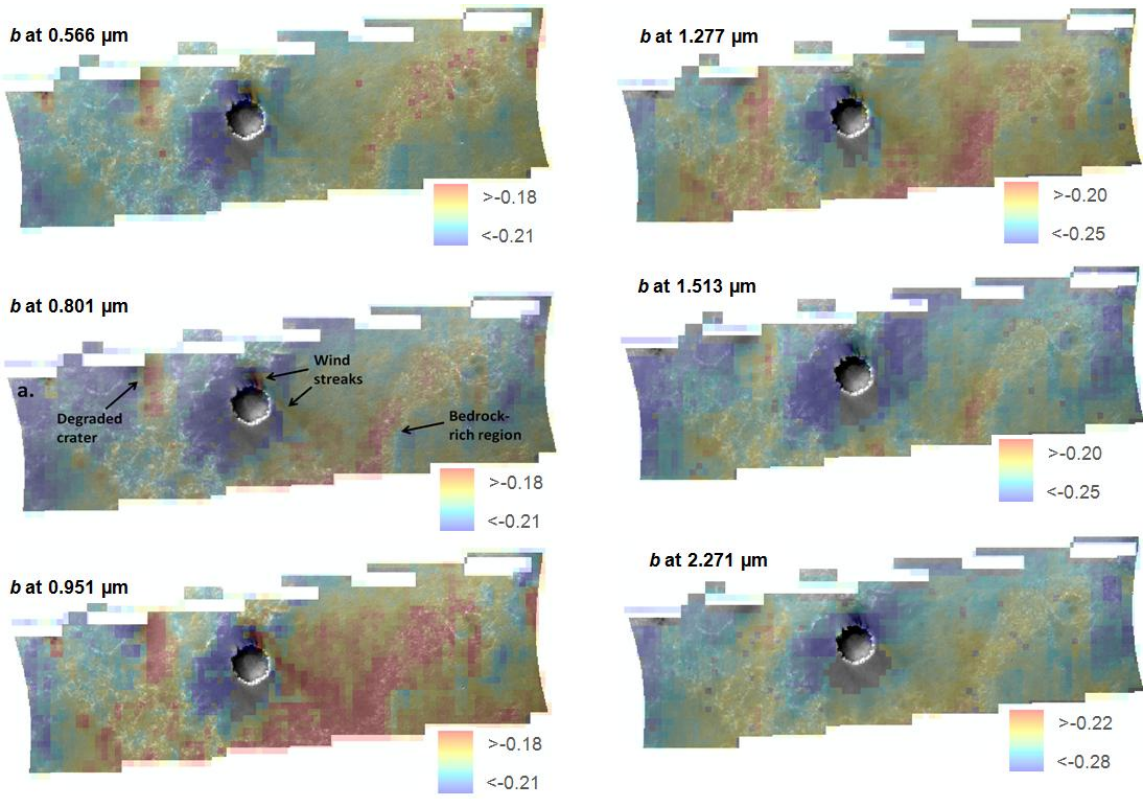

Figure 4.25. Asymmetry parameter maps as a function of wavelength. Note that the map at 0.566 µm has the lowest associated error. For scale, Victoria crater, in the approximate center of each image, is ~750 meters wide. The same color scale is used for the three shortest wavelengths, but this convention was not followed at longer wavelengths in order to display the full spatial variability of the asymmetry parameter.

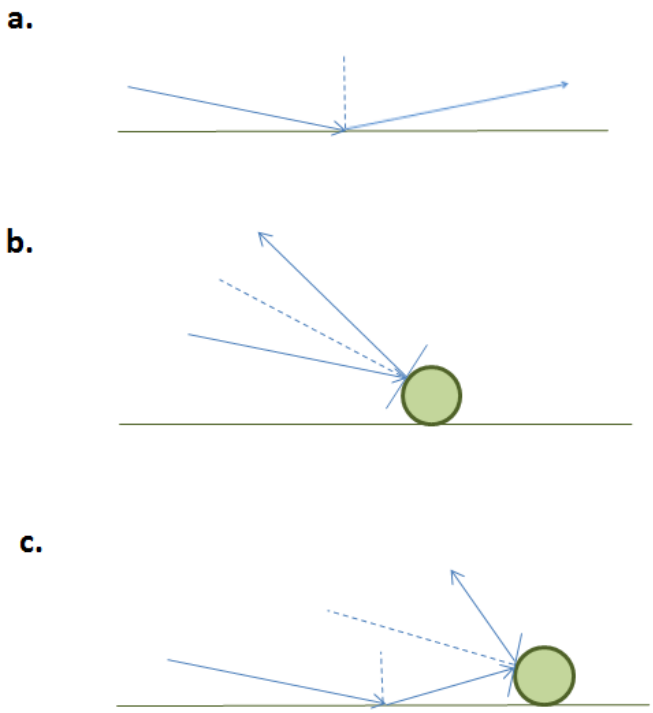

Figure 4.26. A schematic that uses idealized ray diagrams to show how the return angle of the light is affected by the presence of spherules. Dashed lines are surface normals.

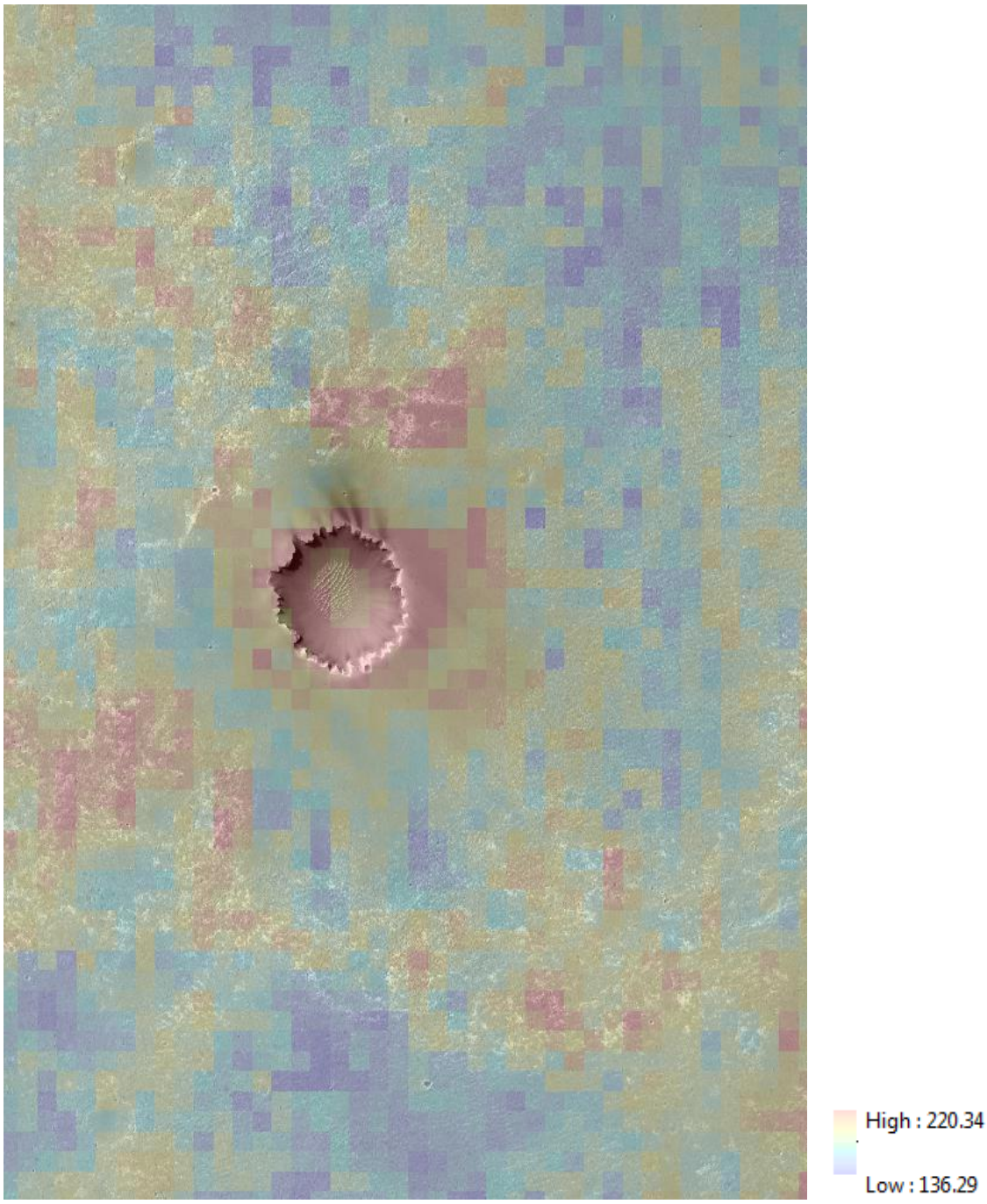

Figure 4.27. Zoom-in on thermal inertia of Victoria's apron and surroundings.

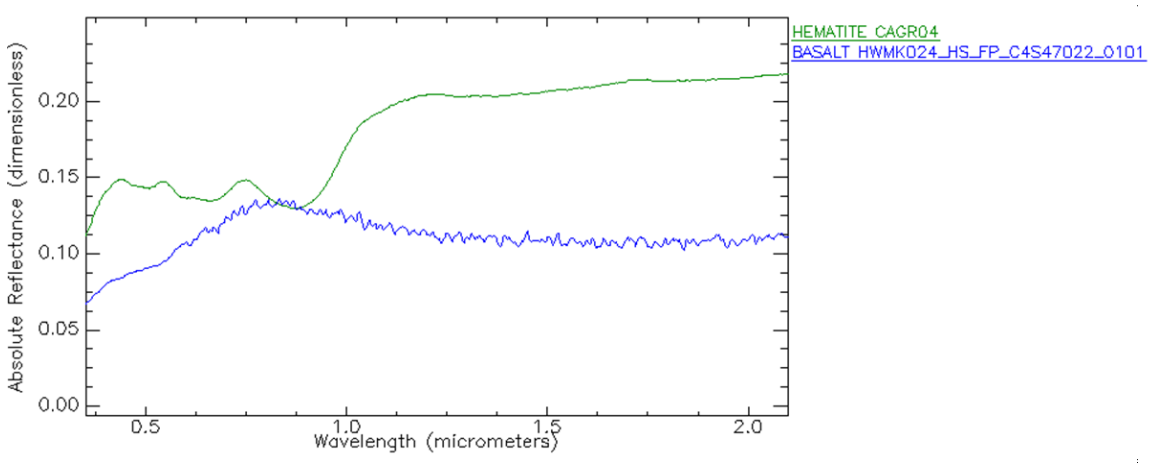

Figure 4.28. Spectra of materials (from the CRISM Spectral Library) similar to those found around Victoria crater. The hematite was measured at an incidence angle of 30°, an emergence angle of 0°, and a phase angle of 30°, using a bidirectional measurement. The basalt was measured at an incidence angle of 0° using a directional-hemispherical measurement. Both measurements use a Halon reference.

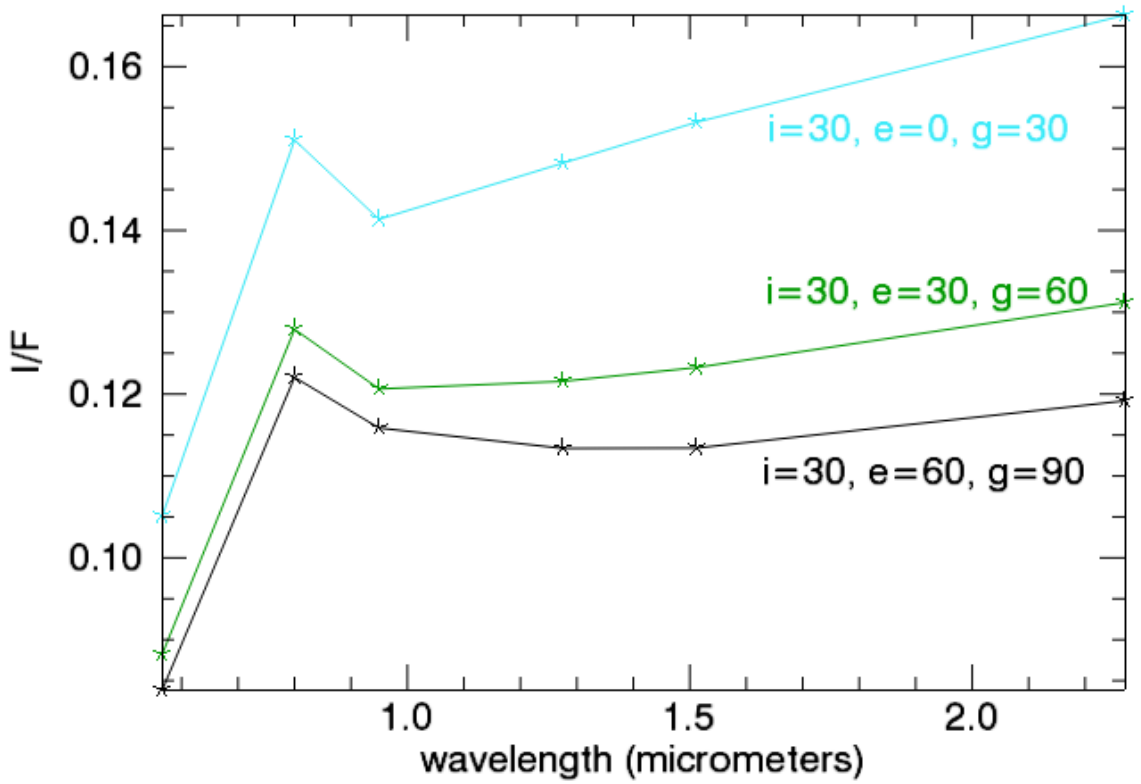

Figure 4.29. Reconstructed I/F values at various observation geometries, for the best-fit scattering parameters.

References

Andrews-Hanna, J. C., R. J. Phillips, M. T. Zuber (2007), Meridiani Planum and the global hydrology of Mars, *Nature, 446*, 163-166.

Arvidson, R. E., F. Poulet, R. V. Morris, J.-P. Bibring, J. F. Bell II, S. W. Squyres, P. R. Christensen, G. Bellucci, B. Gondet, B. L. Ehlmann, W. H. Farrand, R. L. Fergason, M. Golombek, J. L. Griffes, J. Grotzinger, E. A. Guinness, K. E. Herkenhoff, J. R. Johnson, G. Klingelhofer, Y. Langevin, D. Ming, K. Seelos, R. J. Sullivan, J. G. Ward, S. M. Wiseman, M. Wolff (2006), Nature and origin of the hematite-bearing plains of Terra Meridiani based on analyses of orbital and Mars Exploration rover data sets, *J. Geophys. Res.*, *111*, E12S08.

Arvidson, R. E., J. W. Ashley, J. F. Bell III, M. Chojnacki, J. Cohen, T. E. Economou, W. H. Farrand, R. Fergason, I. Fleischer, P. Geissler, R. Gellert, M. P. Golombek, J. P. Grotzinger, E. A. Guinness, R. M. Haberle, K. E. Herkenhoff, J. A. Herman, K. D. Iagnemma, B. L. Jolliff, J. R. Johnson, G. Klingelhofer, A. H. Knoll, A. T. Knudson, R. Li, S. M. McLennan, D. W. Mittlefehldt, R. V. Morris, T. J. Parker, M. S. Rice, C. Schroder, L. A. Soderblom, S. W. Squyres, R. J. Sullivan, M. J. Wolff (2011), Opportunity Mars Rover mission: Overview and selected results from Purgatory ripple to traverses to Endeavour crater, *J. Geophys. Res.*, *116*, E00F15, doi:10.1029/2010JE003746.

Calvin, W. M., J. D. Shoffner, J. R. Johnson, A. H. Knoll, J. M. Pocock, S. W. Squyres, C. M. Weitz, R. E. Arvidson, J. F. Bell III, P.R. Christensen, P. A. de Souza Jr., W. H. Farrand, T. D. Glotch, K. E. Herkenhoff, B. L. Jolliff, A. T. Knudson, S.

M. McLennan, A. D. Rogers, S. D. Thompson (2008), Hematite spherules at Meridiani: Results from MI, Mini-TES, and Pancam, *J. Geophys. Res*., *113*, E12S37, doi:10.1029/2007JE003048.

Cord, A. M., P. C. Pinet, Y. Daydou, S. Chevrel (2003), Experimental determination of the Hapke shadowing function parameter for planetary regolith surface analogs, *Lunar Planet Sci.*, *XXXIV*, abstract #1349.

Geissler, P. E., J. R. Johnson, R. Sullivan, K. Herkenhoff, D. Mittlefehldt, R. Fergason, D. Ming, R. Morris, S. Squyres, L. Soderblom, M. Golombek (2008), First in situ investigation of a dark wind streak on Mars, *J. Geophys. Res*., *113*, E12S31, doi:10.1029/2008JE003102.

Goguen, J. D., T. C. Stone, H. H. Kieffer, B. J. Buratti (2010), A new look at photometry of the Moon, *Icarus*, *208*, 548-557.

Golombek, M., J. Grant, D. Kipp, A. Vasavada, R. Kirk, R. Fergason, P. Bellutta, F. Calef, K. Larsen, Y. Katayama, A. Huertas, R. Beyer, A. Chen, T. Parker, B. Pollard, S. Lee, Y. Sun, R. Hoover, H. Sladek, J. Grotzinger, R. Welch, E. Noe Dobrea, J. Michalski, M. Watkins, (2012), Selection of the Mars Science Laboratory Landing Site, *Space Science Reviews*, in press.

Grant, J. A., S. A. Wilson, B. A. Cohen, M. P. Golombek, P. E. Geissler, R. J. Sullivan, R. L. Kirk, T. J. Parker (2008), Degradation of Victoria crater, Mars, *J. Geophys. Res*., *113*, E11010, doi:10.1029/2008JE003155.

Hapke, B. (1993), *Theory of Reflectance and Emittance Spectroscopy*, Cambridge Univ. Press, New York.

Helfenstein, P. (1988), The Geological Interpretation of Photometric Surface Roughness, *Icarus, 73,* 462-481.

Hynek, B. M. and K. Singer (2007), Ground truth from the Opportunity Rover for Mars thermal inertia data, *Geophysical Research Letters, 34,* L11201, doi:10.1029/2007GL029687

Johnson, J. R., W. M. Grundy, M. T. Lemmon, J. F. Bell III, M. J. Johnson, R. Deen, R. E. Arvidson, W. H. Farrand, E. Guinness, A. G. Hayes, K. E. Herkenhoff, F. Seelos IV, J. Soderblom, S. Squyres (2006a), Spectrophotometric properties of materials observed by Pancam on the Mars Exploration Rovers: 2. Opportunity, *J. Geophys. Res., 111,* E12S16.

Johnson, J. R. , W. M. Grundy, M. T. Lemmon, J. F. Bell III, M. J. Johnson, R. G. Deen, R. E. Arvidson, W. H. Farrand, E. A. Guinness, A. G. Hayes, K. E. Herkenhoff, F. Seelos IV, J. Soderblom, S. Squyres (2006b), Spectrophotometric properties of materials observed by Pancam on the Mars Exploration Rovers: 1. Spirit, *J. Geophys. Res., 111,* E02S14.

Johnson, J. R., M. K. Shepard, W. Grundy, R. V. Morris, T. S. White (2007) Spectrogoniometric measurements and models of Mars analog soils. *LPS XXXVIII,* Abstract #1288.

Mellon, M. T., B. M. Jakosky, H. H. Kieffer, P. R. Christensen (2000), High-resolution thermal inertia mapping from the Mars Global Surveyor Thermal Emission Spectrometer, *Icarus, 148,* 437–455.

Morris, R. V., G. Klingelhofer, C. Schroder, D. S. Rodionov, A. Yen, D. W. Ming, P. A. de Souza Jr., T. Wdowiak, I. Fleischer, R. Gellert, B. Bernhardt, U. Bonnes, B. A. Cohen, E. N. Evlanov, J. Foh, P. Gutlich, E. Kankeleit, T. McCoy, D. W. Mittlefehldt, F. Renz, M. E. Schmidt, B. Zubkov, S. W. Squyres, R. E. Arvidson (2006), Mössbauer mineralogy of rock, soil, and dust at Meridiani Planum, Mars: Opportunity's journey across sulfate-rich outcrop, basaltic sand and dust, and hematite lag deposits, *J. Geophys. Res*., *111*, doi:10.1029/2006JE002791

Shepard, M. K. and B. A. Campbell (1998), Shadows on a Planetary Surface and Implications for Photometric Roughness, *Icarus*, *134*, 279-291.

Squyres, S. W., J. P. Grotzinger, R. E. Arvidson, J. F. Bell III, W. Calvin, P. R. Christensen, B. C. Clark, J. A. Crisp, W. H. Farrand, K. E. Herkenhoff, J. R. Johnson, G. klingelhofer, A. H. Knoll, S. M. McLennan, H. Y. McSween Jr., R. V. Morris, J. W. Rice Jr., R. Rieder, L. A. Soderblom (2004a), In Situ Evidence for an Ancient Aqueous Environment at Meridiani Planum, Mars, *Science*, *306*, 1709-1714, doi: 10.1126/science.1104559.

Squyres, S. W., R. E. Arvidson, J. F. Bell III, J. Bruckner, N. A. Cabrol, W. Calvin, M. H. Carr, P. R. Christensen, B. C. Clark, L. Crumpler, D. J. Des Marais, C. d'Uston, T. Economou, J. Farmer, W. H. Farrand, W. Folkner, M. Golombek, S. Gorevan, J. A. Grant, R. Greeley, J. Grotzinger, L. Haskin, K. E. Herkenhoff, S. Hviid. J. Johnson, G. Klingelhofer, A. H. Knoll, G. Landis, M. Lemmon, R. Li, M. B. Madsen, M. C. Malin, S. M. McLennan, H. Y. McSween, D. W. Ming, J. Moersch, R. V. Morris, T. Parker, J. W. Rice Jr., L. Richter, R. Rieder, M. Sims,

M. Smith, P. Smith, L. A. Soderblom, R. Sullivan, H. Wanke, T. Wdowiak, M. Wolff, A. Yen (2004b), The Opportunity Rover's Athena Science Investigation at Meridiani Planum, Mars, *Science*, *306*, 1698, doi: 10.1126/science.1106171

Squyres, S. W., A. H. Knoll, R. E. Arvidson, B. C. Clark, J. P. Grotzinger, B. L. Jolliff, S. M. McLennan, N. Tosca, J. F. Bell III, W. M. Calvin, W. H. Farrand, T. D. Glotch, M. P. Golombek, K. E. Herkenhoff, J. R. Johnson, G. Klingelhofer, H. Y. McSween, A. S. Yen (2006), Two Years at Meridiani Planum: Results from the Opportunity Rover, *Science*, *313*, 1403-1407.

Squyres, S. W., A. H. Knoll, R. E. Arvidson, J. W. Ashley, J. F. Bell III, W. M. Calvin, P. R. Christensen, B. C. Clark, B. A. Cohen, P. A. de Souza Jr., L. Edgar, W. H. Farrand, I. Fleischer, R. Gellert, M. P. Golombek, J. Grant, J. Grotzinger, A. Hayes, K. E. Herkenhoff, D. W. Ming, D. W. Mittlefehldt, R. V. Morris, J. W. Rice Jr., C. Schroder, R. J. Sullivan, A. Yen, R. A. Yingst (2009), Exploration of Victoria Crater by the Mars Rover Opportunity, *Science, 324*, 1058-1061.

Weitz, C. M., R. C. Anderson, J. F. Bell III, W. H. Farrand, K. E. Herkenhoff, J. R. Johnson, B. L. Jolliff, R. V. Morris, S. W. Squyres, R. J. Sullivan (2006), Soil grain analyses at Meridiani Planum, Mars, *J. Geophys. Res*., *111*, E12S04, doi:10.1029/2005JE002541.

Chapter 5 : Summary and Synthesis

In this dissertation, two very different locations on the surface of Mars are studied, using data sets acquired from orbit and acquired *in situ* to model surface properties. At both locations studied, water has affected soil properties. At the Phoenix landing site in a northern polar region of Mars, adsorbed water and pore water-ice have affected the soil cohesion. At the Opportunity rover traverse area, much closer to the equator than Phoenix, hematite-rich, millimeter-scale spherules are present and are interpreted as having formed from water flowing through rock. It is apparent that, in the region around Victoria crater, there are variations in millimeter-scale roughness due to the size, abundance, and burial depth of these spherules, and that these factors affect orbital and near-surface observations.

At the Phoenix landing site, soil cohesion, calculated using *Balovnev*'s [1983] model of excavation in conjunction with forces derived from motor currents, varies from $0.2^{+0.4}_{-0.2}$ kPa to $1.2^{+1.8}_{-1.2}$ kPa, giving upper bounds on cohesion of 0.6 to 3 kPa. Cohesion increases (corresponding to force increases up to greater than 30 N) both with proximity to relatively pure, impenetrable ice, and with proximity to the ice table, whose depth varies depending on whether the surface being observed corresponds to a mound, side, or trough of a thermal contraction polygonal landform. The ice table is shallowest at polygon mounds and is deepest at polygon troughs. At one trough with a relatively shallow surface, cohesive plates were exposed during excavation. Due to low interplate cohesion, the cohesion of these plates is not recorded by forces encountered during excavation.

An average angle of internal friction of $38^{\circ} \pm 5^{\circ}$ is retrieved for the Phoenix site by measuring slopes formed by disaggregated soils at dump sites. The angle of internal friction and cohesion together provide a complete Mohr-Coulomb description of the soil. The values of these parameters are consistent with the stability of steep trench slopes in the Phoenix Robotic Arm work area.

At the Opportunity traverse area, the information on and interpretations of surface scattering have been spectrally and spatially extended relative to previous studies by generating maps of single scattering albedo and asymmetry parameter at visible and near-infrared wavelengths. Backscattering of incident light is observed to increase with wavelength. Additionally, backscatter increases as the abundance of larger (3-5 mm) spherules increases because their presence results in a corresponding increase in roughness at the 3-5 mm scale. The abundance of large spherules increases over Victoria crater's ejecta blanket, and this can be seen from the amount of backscatter observed from orbit. Changes in spherule size are indicative of changes in composition or amount of water present during spherule formation [*Squyres et al*., 2006]. Observable differences in backscatter also include a backscatter decrease that results from the burial of spherules in sand and dust at the wind streaks emanating from Victoria crater.

The single scattering albedo of the surface varies from 0.42-0.57 (0.5663-2.2715 μm) for the study area. The asymmetry parameter of the surface varies from -0.27 to -0.17 (0.5663-2.2715 μm) for the study area. Negative values for asymmetry parameter indicate a backscattering surface. In the spectral domain, backscatter increases with increasing albedo. In the spatial domain, backscatter decreases with increasing albedo.

Findings at both study regions investigated in this work are compared to previous work, and these comparisons indicate that results are reasonable. At the Phoenix landing site, retrieved soil properties are compared to soil properties from previous work at other landing sites on Mars, and they match the Viking Lander 2 site's crusty to cloddy soil best. This provides a consistency check, given that the Viking Lander 2 site is the closest and most geologically similar landing site to that of Phoenix. For the Opportunity traverse area analyses, orbital, near-surface, and laboratory measurements are in agreement.

Use of the methods outlined in this dissertation will continue to be advantageous for future analyses of regions visited by spacecraft and those that have not been observed *in situ*. In this work, a procedure has been presented for combined modeling of atmospheric and surface contributions to scattered light, a technique which will benefit many studies of Mars. One example of an interesting application is in determining if small scale texture at the Phoenix landing site can be related to large-scale texture in the form of polygons (whose size is related to ice table depth).

References

Balovnev, V. I. (1983), *New methods for calculating resistance to cutting of soil*, Amerind Publishing (Translation), P. Datta translator and Rosvuzizdat, New Delhi, Available from National Technical Information Service, Springfield, VA 22161.

Squyres, S. W., R. E. Arvidson, D. Bollen, J. F. Bell III, J. Bruckner, N. A. Cabrol, W. M. Calvin, M. H. Carr, P. R. Christensen, B. C. Clark, L. Crumpler, D. J. Des Marais, C. d'Uston, T. Economou, J. Farmer, W. H. Farrand, W. Folkner, R. Gellert, T. D. Glotch, M. Golombek, S. Gorevan, J. A. Grant, R. Greeley, J. Grotzinger, K. E. Herkenhoff, S. Hviid. J. R. Johnson, G. Klingelhofer, A. H. Knoll, G. Landis, M. Lemmon, R. Li, M. B. Madsen, M. C. Malin, S. M. McLennan, H. Y. McSween, D. W. Ming, J. Moersch, R. V. Morris, T. Parker, J. W. Rice Jr., L. Richter, R. Rieder, C. Schroder, M. Sims, M. Smith, P. Smith, L. A. Soderblom, R. Sullivan, N. J. Tosca, H. Wanke, T. Wdowiak, M. Wolff, A. Yen (2006), Overview of the Opportunity Mars Exploration Rover Mission to Meridiani Planum: Eagle Crater to Purgatory Ripple, *J. Geophys. Res*., *111*, E12S12, doi:10.1029/2006JE002771.

.